RNA AND METALS AS A WINDOW ONTO ANCIENT BIOCHEMISTRY

A Dissertation
Presented to
The Academic Faculty

by

Rebecca Guth-Metzler

In Partial Fulfillment
of the Requirements for the Degree
Chemistry & Biochemistry in the
College of Sciences

Georgia Institute of Technology
May 2023

RNA AND METALS AS A WINDOW ONTO ANCIENT BIOCHEMISTRY

Approved by:

Dr. Loren Dean Williams, Advisor
School of Chemistry & Biochemistry
Georgia Institute of Technology

Dr. Amit Reddi
School of Chemistry & Biochemistry
Georgia Institute of Technology

Dr. Jennifer B. Glass, Advisor
School of Earth & Atmospheric Sciences
Georgia Institute of Technology

Dr. Roger Wartell
School of Biology
Georgia Institute of Technology

Dr. Nicholas Hud
School of Chemistry & Biochemistry
Georgia Institute of Technology

Date Approved: April 11, 2023

“I think I'm able to explain things because understanding wasn't entirely easy for me. Some things that the most brilliant students were able to see instantly I had to work to understand”

-Carl Sagan

ACKNOWLEDGEMENTS

I consider myself fortunate to have many people to thank. I owe a depth of gratitude to my advisors, Dr. Loren Williams and Dr. Jennifer Glass. Your support allowed me to continually challenge myself and grow in ways I could not have imagined. From you I have learned thoughtfulness in ideating, experimenting, and communicating. I am also thankful to my committee, Dr. Nicholas Hud, Dr. Amit Reddi, and Dr. Roger Wartell, for their continued support and valuable guidance through my journey.

I am grateful to have been part of two amazing lab groups, the Williams & Glass Labs. You all truly have been positive influences. I especially want to thank Dr. Marcus Bray, Dr. Moran Frenkel-Pinter, Dr. Roger Wartell, Jessica Bowman, and Chieri Ito, for giving me a firm scientific footing. I also am lucky to have walked this PhD path in step with three strong women over five years: Brooke Rothschild-Mancinelli, Emily Saccuzzo, and Minh Thu (Alice) Ma. We did it!

My past and future have been irreversibly and wonderfully transformed by Dr. Mary Peek and my experiences teaching Biochemistry II Laboratory. When I started as a mere teaching assistant, I was fearful of talking in front of students. Now, I am finishing my first semester of being a course instructor (shout out to the students and TAs of CHEM 4582 Spring ‘23) and embarking on a professorship. Through you I learned that people of all sorts, even the quiet ones, can leverage individual strengths to spread the love of learning.

I found welcoming friends and colleagues in the members of ExplOrigins and the Georgia Tech astrobiology community past and present. Keep exploring! Same too with the BBUGS gardeners, with a huge thank you to Michelle Wong and Steve Place for making our dreams literally grow.

Looking back, I see a long chain of people supporting me even before my time at Georgia Tech. I want to thank Dr. Philip Bevilacqua and the Bevilacqua Lab for taking a chance on an undergraduate artist who thought RNA was pretty cool, and everyone who believed in someone with paint brushes picking up a pipette.

A final thank you goes to my friends and family. Without your support, I wouldn't be achieving a PhD. From my parents I have a love of knowledge and a drive to succeed. From my siblings I have people in my corner that cheer for each other. From my husband I have a confidant who cares for me even when I'm too busy to. From my friends I have happy connections to the places I've been. From my cats I have chest and leg warmers.

To all people I should have mentioned but haven't, I offer you this joke I wrote as a penance: Why are protons positive? They're in their element.

TABLE OF CONTENTS

LIST OF TABLES

LIST OF FIGURES

LIST OF SYMBOLS AND ABBREVIATIONS

Å	Angstrom
AMP	Adenosine monophosphate
ApA	Adenine dinucleotide
ATP	Adenosine triphosphate
Ca^{2+}	Cadmium
cAMP	Cyclic adenosine triphosphate
CD	Circular dichroism
Co^{2+}	Cobalt
CoA	Coenzyme A
CTP	Cytidine triphosphate
Cu^{2+}	Cupric copper
DFT	Density functional theory
DHFR	dihydrofolate reductase
DNA	Deoxyribonucleic acid
EDTA	Ethylenediaminetetraacetic acid
F	Folded
FAD	Flavin adenine dinucleotide
Fe^{2+}	Ferrous iron
Fe^{3+}	Ferric iron
GOE	Great Oxidation Event
GTP	Guanosine triphosphate
H_2O_2	Hydrogen peroxide
HEPES	4-(2-hydroxyethyl)-1-piperazineethanesulfonic acid
HPLC	High performance liquid chromatography

I	Intermediate
IDT	Integrated DNA Technologies
k_{obs}	Observed rate constant
LC-MS	Liquid chromatography mass spectrometry
LFQ	Label-free quantification
LSU	Large ribosomal subunit
LUCA	Last universal common ancestor
M^{2+}	Divalent metal
M^{2+}-μc's	Microclusters
Mg^{2+}	Magnesium
Mn^{2+}	Manganese
mRNA	Messenger RNA
MS	Mass spectrometry
N	Native
NAD	Nicotinamide adenine dinucleotide
O_2	Molecular oxygen
P4-P6	*Tetrahymena* ribozyme P4-P6 domains
PAGE	Polyacrylamide gel electrophoresis
RNA	Ribonucleic acid
rProtein	Ribosomal protein
rRNA	Ribosomal RNA
rU_{20}	Polyuridylic acid 20-mer
S.E.M.	Standard error of the mean
SAM	S-adenosyl methionine
SDS	Sodium dodecyl sulfate
SSU	Small ribosomal subunit

tRNA	Transfer RNA
$tRNA^{Phe}$	Phenylalanine transfer RNA
U	Unfolded
UTP	Uridine triphosphate
Zn^{2+}	Zinc

SUMMARY

RNA is one of life's three essential biopolymers. RNA is so entrenched in biology that it is thought to have arisen near the origin of life itself. Work herein uses RNA's ancient relationship with metals as a detective's lens to peer back into time. The dependence of RNA on divalent metal (M^{2+}) ions for its form and function is well-studied, but that knowledge left gaps in the deeper significance of the natural RNA-M^{2+} relationship. This work turns the RNA-M^{2+} relationship into new insight about RNA's origin and evolution through time. We first demonstrate a shared reaction between two different M^{2+} and RNA, further evidence that RNA may change between M^{2+} through time, making RNA adaptable and thereby successful over Earth history. We then show that RNA combined with M^{2+} yields innate yet sophisticated behavior not previously understood and shedding light on RNA's origin.

RNA uses Mg^{2+} as its primary M^{2+} partner in modern life. However, RNA evolved when Fe^{2+} was more bio-available, in a time before rising atmospheric oxygen caused Fe^{2+} to "rust out". Mg^{2+} and Fe^{2+} are similar in size and atomic coordination, suggesting Fe^{2+} could have been an earlier binding partner of RNA. Confoundingly, Fe^{2+} exposed to oxygen forms free radicals that break down biomolecules including RNA, limiting studies of similarities of Mg^{2+} and Fe^{2+} in RNA chemistry. This research shows that when Fe^{2+} is kept in anoxic conditions mimicking early Earth, it does not cause oxidation reactions. Instead, Fe^{2+} has the same reaction with RNA as does Mg^{2+}. Both Fe^{2+} and Mg^{2+} cause RNA to adopt a specific, 180° arrangement of certain atoms that leads to RNA self-cutting called "in-line" cleavage. This reaction similarity of Fe^{2+} and

Mg^{2+} adds to growing evidence that Fe^{2+} may have been an early binding partner of RNA, and that RNA adaption through swapping out M^{2+} may have made it successful over billions of years. Moreover, Fe^{2+} may have sped up early RNA evolution relative to Mg^{2+}, allowing RNA to diversify and multiply.

To RNA, M^{2+} is a double-edged sword. While M^{2+} ions catalyze RNA in-line cleavage, shortening its lifetime, they also promote RNA folding, which in turn protects RNA from cleavage. Here, we combine these concepts into the following scheme: too little M^{2+} shortens RNA lifetime because there is no folding and therefore no cleavage protection, too much M^{2+} shortens RNA lifetime because cleavage overwhelms folding protection, but the in-between "Goldilocks peak" of moderate $[M^{2+}]$ is "just right". Our simulations and experiments using Mg^{2+} support this hypothesis, showing that folding RNAs had Goldilocks peaks while non-folding RNAs do not. The peaks can take on a variety of appearances, revealing unexpected complexity from the innate RNA-Mg^{2+} relationship. The Goldilocks peak appearance depends on RNA sequence, meaning the phenomenon can be tuned by a simple change in RNA code. Tuning Goldilocks peaks through RNA sequence is a potential mechanism for chemical and biological evolution. The average Goldilocks peak of modern RNA may reflect the metal conditions of its origin, giving a clearer picture of the environment where life emerged. The Goldilocks peak boost to RNA lifetime perhaps caused RNA to win out over competing polymers on early Earth, a possible explanation for why RNA is one of life's core biopolymers.

CHAPTER 1. INTRODUCTION

How did life begin? Why is life made from its current chemistry of nucleic acids, proteins, carbohydrates, water, etc.? These are questions in the field of astrobiology, the study of the origin, evolution, distribution, and future of life in the universe (1). These are also questions that can be investigated in part by studying RNA. RNA is useful for interrogating questions on the origin of or early life because it was an early biomolecule in evolution still abundant today, with preserved ancient information. Chemical laws and principles do not change across time, therefore studying RNA chemistry now reveals the ancient rules of biochemistry. One such rule is that RNA depends on metals for its form and function, which highlights the ancient importance of metals in early evolution. Detecting the RNA-metal relationship might uncover a set of metal conditions that aided life's emergence and remains integral in biology to this day.

1.1 RNA is a molecule of ancient importance

Life on Earth originated at least 3.4 billion years ago (2). Meeting the criteria of life meant becoming a self-sustaining chemical system capable of Darwinian evolution, according to a popular definition (3). The ability of known life to self-sustain, or renew its biomolecules, depends on RNA. Darwinian evolution requires a genetic code, which can be carried by RNA. Therefore, RNA may have supported early life, possibly near to the origin of life, although this can never be known (4). RNA was not necessarily the sole or original biopolymer; proto-biopolymers could have predated RNA (5). However, such ancient molecule identities are uncertain, while RNA is certainly ancient and can be

studied *in situ*. Lasting signals of RNA's early importance are its position in the core of life, information content, conservation, catalysis, and ubiquity across biology.

1.1.1 RNA and protein mutualism is at the core of life

The central dogma of biology is that life uses DNA as a template to transcribe RNAs, some of which are translated into protein. Out of the 63 protein-coding genes shared by all life, 58 support translation, 2 are for transcription, and 3 are for genetic replication and repair (6), meaning that translation and its supporting processes were more central to ancient life than other processes, for example metabolism, membrane maintenance, cell division, and molecular transport. Transcription is currently thought to predate DNA replication (7,8), leaving transcription and translation as the pillars of early life. A core of translation, making protein, and transcription, making RNA, is reasonable on a molecular level. First, components to make both RNA and protein likely existed together on early Earth (9,10). There would have been ample opportunity for the two to interact rather than separate to pure environments. Second, all life uses RNA to make protein and uses protein to make RNA in a mutual cycle (11). To make protein, messenger RNA (mRNA), holds the code for a protein to be constructed by ribosomal RNA (rRNA) using amino acids carried by transfer RNA (tRNA). To make RNA, ribonucleotides are linked together by a protein called RNA polymerase. By extension, all modern biology is elaborations on a ceaseless cycle of RNA and protein mutualism reaching back to before the birth of life itself. RNA with protein is an ancestor to all life.

1.1.2 RNA carries genetic and physical information

RNA is distinct from protein in that the sequence that gives it is structure is also its genetic code. RNA serves as a genetic template for a complementary RNA strand, which in turn templates the original RNA. A protein cannot template itself. But in RNA, the genotype and phenotype are united. One consequence is that RNA molecular evolution can be many orders of magnitude faster than organismal evolution, where phenotype and the DNA genotype are separate (12). If evolution on early Earth included a simple system wherein RNA could be copied, RNAs susceptible to degradation would be copied to a lesser extent and thereby removed from the gene pool. This would encourage rapid growth of RNA complexity to support early biochemistry. Such RNA evolution exists modernly as viroids, small circular RNAs that infect plants, where the survival and replication of the viroid depends on the RNA's physical shape (13). RNA is also fully capable of carrying a genome, which it does in RNA viruses (14). In sum, RNA is a carrier of genetic information with implications for the progress early evolution.

1.1.3 RNA is highly conserved

The most ancient, coded information in cells still detectable in modern life, i.e. the oldest conserved sequences, is rich in instructions for building and using RNA. Many such sequences pre-date life's last universal common ancestor (LUCA), indicating they arose at the time of or before LUCA. Many studies have reconstructed LUCA's genome to understand how it lived by finding protein-coding genes conserved across modern organisms (6,15-18). While insightful, protein-focused studies can only give protein-related results. In a study comparing full genomes rather than only protein-coding genes, of life's 35 most-conserved sequences (defined by 100 nucleotide fragments), 40% are for rRNA, 46% are related to tRNA, and 14% are for adenosine triphosphate-binding

cassette transporters, which depend on an RNA nucleotide (19). rRNA sequences also have the greatest levels of conservation. In fact, rRNA's level of conservation cements 16S rRNA as a biochemical standard for measuring diversity and identities of organisms, as 16S rRNA is identifiable across all life while simultaneously harboring sequences specific to the different levels of taxonomy that emerged through time (20). RNA's deep conservation in the genetic code insinuates RNA in the earliest biochemistry.

RNA is not only conserved by sequences in genetic code, but RNA's structure is conserved in physical patterns that pre-date known gene sequences. During evolution, functional and physical constraints on structured RNA tend to maintain its existing portions, causing adaptation to occur through offshoots on the RNA called RNA expansion segments (21). Addition of new segments onto old creates growth through accretion rather than remodeling. To reconstruct the ancient past, then, removing successive outer layers of expansion segments reveals increasingly ancient portions of RNA. This dissection process applied to the ribosome, itself one of life's earliest molecular machines, traces its lineage back even farther than conserved genes. Long before LUCA had ribosomes, there existed a few RNA segments that eventually became rRNA.

1.1.4 RNA is catalytic

Another argument for RNA's antiquity is that its ability for catalysis may have created indispensability during early evolution. RNA's catalysis was discovered in the early 1980's in the form an RNA enzyme, or ribozyme, that reacts to cleave itself (22,23). Since then, the known catalysis of RNA has expanded to over twenty different

reactions (24). Each one is further support for RNA having played an important role as an enzyme on early Earth. Of note, the ribosome, responsible for making all coded proteins, catalyzes peptide bond formation using its RNA, making it a ribozyme (25). It is possible that RNA performed myriad other reactions that helped life to evolve.

1.1.5 RNA is ubiquitous across biology

RNA and its chemical structure are spread throughout biochemistry, pointing to an early emergence followed by adoption across systems. Outside of its role in protein translation, RNAs have found their way into essential processes including DNA replication (26), tRNA processing (27), gene regulation (28-31), molecule and temperature sensing (32-35), and cellular organization by phase separation (36,37).

Similarly, RNA's chemical structure has been appropriated in essential cofactors. Two of the building-block units that make RNA, or nucleotides, called adenosine triphosphate (ATP) and guanosine triphosphate (GTP), are essential protein cofactors and energy currency for all cells (38,39). A third nucleotide bearing a cyclic phosphate called cyclic adenosine monophosphate (cAMP) is a multi-purpose signaling molecule in all domains of life (40). More cofactors used in all domains of life contain embedded or modified RNA nucleotides as part of their chemical makeup, including coenzyme A (CoA) (41), nicotinamide adenine dinucleotide (NAD) (42), S-adenosyl methionine (SAM) (43), and flavin adenine dinucleotide (FAD) (44). It is theorized that these protein cofactors were once the active sites of RNA, modified RNA, or RNA-like molecules, maintained over time as the surrounding parts of the molecule were slowly replaced with coded proteins (45). In analogy, these cofactors could be the only original parts of

exceedingly ancient ribo- or near-ribo-zymes, wherein the rest of the molecule has since been cast into a protein fossil.

1.2 RNA's existence depends on metals

RNA is a salt (46). It is an assembly of cationic metals and anionic polymer that dissociate in solution. Upon dissolution, the metal ions surround the RNA in an ionic cloud (47). Rather than being a mere consequence of RNA's negative charge, the attracted cationic metals are integral to RNA biochemistry, supporting RNA's structure (48) and unlocking otherwise inaccessible reactions (49-51). Particularly important for RNA biochemistry are divalent cations (M^{2+}), which per their 2+ charge can take the place of two monovalent ions. Constraining one M^{2+} near RNA thereby freeing two monovalent ions is net entropically favorable (52). Therefore, RNA is given to draw in M^{2+}. M^{2+} are of particular interest because of their natural availability, enhanced support of RNA structure, and special reactivity conferred to RNA.

1.2.1 RNA folds with M^{2+}

When RNA's negative charge is locally neutralized by metal ions, it can self-associate rather than self-repel. The majority of self or intramolecular contacts are hydrogen bonds formed between complementary nucleobases. Each adenine to uracil or guanine to cytosine pairing is called a base pair. The base pairing of stretches of nucleobases within an RNA is classified as secondary structure. Additional self-contacts in 3D space that bring the secondary structure together constitute tertiary structure. When RNA moves from a random, un-associated form toward or to tertiary structure, the process is called folding. The random, un-associated form is called unfolded (U), and the

natural tertiary structure form is called native (N). In between are secondary structure up to incomplete tertiary structure forms, or intermediates (I). RNA folding proceeds by U → I → N (53).

Metals allow RNA's folded, low-free energy state (54). However, it is important to note that the transition from unfolded to folded is net due to the increased entropy of water. When the RNA collapses fewer waters are required to organize around its smaller surface (55). Both monovalent metals and M^{2+} can tip the scale taking RNA from unfolded to folded, but to different extents. Secondary structure readily forms with either monovalent metal or M^{2+}. But, the higher negative charge density of RNA tertiary structure, which is more compact, favors the metal with a higher charge density (i.e. M^{2+}) (56). In experiments, some RNAs can fold to the native state in high monovalent metal but will do so with far less M^{2+} required (57-59). Other RNAs only reach an intermediate folding state with monovalent metals and require addition of M^{2+} to achieve the native state (60,61). Additionally, certain local RNA folds can only form with M^{2+} (62). In nature, RNA folds natively using a mixture of monovalent metal and M^{2+} and sometimes both are required (63).

1.2.2 RNA is cleaved with M^{2+}

Metals of a 2+ charge and higher, i.e. multivalent metals, are distinct from monovalent metals in an ability to drive RNA to cleave itself (Figure 1.1). The cleavage occurs through deprotonation of RNA's 2' hydroxyl group, allowing 2' oxygen attack on the phosphate backbone, which consequentially releases the rest of the RNA molecule (64). The reaction proceeds when the 2' oxygen, phosphorus, and leaving oxygen come

into 180°, or linear, alignment. Hence, the reaction is called in-line cleavage. M^{2+} (and higher) may induce in-line cleavage through multiple pathways. One proposal is that the metal lowers the pK_a of water allowing it to become deprotonated and act as a base in the deprotonation step of the 2' hydroxy group (65,66). Other means by which M^{2+} might support RNA cleavage include coordinating water to stabilize the intermediate state and then protonate the leaving oxygen (67,68), neutralizing negative charge formed on the leaving oxygen, drawing electrons away from the phosphorous nucleus exposing it to attack, and inducing proximity of the 2' hydroxyl group and phosphate (69).

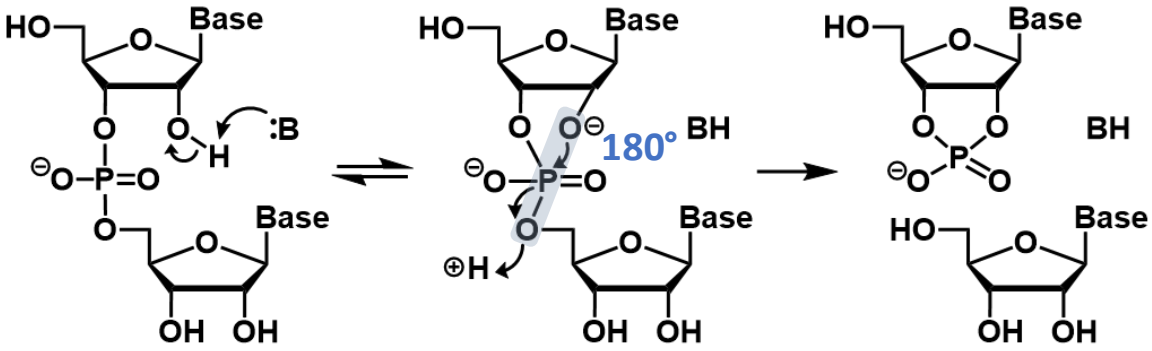

Figure 1.1 – RNA is cleaved by an "in-line" mechanism. General requirements for in-line cleavage are deprotonation of the 2' hydroxyl group, a 180° alignment of the 2' oxygen, phosphorous, and leaving group oxygen, protonation of the leaving group oxygen, and formation of a cyclic phosphate product.

1.2.3 The catalysis of RNA is supported by M^{2+}

RNA catalysis depends on metals with a few exceptions (24,70). The first discovered RNA catalysis was of RNA specifically directing its in-line cleavage (22). In-line cleavage is an example wherein the metal participates in acid-base chemistry. Added acid-base chemistry is not the only tactic by which metals help RNA overcome a lack of chemically reactive functional groups relative to protein enzymes. RNA-bound metals

can also directly participate in ionic and other electrostatic interactions (71), induce charge on nucleobases for ionic reactions (72), and allow redox chemistry (49). M^{2+} are particularly important for RNA catalysis because they tend to create greater reactivity than monovalent metals (73,74) and no trivalent or higher metal ribozymes have been found in the natural world (50).

1.2.4 The RNA-M^{2+} relationship depends on M^{2+} identity

RNA will naturally associate with a range of M^{2+}, but not all M^{2+} are equal. Different M^{2+} interact with RNA at different sites with different binding affinities, exchange kinetics, and catalytic and folding propensities. In nature, RNA interacts with the M^{2+} of biology: Mg^{2+}, Ca^{2+}, Mn^{2+}, Fe^{2+}, Co^{2+}, Cu^{2+}, and Zn^{2+} (46). These M^{2+} associate most with RNA's backbone to neutralize negative charge, with greatest favorability, measured by lowest ΔG, ordered by charge density (75). The smallest M^{2+} size gives the largest charge density and the greatest favorability. M^{2+} can also be found to different extents at the nucleobases, primarily N7 of guanine which has the opposite favorability trend as the backbone, and O6 of guanine which has mixed favorability with the metals. In total, there are over 50 patterns of metal binding to nucleobases alone, occurring to different degrees with different metals (76). Clearly metal identity has an integral impact on RNA chemistry.

Mg^{2+} is the "gold standard" for M^{2+} interactions with RNA. Mg^{2+} is the most abundant M^{2+} in cells (77) and the most prevalent M^{2+} bound to RNA *in vivo* (78). To approximate the *in vivo* effect of M^{2+} on RNA folding, Mg^{2+} is typically added to RNA *in vitro*. Such studies show that Mg^{2+} addition can transition RNA from unfolded to folded

(79-81). Mg^{2+} also most strongly favors the folded state relative to other M^{2+} as the smallest, most charge-dense M^{2+} (82). When M^{2+} properties deviate from Mg^{2+}, the RNA is less likely to adopt its Mg^{2+}-adapted native form. The ions most similar to Mg^{2+} are Fe^{2+}, Mn^{2+}, and Co^{2+} (Table 1.1).

Table 1.1 – Properties of biological M^{2+}

M^{2+}	Coordination number(s)[a]	Coordination geometry[b]	Ionic radius (Å)[b]	Hydration enthalpy (kcal/mol)[c]	First pK_a of hydrate[d]
Ca^{2+}	6,7,8	Square antiprism	0.99	381	12.7-12.9
Co^{2+}	6	Octahedral	0.72	479	9.7
Cu^{2+}	4,5,6	Square planar	0.72	499	8
Fe^{2+}	6	Octahedral	0.74	461	9.3-9.5
Mg^{2+}	6	Octahedral	0.66	458	11.2-11.4
Mn^{2+}	6	Octahedral	0.8	442	10.6-11.0
Zn^{2+}	4,5,6	Tetrahedral	0.74	488	9

[a]Ref. (83); [b]Ref. (46); [c]Ref. (84); [d]Ref. (85)

1.2.5 Mg^{2+} may be a substitute of Fe^{2+}

The similarities between Mg^{2+} and certain other M^{2+} mixed with the changing availability of M^{2+} over Earth history begs the question of whether Mg^{2+} was always the primary M^{2+} used by RNA. Fe^{2+} was more available on early Earth before the Great Oxidation Event (GOE) compared to after, when oxygen converted free aqueous Fe^{2+} to Fe^{3+} within solid iron oxides (86-90). Therefore, when RNA first emerged up through 2.4 billion years ago, it was in an environment of available Fe^{2+}, which could have integrated with and shaped RNA chemistry. The rise of oxygen, however, would have pulled Fe^{2+} out of RNA through a concentration decrease. Fe^{2+} would have further evolved out of life post-GOE because when exposed to oxygen it generates reactive oxygen species that damage biomolecules including RNA (91). Mg^{2+}, the current M^{2+} of life, does not drive

damaging redox chemistry. The possibility that reactive Fe^{2+} was once a primary M^{2+} used by RNA that has since been replaced with benign Mg^{2+} forms the Fe^{2+}-Mg^{2+} substitution hypothesis (92,93).

The Fe^{2+}-Mg^{2+} substitution hypothesis is supported from several angles:

1. Some natural and Mg^{2+}-evolved ribozymes are faster with Fe^{2+} than with Mg^{2+} (92).
2. Fe^{2+} can catalyze redox ribozyme reactions while Mg^{2+} cannot (49), making Fe^{2+} the more versatile ion.
3. Fe^{2+} to Cu^{2+}, Zn^{2+}, and Mg^{2+} substitutions have occurred with proteins, validating the principle of Fe^{2+}-Mg^{2+} substitution in biochemistry (93).
4. Fe^{2+} and Mg^{2+} fold rRNA, essential to all life, similarly (94).
5. Fe^{2+} can replace Mg^{2+} in processing of RNA by enzymes (95).

Fe^{2+} was therefore possibly a critical element for the emergence of life. Current astrobiological research can investigate the ancient metal and biochemical environment through the lens of RNA.

1.3 Thesis aims

Work in this thesis was inspired by two main ideas: that RNA endured a Fe^{2+} to Mg^{2+} cofactor transition, and that M^{2+} dualistically affect RNA. Each topic has meaning for the origin of RNA and a window of opportunity to weave old knowledge into new understanding. Studies since the 1950's (96) show that some metals, including Mg^{2+}, can cleave RNA. But, the reaction remained untested with Fe^{2+} because of its reactivity when

exposed to oxygen. The first study herein aimed to demonstrate the cleavage reaction with Fe^{2+} to draw a new parallel between Fe^{2+} and Mg^{2+} chemistry with RNA. Such evidence could support a path for Fe^{2+}-Mg^{2+} substitution in RNA over time, but also highlight differences in strengths of the reaction. We then took the knowledge that M^{2+} will cleave RNA and evidence since the 1960's that M^{2+} fold RNA (97) to address our next aim of unifying M^{2+}'s dualism into a single model. Such a model provides new insight of a point of balance for RNA between M^{2+}'s opposing effects. Through RNA's reactivity with M^{2+}, we draw a picture RNA's history of survival by walking the M^{2+} tightrope.

CHAPTER 2. CUTTING IN-LINE WITH IRON: RIBOSOMAL FUNCTION AND NON-OXIDATIVE RNA CLEAVAGE

The work described in this chapter has been previously published in the journal *Nucleic Acids Research* (98). Experiments were performed by me and by M.S. Bray and D.C. Okafor. I designed and performed all in-line cleavage and Fenton chemistry experiments with rRNA and ApA, D.C. Okafor did so for in-line cleavage with a-rRNA, and M.S. Bray did so for in the *in vivo* ribosome experiments. M. Frenkel-Pinter assisted in the analysis of the in-line cleavage experiments of ApA using HPLC and LC-MS. The manuscript was written with contributions from all coauthors.

2.1 Abstract

Divalent metal cations are essential to the structure and function of the ribosome. Previous characterizations of the ribosome performed under standard laboratory conditions have implicated Mg^{2+} as a primary mediator of ribosomal structure and function. Possible contributions of Fe^{2+} as a ribosomal cofactor have been largely overlooked, despite the ribosome's early evolution in a high Fe^{2+} environment, and its continued use by obligate anaerobes inhabiting high Fe^{2+} niches. Here we show that (i) Fe^{2+} cleaves RNA by in-line cleavage, a non-oxidative mechanism that has not previously been shown experimentally for this metal, (ii) the first-order rate constant with respect to divalent cations is more than 200 times greater with Fe^{2+} than with Mg^{2+}, (iii) functional ribosomes are associated with Fe^{2+} after purification from cells grown under low O_2 and high Fe^{2+}, and (iv) a small fraction of Fe^{2+} that is associated with the ribosome is not exchangeable with surrounding divalent cations, presumably because it is tightly coordinated by rRNA and buried in the ribosome. In total, these results expand the

ancient role of iron in biochemistry and highlight a possible new mechanism of iron toxicity.

2.2 Key Points

1) Fe^{2+} cleaves rRNA by a non-oxidative in-line cleavage mechanism that is more than 200 times faster than in-line cleavage with Mg^{2+};

2) ribosomes purified from cells grown under low O_2 and high Fe^{2+} retain ~10 Fe^{2+} ions per ribosome and produce as much protein as low O_2, high Mg^{2+}-grown ribosomes;

3) a small fraction (~2%) of Fe^{2+} that is associated with the ribosome is not exchangeable.

2.3 Introduction

The translation system is responsible for the synthesis of all coded proteins and contains life's most conserved ribonucleic acids. The common core of the ribosome is universal to all life (99,100) and has been essentially invariant since the last universal common ancestor (21,101,102). Thus, ribosomes can be interrogated as molecular fossils (103-105). Because ribosomal structure and function are strongly dependent on divalent cations (M^{2+}) (106), and because ribosomes originated long before the Great Oxidation Event (GOE), understanding ribosomal origins and evolution requires characterization of ribosomal interactions with M^{2+} ions under pre-GOE conditions (86-88,90,107).

In extant aerobic life, Mg^{2+} appears to be the dominant M^{2+} ion in the translation system. Hundreds of Mg^{2+} ions mediate ribosomal RNA (rRNA) folding and ribosomal assembly, in some instances binding to specific sites in the universal rRNA common core by direct coordination (47,106,108,109). Mg^{2+} ions facilitate association of the large

ribosomal subunit (LSU) and small ribosomal subunit (SSU) (110), stabilize folded tRNA (111), maintain the reading frame during translation (112), and link ribosomal proteins (rProteins) to rRNA (113). Mg^{2+} also catalyzes in-line cleavage (33,64,114,115), the reaction in which a divalent or trivalent metal catalyzes self-cleavage of RNA (116-119).

Before the GOE, anoxia would have stabilized abundant Fe^{2+} in the biosphere and hydrosphere. Under pre-GOE conditions, Fe^{2+} would not have caused the damage to biomolecules that occurs today in the presence of O_2, via Fenton chemistry (120). In Fenton chemistry H_2O_2, a product of Fe^{2+} autoxidation by O_2 (121), is reduced by Fe^{2+} generating hydroxyl radicals which can oxidatively damage nucleic acids (122-126). We recently reported that Fe^{2+} can fold RNA and mediate *in vitro* translation under "pre-GOE" conditions: in the presence of abundant Fe^{2+} and in the absence of O_2 (94). Based on these findings, we proposed that early ribosomal folding and catalysis used Fe^{2+} instead of, or in combination with Mg^{2+} and other M^{2+} ions. However, we found lower translation rates with anoxic Fe^{2+} than with Mg^{2+} (94). While this observation could be partially explained by ribosomes adapting to the near-absence of Fe^{2+} and the presence of tens of mM Mg^{2+} in the ocean over the last two billion years, we assume that this explanation alone is insufficient because the catalytic core of the ribosome, and its central structure appears to be so conserved that it reflects the behavior of its evolutionary ancestor more than three billion years ago. One possible explanation for this finding is that non-oxidative damage of RNA mediated by Fe^{2+} is faster than with Mg^{2+}.

Here we demonstrate that Fe^{2+} can damage RNA by in-line cleavage, which is distinct from previously characterized oxidative processes. We discovered that this second, non-oxidative mechanism of Fe^{2+}-mediated RNA damage by in-line cleavage can be more extensive in some conditions than oxidative damage. We show that anoxic Fe^{2+} is efficient in catalyzing in-line cleavage, cleaving rRNA far more rapidly and extensively than Mg^{2+}. Given that the reaction is likely first-order with respect to the

metal (127,128), the reaction rate constant (M^{-1} s^{-1}) appears to be over 200 times greater for rRNA with Fe^{2+} than with Mg^{2+}. The in-line mechanism of cleavage by Fe^{2+} was validated here by a variety of methods including reaction product characterization.

While metals such as Mg^{2+} cleave RNA, they are nonetheless essential for folding and function. In parallel with our experiments comparing Fe^{2+} and Mg^{2+} in-line cleavage, we investigated whether ribosomes from *E. coli* grown in pre-GOE conditions associate functionally with Fe^{2+} *in vivo*. We grew *E. coli* in anoxic conditions with ample Fe^{2+} in the growth media. We purified ribosomes from these bacteria and have probed their interactions with metals. We identified tightly bound M^{2+}, which survive ribosomal purification. A small fraction (~2%) of Fe^{2+} ions are not exchangeable with Mg^{2+} in solution and are detectable after purification involving repeated washes in high [Mg^{2+}] buffers. We use these tightly bound ions as reporters for more general M^{2+} association *in vivo*. The data are consistent with a model in which certain M^{2+} ions are deeply buried and highly coordinated within the ribosome (108). Our results suggest that ribosomes grown in pre-GOE conditions contain ~10 tightly bound Fe^{2+} ions compared to ~1 Fe^{2+} ion in ribosomes from standard growth conditions. Ribosomes washed with Fe^{2+} contained significantly higher Fe^{2+} and showed more rRNA degradation than ribosomes washed with Mg^{2+}. Our combined results show the capacity for Fe^{2+} to (i) associate with functional ribosomes *in vivo* and *in vitro* and (ii) mediate significant non-oxidative damage. Our results have significant implications for the evolution of rRNA and iron toxicity in disease.

2.4 Materials and Methods

2.4.1 Ribosomal RNA purification

A one-tenth volume of sodium acetate (3.0 M, pH 5.2) and an equal volume of 25:24:1 phenol:chloroform:isoamyl alcohol, pH 5.2 (Fisher BioReagents) were added to purified ribosomes. The sample was vortexed and spun at 16,200 × g in a table-top centrifuge for 5 minutes. The top aqueous layer was transferred to a new tube and extracted twice in a 24:1 mixture of chloroform:isoamyl alcohol (Acros Organics) using the same procedure. rRNA was then precipitated by adding two volumes of 100% ethanol, followed by incubation at -20°C for 30 minutes. Precipitated rRNA was pelleted by centrifuging at 16,100 × g for 15 minutes. The pellet was washed with 70% ethanol and suspended in 0.1 mM sodium-EDTA (pH 8.0). Ribosomal RNA concentrations were quantified by A_{260} ($1A_{260}$ = 40 µg rRNA mL^{-1}).

2.4.2 rRNA in-line cleavage reaction rates

Nuclease free water (IDT) was used in all experiments involving purified or transcribed RNA. rRNA for in-line cleavage experiments was purified as above by phenol-chloroform extraction followed by ethanol precipitation of commercial *E. coli* ribosomes (New England Biolabs). All in-line cleavage reaction solutions were prepared and incubated in the anoxic chamber. Fe and Mg solutions were prepared by dissolving a known mass of $FeCl_2$-$4H_2O$ or $MgCl_2$ salt in degassed water inside the chamber. 0.5 µg $µL^{-1}$ of rRNA was suspended in degassed 20 mM HEPES pH 7.6, 30 mM KCl, 5% v/v glycerol [Invitrogen (UltraPure)], and either 25 mM of $MgCl_2$ or 1 mM of $FeCl_2$. Reactions were placed on a 37°C heat block and incubated for 4 days for the $MgCl_2$ and no M^{2+} conditions and for 8 hours for the $FeCl_2$ conditions. At each time point (0, 1.5, 3, 6, 12, 24, 48, and 96 hours for the $MgCl_2$ and no M^{2+} conditions and 0, 7.5, 15, 30, 60, 120, 240, and 480 minutes for the $FeCl_2$ conditions) 4.5 µL aliquots were combined with

0.5 µL of 1 M sodium phosphate buffer pH 7.6 to precipitate the Fe^{2+} or Mg^{2+} from solution and stored at -80°C. Aliquots were defrosted on ice and combined with 2X Gel Loading Buffer II (Amicon) then loaded onto a 1% Tris/Borate/EDTA agarose gel and run at 120V for 1.25 hours. The RNA in the gel was stained with GelStar™ (Lonza) and imaged with an Azure 6000 Imaging System (Azure Biosystems). Azurespot software was used as a pixel counter to create lane profiles. rRNA peaks were integrated by fitting to an Exponentially Modified Gaussian distribution using Igor Pro (v 7.08) (Figure A.1). Observed pseudo first-order rate constants (k_{obs}) were found by taking the negative of the slope from the natural logarithm of the normalized peak area vs. time plot. Reaction rate constants (k) were calculated by $k = k_{obs}/[M^{2+}]$.

2.4.3 In-line cleavage banding patterns

a-rRNA (129), which is composed of the core of the LSU rRNA, was synthesized and purified as previously described. Lyophilized a-rRNA was resuspended in degassed nuclease free water (IDT) inside the anoxic chamber. Fe and Mg solutions were prepared by dissolving known amounts of $FeSO_4$-$7H_2O$ or $MgSO_4$ in degassed nuclease free water inside the anoxic chamber. To initiate the reaction, 1 mM (final concentration) of Mg or Fe was added to 0.02 µg $µL^{-1}$ a-rRNA in 20 mM HEPES-TRIS (pH 7.2) in a 37°C heat block. Samples were removed at 0, 0.25, 0.5, and 1 hr for added Fe^{2+}, and at 24 hrs for added Mg^{2+}. Divalent chelation beads (Hampton Research) were added to quench the reactions. Chelation beads were removed using spin columns. The RNA cleavage products were visualized using denaturing PAGE (6%, 8M urea) run at 120 V for ~1.3 hours stained with SYBR Green II.

2.4.4 Fenton chemistry reactions

Purified rRNA from *E. coli* ribosomes (New England Biolabs) was obtained by phenol-chloroform extraction and ethanol precipitation as above. A stock solution of Fe/EDTA was prepared inside the anoxic chamber by dissolving a known amount of $FeCl_2$-$4H_2O$ salt in degassed water then mixing with EDTA in degassed water. The Fe/EDTA was removed from the chamber for the Fenton reactions. Ribosomal RNA was suspended to 0.5 μg μL^{-1} in 20 mM HEPES pH 7.6, and 30 mM KCl, with 0% or 5% v/v glycerol and either 1 mM Fe/10 mM EDTA/10 mM ascorbate plus 0.3% v/v H_2O_2 or 10 mM EDTA as the reaction initiators wherein the initiators were separately dispensed onto the tube wall then vortexed with the other components. For the zero time points, reaction components were mixed in tubes containing the thiourea quenching agent at a final concentration of 100 mM. For non-zero time points the reaction mixtures were prepared as bulk solutions and incubated at 37°C on a heat block, after which aliquots were removed at 0, 10, and 60 minutes and mixed with the thiourea quenching agent at a final concentration of 100 mM. The stopped solutions were immediately frozen and stored at -80°C. For analysis, samples were defrosted on ice, combined with 2X Gel Loading Buffer II (Amicon), loaded onto a 1% Tris/Borate/EDTA agarose gel and run at 120V for 1.25 hours.

2.4.5 Characterization of ApA cleavage products by HPLC

In-line cleavage reagents were prepared as previously described in the anoxic chamber. In duplicate reactions, 0.5 mM ApA RNA dinucleotide (5’ to 3’; TriLink BioTechnologies) was suspended in degassed 20 mM HEPES/NaOH pH 7.6, 30 mM

KCl, 5% v/v glycerol, and combined with either water, 25 mM $MgCl_2$ or $FeCl_2$ (final concentration). Reactions were placed on a 37°C heat block with aliquots removed at 0, 0.25, 0.5, 1, 2, 4, and 8 days for no M^{2+} and Mg^{2+} samples and at 0, 0.25, 0.5, 1, and 2 days for Fe^{2+} samples. Aliquots were immediately quenched with 100 mM final concentration sodium phosphate pH 7.6, centrifuged at 2,000 × g for 1 minute, and the ApA-containing supernatant was collected to avoid transfer of Fe or Mg phosphate precipitate to the HPLC column. The samples were stored at -80°C prior to placement in the HPLC where they were held at 4°C. HPLC analyses were conducted on an Agilent 1260 Infinity HPLC with DAD UV-vis detector, with a path length of 1.0 cm. Products of the reactions were separated using a Kinetex XB-C18 column (150 × 2.1 mm, 2.6 μm particle size). The flow rate was 0.3 mL min^{-1} and the column temperature was held at 25°C. The mobile phase was water (0.1% formic acid) /acetonitrile. The gradient started with 100% water for the first 5 minutes and ramped to 55% acetonitrile over 25 minutes. The acetonitrile concentration was then ramped to 100% and was held as such for 10 minutes before returning to 100% water for column equilibration for 15 min. We recorded the elution at 210 nm, 220 nm, and 260 nm wavelengths, with a 180-400 nm spectrum detected in 2nm steps. To characterize reaction products, standards were spiked into product mixtures. The spiked standards were 0.5 mM ApA in 20 mM HEPES pH 7.6, 30 mM KCl, 5% v/v glycerol with either water, 2.5 μM adenosine, 3'-adenosine monophosphate, or 2',3'-cyclic adenosine monophosphate.

2.4.6 Characterization of ApA cleavage products by LC-MS

ApA was anoxically resuspended at 0.5 mM with 20 mM HEPES pH 7.6, 30 mM KCl, 5% v/v glycerol, and 25 mM $FeCl_2$, and then incubated at 37°C for 2 days. The

sample was analyzed by liquid chromatography mass spectrometry using and Agilent 1290 HPLC pump and thermostat; Agilent 1260 Autosampler and DAD UV-vis detector; path length: 0.6 cm; Agilent 1260 quaternary pump and RID; column: Phenomenex Kinetex 2.6 mmxB-C18100Å, LC column 150x2.1mm; column temp: 25°C; 10 µL injection with needle wash, 100 µL s^{-1} injection speed. The solvents were A) 0.1% formic acid in LC-MS grade water, and B) LC-MS grade acetonitrile a flow rates of 0.3 mL min^{-1}; gradient: 5 min 100% A, 0% B; 20 min ramp to 45% A, 55% B; 10 min 0% A, 100% B; 1 min ramp 100% A, 0% B; 9 min 100% A, 0% B. Elutions were recorded at 210, 220 and 260 nm, with the entire spectrum (180-400 nm) detected in 2 nm steps. This system was coupled to an Agilent 6130 single quad MS Electrospray Ionization Mass Spectrometry system with scanning of ±65 to ±2000 m/z and capillary voltage of 2.0kV.

2.4.7 Cell culture and harvesting

Culturing media consisted of LB broth (10 g L^{-1} NaCl, 10 g L^{-1} tryptone, 5 g L^{-1} yeast extract) amended with 4 mM tricine, 50 mM sodium fumarate, and 80 mM 3-(N-morpholino)propanesulfonic acid (MOPS; titrated with NaOH to pH 7.8). Fifty mL cultures containing all of these ingredients plus 0.25% v/v glycerol were inoculated from glycerol stocks of *Escherichia coli* MRE600 cells and shaken overnight at 37°C with or without O_2 and with either 1 mM $FeCl_2$ or ambient Fe^{2+} [6-9 µM, measured by the ferrozine assay (130)]. Two mL of each overnight culture was used to inoculate 1-L cultures in the same conditions. These cultures were then orbitally shaken at 37°C to OD_{600} 0.6-0.7. Aerobic cultures were grown in foil-covered Erlenmeyer flasks. Anaerobic fumarate-respiring cultures were inoculated into stoppered glass bottles containing medium that had been degassed with N_2 for one hour to remove O_2. Cells were then

harvested by centrifugation at 4,415 × g for 10 minutes, washed in 20 mL buffer containing 10 mM Tris pH 7.4, 30 mM NaCl, and 1 mM EDTA, and pelleted at 10,000 × g for 10 minutes. Cell pellets were stored at -80°C until ribosome purification.

2.4.8 Ribosome purification

The ribosome purification procedure was modified from Maguire et. al (131). All purification steps were performed in a Coy anoxic chamber (97% Ar, 3% H_2 headspace) unless otherwise noted. Buffers varied in their metal cation content. The typical wash buffer contained 100 mM NH_4Cl, 0.5 mM EDTA, 3 mM β-mercaptoethanol, 20 mM Tris pH 7.5, 3 mM $MgCl_2$, and 22 mM NaCl. For "Fe purification" experiments, buffer was composed of 100 mM NH_4Cl, 0.5 mM EDTA, 3 mM β-mercaptoethanol, 20 mM Tris pH 7.5, 1 mM $FeCl_2$ and 28 mM NaCl. Sodium chloride concentrations were increased here to maintain the ionic strength of the buffer (131 mM). Elution buffers contained the same composition as the wash buffer except for NH_4Cl (300 mM). Frozen cell pellets were resuspended in ribosome wash buffer and lysed in a BeadBug microtube compact homogenizer using 0.5 mm diameter zirconium beads (Benchmark Scientific). Cell lysate was transferred into centrifuge bottles inside the anoxic chamber which were tightly sealed to prevent O_2 contamination. Cell debris were removed by centrifuging outside of the anoxic chamber at 30,000 × g for 30 minutes at 4°C. The soluble lysate was then transferred back into the chamber and loaded onto a column containing pre-equilibrated, cysteine-linked, SulfoLink™ Coupling Resin (Thermo Fisher Scientific). The resin was washed with 10 column volumes of wash buffer. Ribosomes were eluted into three 10 mL fractions with elution buffer. Eluted fractions were pooled inside the anoxic chamber into ultracentrifuge bottles which were tightly sealed. Ribosomes were pelleted outside

the chamber by centrifuging at 302,000 × g for 3 hours at 4°C under vacuum in a Beckman Optima XPN-100 Ultracentrifuge using a Type 70 Ti rotor. Tubes containing ribosome pellets were brought back into the chamber and suspended in buffer containing 20 mM N-(2-hydroxyethyl)piperazine-N'-2-ethanesulfonic acid (HEPES; pH 7.6), 30 mM KCl, and 7 mM β-mercaptoethanol, heat-sealed in mylar bags, and stored at -80°C. Ribosome concentrations were calculated with a NanoDrop spectrophotometer assuming $1A_{260}$ = 60 μg ribosome mL^{-1} (conversion factor provided by New England Biolabs). This conversion factor was used to estimate the molecular mass of bacterial ribosomes, from which molarity was calculated. Biological triplicates of each growth and purification method were taken for downstream analyses.

2.4.9 Ribosomal Fe content

Purified ribosomes were analyzed for iron content by total reflection X-ray fluorescence spectroscopy (TRXF) as described in Bray and Lenz et al (94).

2.4.10 rProtein electrophoresis

For SDS-PAGE, purified ribosomes were normalized to 3.33 mg mL^{-1} in 2X SDS-PAGE dye, heated at 95°C for 5 minutes, and then incubated on ice for 2 minutes. Samples were loaded onto a 12% SDS acrylamide gel with a 4% stacking gel and run at 180 V for 60 minutes.

2.4.11 In vitro translation

Translation reactions were based on the methods of Bray and Lenz et al. (94) with minor modifications. All 15 μL reactions contained 2.25 μL of purified ribosome samples

normalized to 9 μg μL^{-1} (so that the final concentration of ribosomes in our reactions was 1.35 μg μL^{-1}), 0.1 mM amino acid mix, 0.2 mM tRNAs, ~0.2 μg μL^{-1} of dihydrofolate reductase mRNA, and 3 μL of factor mix (with RNA polymerase, and transcription/translation factors in 10 mM Mg^{2+}) from the PURExpress® Δ Ribosome Kit (New England Biolabs). The reaction buffer was based on Shimizu et al. (132), with HEPES instead of phosphate buffer to avoid precipitation of metal phosphates. Buffer consisted of 20 mM HEPES (pH 7.3), 95 mM potassium glutamate, 5 mM NH_4Cl, 0.5 mM $CaCl_2$, 1 mM spermidine, 8 mM putrescine, 1 mM dithiothreitol (DTT), 2 mM adenosine triphosphate (ATP), 2 mM guanosine triphosphate (GTP), 1 mM uridine triphosphate (UTP), 1 mM cytidine triphosphate (CTP), 10 mM creatine phosphate (CP), and 53 μM 10-formyltetrahydrofolate. Divalent cation salts ($MgCl_2$ or $FeCl_2$) were added to 9 mM final concentration. The reaction buffer was lyophilized and stored at -80°C until resuspension in anoxic nuclease-free water immediately before experiments in the anoxic chamber. Reaction mixtures were assembled in the anoxic chamber and run at 37°C in a heat block for 120 minutes. Reactions were quenched on ice to terminate translation (132) and stored on ice until they were assayed for the extent of protein synthesis. Protein synthesis was measured using a DHFR assay kit (Sigma-Aldrich), which measures the oxidation of NADPH (60 mM) to $NADP^+$ by dihydrofolic acid (51 μM). Assays were performed by adding 5 μL of protein synthesis reaction to 995 μL of 1X assay buffer. The NADPH absorbance peak at 340 nm (Abs_{340}) was measured in 15 s intervals over 2.5 minutes. The slope of the linear regression of Abs_{340} vs. time was used to estimate protein activity (Abs_{340} min^{-1}).

2.4.12 Protein characterization by LC-MS/MS

After ribosomal purification, samples were reduced with β-mercaptoethanol, and then alkylated with 14 mM iodoacetamide (HEPES, pH 7.6) for 30 minutes at room temperature in the dark. Alkylation was quenched with 5 mM dithiothreitol for 15 minutes at room temperature in the dark. Proteins were purified by the methanol/chloroform precipitation method and were then digested with trypsin in a buffer containing 5% acetonitrile, 1.6 M urea, and 50 mM HEPES pH 8.8 at 37°C with shaking overnight. The digestion was quenched with addition of trifluoroacetic acid to a final concentration of ~0.2%. Peptides were purified by Stage-Tip (133) prior to LC-MS/MS analysis.

Peptides were dissolved in a solution containing 5% acetonitrile and 4% formic acid and loaded onto a C18-packed microcapillary column (Magic C18AQ, 3 μm, 200 Å, 75 μm × 16 cm, Michrom Bioresources) by a Dionex WPS-3000TPL RS autosampler (Thermostatted Pulled Loop Rapid Separation Nano/Capillary Autosampler). Peptides were separated by a Dionex UltiMate 3000 UHPLC system (Thermo Scientific) using a 112-minute gradient of 4-17% acetonitrile containing 0.125% formic acid. The LC was coupled to an LTQ Orbitrap Elite Hybrid Mass Spectrometer (Thermo Scientific) with Xcalibur software (version 3.0.63). MS analysis was performed with the data dependent Top15 method; for each cycle, a full MS scan with 60,000 resolution and 1×10^6 AGC (automatic gain control) target in the Orbitrap cell was followed by up to 15 MS/MS scans in the Orbitrap cell for the most intense ions. Selected ions were excluded from further sequencing for 90 seconds. Ions with single or unassigned charge were not sequenced. Maximum ion accumulation time was 1,000 ms for each full MS scan, and 50 ms for each MS/MS scan.

Raw MS files were analyzed by MaxQuant (version 1.6.2.3) (134). MS spectra were searched against the *E. coli* database from UniProt containing common contaminants using the integrated Andromeda search engine (135). Due to the unavailability of the proteome database for *E. coli* strain MRE-600, the database for strain K12 was used. It has been shown that the two strains have nearly identical ribosome associated proteins (136). All samples were searched separately and set as individual experiments. Default parameters in MaxQuant were used, except the maximum number of missed cleavages was set at 3. Label-free quantification was enabled with the LFQ minimum ratio count of 1. The match-between-runs option was enabled. The false discovery rates (FDR) were kept at 0.01 at both the peptide and protein levels.

The results were processed using Perseus software (137). In the final dataset, the reverse hits and contaminants were removed. The LFQ intensity of each protein from the proteinGroups table was extracted and reported. For the volcano plots showing differential regulation of proteins, the ratios used were from the LFQ intensities of samples from each of the three experiments. The cutoff for differential expression was set at 2-fold. P-values were calculated using a two-sided T-test on biological triplicate measurements with the threshold p-value of 0.05 for significant regulation. The raw files are publicly available at http://www.peptideatlas.org/PASS/PASS01418 (username: PASS01418 and password: ZW2939nnw).

2.5 Results

2.5.1 In-line cleavage of rRNA: Mg^{2+} and anoxic Fe^{2+}

By manipulating reaction conditions, we could switch the mode of rRNA cleavage between Fenton and in-line mechanisms. In-line is the only possible mechanism of cleavage by Mg^{2+} due to its fixed oxidation state and inability to generate hydroxyl radicals. We confirm the expectation that Mg^{2+}-mediated in-line cleavage reactions are not inhibited by anoxia or hydroxyl radical quenchers (Figure A.2).

We confirm here in a variety of experiments that RNA is degraded by in-line cleavage when incubated with Fe^{2+} under anoxic conditions (Figure 2.1a). Most of the experiments employed the rRNA of *E. coli* as substrate. A shorter RNA [a-RNA (129)] showed on a higher size resolution gel that RNA banding patterns and reaction products were nearly identical for Mg^{2+} and anoxic Fe^{2+} reactions (Figure 2.2), indicating that preferred sites of cleavage are the same for both metals. Common sites of cleavage are indications of common mechanisms of cleavage (114). Neither Mg^{2+} nor anoxic Fe^{2+} cleavage was inhibited by glycerol (5%), which is known to quench hydroxyl radical and to inhibit hydroxyl radical cleavage (138). By contrast, glycerol inhibited cleavage by Fe^{2+} under conditions that favor Fenton-type cleavage (Figure A.3). Glycerol did not inhibit Mg^{2+} in-line cleavage under any conditions (Figure 2.2).

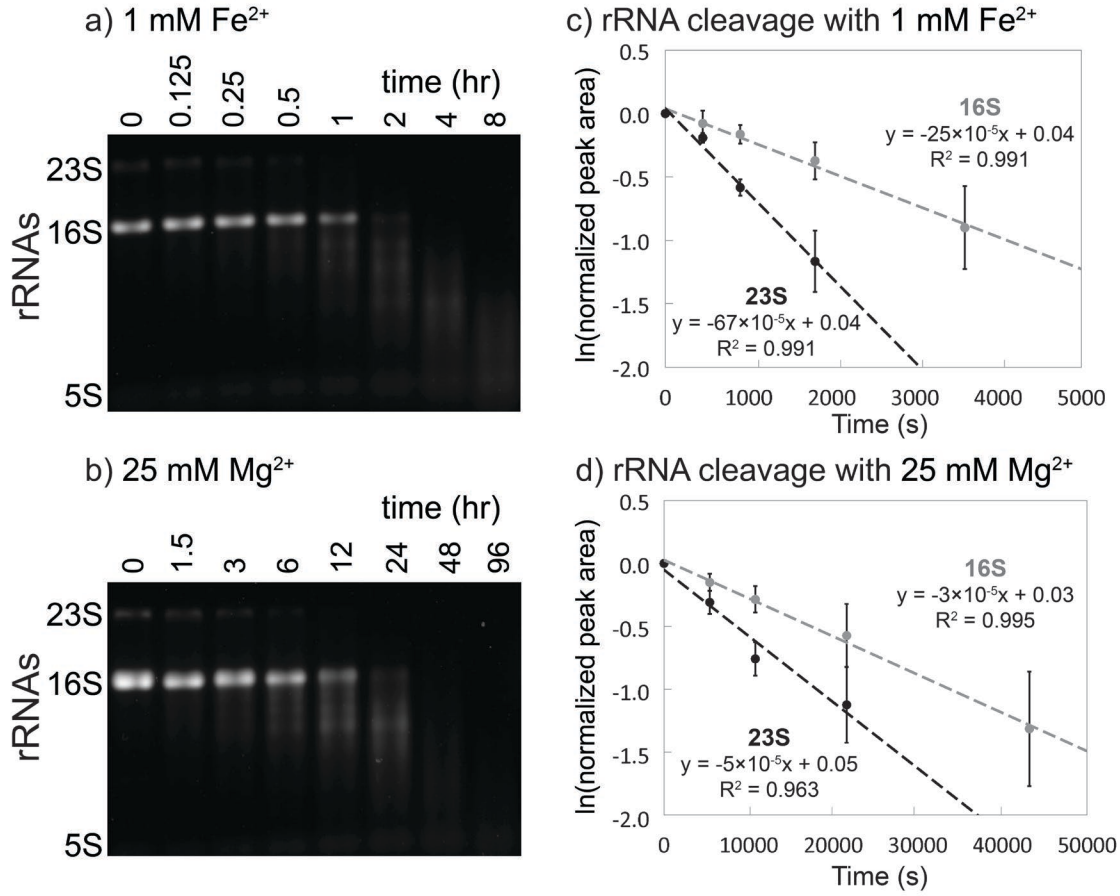

Figure 2.1 – In-line cleavage of rRNA in anoxia. In-line cleavage of purified rRNAs with a) 1 mM Fe^{2+} (0-8 hr) and b) 25 mM Mg^{2+} (0-96 hr). Reactions were conducted in an anoxic chamber at 37°C in the presence of the hydroxyl radical quencher glycerol (5% v/v) and were analyzed by 1% agarose gels. Pseudo first-order rate plots were extracted from 23S and 16S band intensity for c) 1 mM Fe^{2+} and d) 25 mM Mg^{2+} conditions. The Mg^{2+} time axis is 10 times greater than the Fe^{2+} time axis. Error bars represent the S.E.M. (n = 3). Figure in Ref. (98).

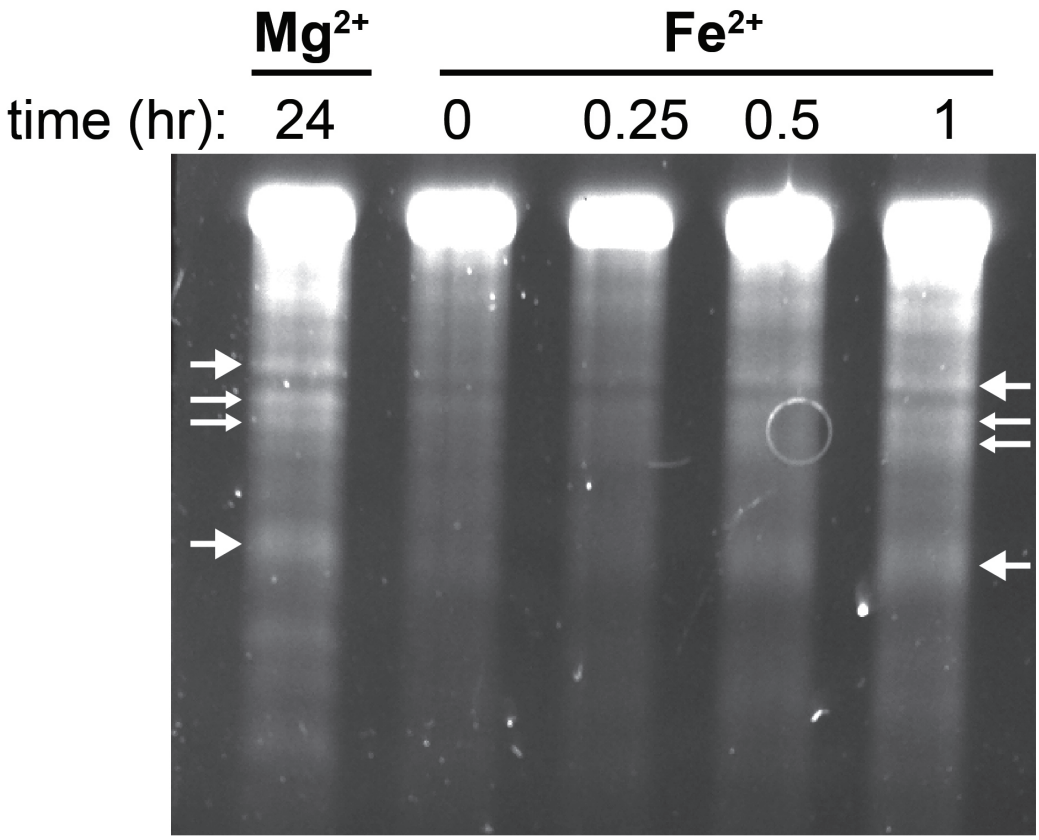

Figure 2.2 – In-line cleavage banding patterns are the same for rRNA cleavage with Mg^{2+} and anoxic Fe^{2+}. Several primary cleavage bands of a-rRNA (129) are indicated by arrows. This gel is 6% polyacrylamide, 8 M urea showing in-line cleavage mediated by 1 mM Mg^{2+} or 1 mM anoxic Fe^{2+} at 37°C for varying amounts of time. Reactions were run in 20 mM Tris-HEPES, pH 7.2. Figure in Ref. (98).

In the absence of O_2, cleavage rates are significantly greater for Fe^{2+} than for Mg^{2+}. For 16S and 23S rRNAs, 1 mM Fe^{2+} caused significant in-line cleavage of rRNA after 30 minutes at 37°C. Both rRNAs were completely degraded after 2 hours in anoxic Fe^{2+} (Figure 2.1a). By contrast, when the M^{2+} ion was switched from 1 mM Fe^{2+} to 25 mM Mg^{2+}, only a modest amount of in-line cleavage was observed after 6 hours (Figure 2.1b). Fitting of the data to a pseudo first-order rate model (Figure 2.1 c and d) reveals apparent rate constants for cleavage of the full-length 23S rRNA with Fe^{2+} is 67×10^{-5} s^{-1}

and with Mg^{2+} is 5×10^{-5} s^{-1}. The rate constants for cleavage of the 16S rRNA is 25×10^{-5} s^{-1} for Fe^{2+} and 3×10^{-5} s^{-1} for Mg^{2+} (Table 2.1). These apparent rate constants do not account for differences in metal concentration or in RNA length.

Table 2.1 – rRNA cleavage pseudo first-order rate constants

Metal	rRNA	k_{obs} (10^{-5} s^{-1})	S.E.M. (10^{-5} s^{-1})
1 mM Fe^{2+}			
	23S	67	12
	16S	25	8.2
25 mM Mg^{2+}			
	23S	5	1.1
	16S	3	0.8

In sum, reactions with Mg^{2+} and anoxic Fe^{2+} showed a lack of inhibition by a hydroxyl radical quencher. By contrast, the quencher inhibited reactions with Fe^{2+} in the presence of O_2. The observed rate constant for in-line cleavage for rRNA is ~10 times greater for 1 mM Fe^{2+} than for 25 mM Mg^{2+}. Under these conditions, in-line cleavage is expected to scale with metal concentration (127,128) so that that the reaction rate constant, k (M^{-1} s^{-1}), is increased with Fe^{2+} by ~300 times for the 23S and by ~200 times for the 16S. We demonstrate that although Fe^{2+} interacts in the same way as Mg^{2+} with RNA, the cleavage potency of Fe^{2+} is greatly enhanced.

2.5.2 Characterization of in-line cleavage reaction products

To confirm that Fe^{2+} catalyzes non-oxidative in-line RNA cleavage, a series of cleavage reactions were performed on the dinucleotide ApA. The products of the reaction were characterized by HPLC via spiking with standards, and by LC-MS. A small RNA with only one possible cleavage site allowed us to identify specific cleavage products,

which report on the mechanism of scission. In-line cleavage leads to 2',3'-cyclic phosphate upstream of the scission site and a downstream 5'OH RNA fragment. Subsequently, the 2',3'-cyclic phosphate can hydrolyze to either a 2' or 3' monophosphate. Conversely, oxidative cleavage of RNA by a hydroxyl radical that may be formed during iron oxidative processes abstracts a proton from a ribose sugar leading to a variety of products but not 2',3'-cyclic phosphate, 2'-phosphate, or 3'-phosphate RNA fragment (91). Anoxic incubation of ApA with 25 mM Mg^{2+} or Fe^{2+} produces adenosine, 2',3'-cyclic adenosine monophosphate (2',3'-cAMP), and 3'-adenosine monophosphate (3'-AMP) (Figure 2.3 a-d and Figure A.4**)**. The repertoire of products is matched for the two metals, pointing to a common in-line cleavage mechanism.

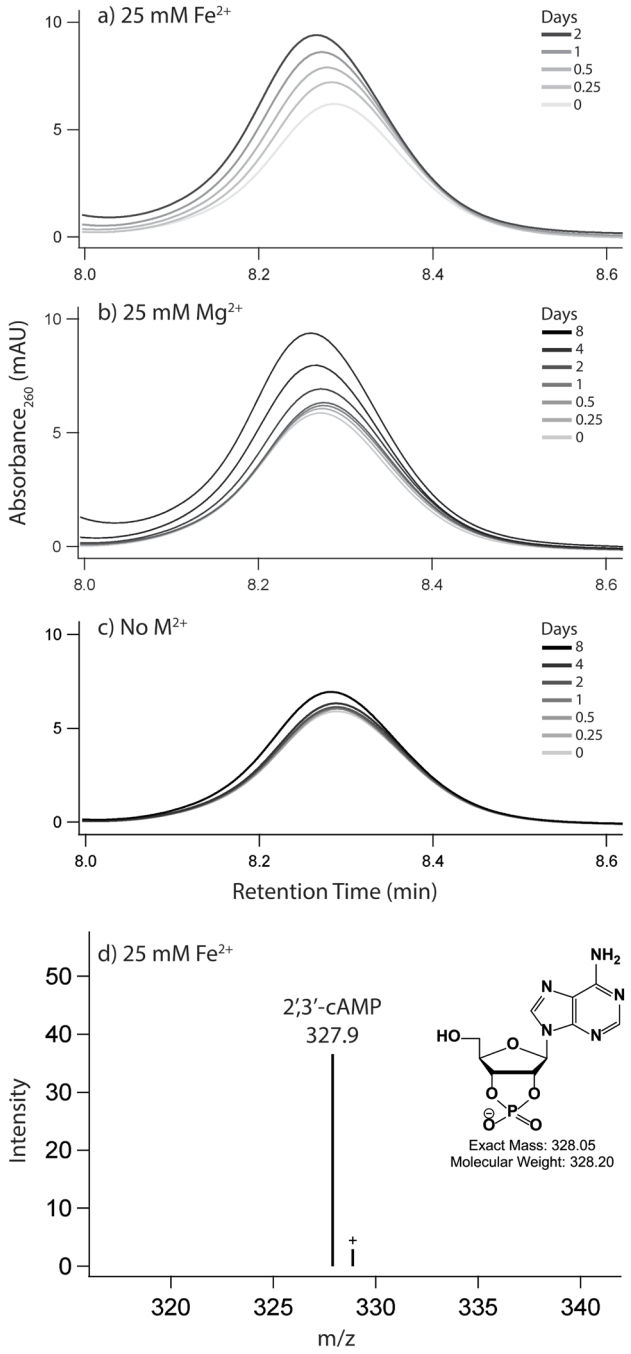

Figure 2.3 – 2',3'-cAMP is formed upon incubation of ApA with Fe^{2+} or Mg^{2+}. HPLC chromatograms show the accumulation of 2',3'-cAMP, a direct product of an in-line cleavage mechanism, upon incubation of ApA with either a) 25 mM Fe^{2+}, b) 25 mM Mg^{2+}, or c) no metal for the negative control. Panel d shows identification of the 2',3'-cyclic adenosine monophosphate by LC-MS of ApA incubated with 25 mM Fe^{2+} for 2 days. Labeled species correspond to $[M-H]^-$ ions. Reactions were incubated anoxically at 37°C in the presence of 5% (v/v) glycerol. Figure in Ref. (98).

2.5.3 M^{2+} exchange during ribosomal purification

We hypothesized that O_2 and Fe^{2+} content during bacterial growth could affect the iron content of ribosomes. However, the vast majority of ribosomal M^{2+} ions are exchangeable (139) and canonical ribosome purification procedures use high Mg^{2+} buffers (140) to maintain folding and stability. Therefore, spontaneous exchange of *in vivo* bound M^{2+} with those in the buffer occurs during purification, suggesting that the final Fe^{2+} content of purified ribosomes depends on the type of M^{2+} in the purification buffer. Indeed, ribosomes purified in solutions with 1 mM Fe^{2+} contained significantly higher Fe^{2+} than those purified in 3 mM Mg^{2+} regardless of growth condition (Figure 2.4). All ribosome samples purified in 1 mM Fe^{2+} contained similar Fe^{2+} (~400-600 mol Fe mol^{-1} ribosome). These results show that the vast majority of ribosomal M^{2+} ions are exchangeable and that M^{2+} exchange takes place during purification.

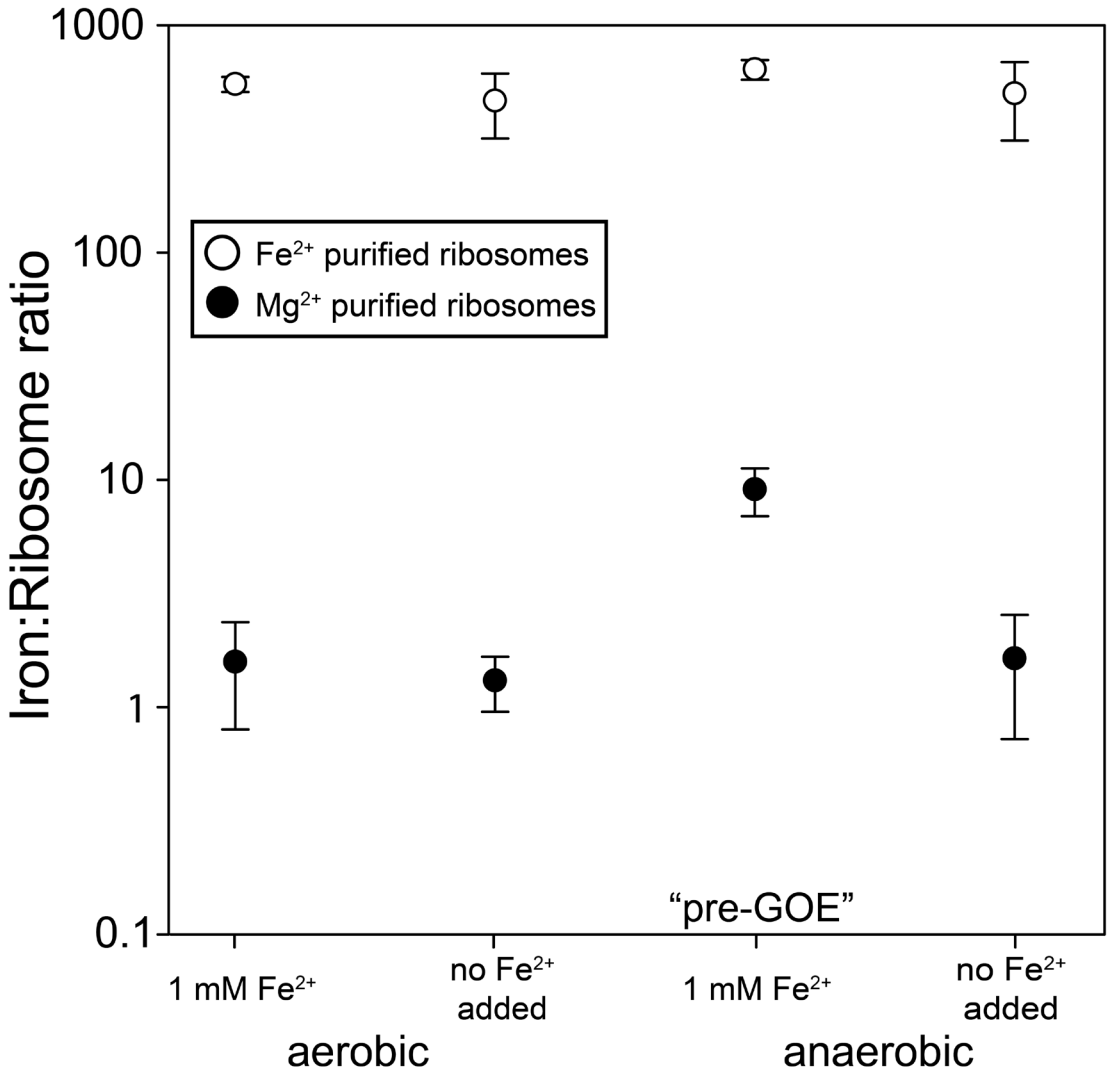

Figure 2.4 – Iron content (mol Fe mol^{-1} ribosome) of purified ribosomes. *E. coli* were grown aerobically or anaerobically at 1 mM Fe^{2+} or ambient Fe^{2+} (6-9 μM, no Fe added), and purified in buffers containing either 3 mM Mg^{2+} (black circles) or 1 mM Fe^{2+} (white circles). Error bars represent the S.E.M. (n=3). Figure in Ref. (98).

2.5.4 M^{2+} exchange during ribosomal purification

A small subset of ribosomal M^{2+} ions are not exchangeable during purification. Ribosomes retain this subset of *in vivo* divalent cations after purification. We harvested *E. coli* in log phase from four growth conditions: oxic or anoxic with high Fe^{2+} in the

medium (1 mM Fe^{2+}), and oxic or anoxic without added Fe^{2+} in the growth medium (6-9 μM Fe^{2+}). Ribosomes from *E. coli* grown in pre-GOE conditions (anoxic, high Fe^{2+}) contained quantitatively reproducible elevated levels of Fe^{2+} after purification in solutions containing Mg^{2+}. We detected around 9 mol Fe mol^{-1} ribosome from cells grown in pre-GOE conditions purified in solutions with high Mg^{2+} (Figure 2.4). The three other growth conditions yielded ribosomes containing near background levels of Fe^{2+} (< 2 mol Fe mol^{-1} ribosome).

2.5.5 Quantitating translation

Ribosomes from all four growth conditions produced active protein in translation assays. Ribosomes were functional *in vitro* under standard conditions (with 10 mM Mg^{2+}) and also in 8 mM Fe^{2+} + 2 mM Mg^{2+} under anoxia. Regardless of whether translation activity was assayed in the presence of 10 mM Mg^{2+} or 8 mM Fe^{2+} + 2 mM Mg^{2+}, ribosomes synthesized aerobically in the absence of Fe^{2+} have higher activity than the ribosomes synthesized anaerobically in the absence of Fe^{2+} ($p< 0.08$; Figure A.5). The presence of 1 mM Fe^{2+} in the bacterial growth conditions did not affect ribosomal activity; the only differences are whether growth conditions are aerobic or anaerobic, and whether 10 mM Mg^{2+} or 8 mM Fe^{2+} + 2 mM Mg^{2+} are used in the assay. Translation was reduced in the presence of Fe^{2+} compared to Mg^{2+}, consistent with our previous work (94). The translational activity of ribosomes harvested from anaerobic cells was slightly less than from those from aerobic cells. Ribosomes from all four growth conditions contained intact 23S, 16S, and 5S rRNAs with purification in 3 mM Mg^{2+} (Figure 2.5a) resulting in a higher proportion of intact rRNA relative to purification in 1 mM Fe^{2+} (Figure 2.5b). Each purification also contained a full suite of rProteins as indicated by

mass spectrometric analysis and by gel electrophoresis (Figure A.6). The protein composition of ribosomes from 1 mM Fe^{2+} growth conditions (Figure A.6b) was similar to that from Mg^{2+} growth conditions (Figure A.6a).

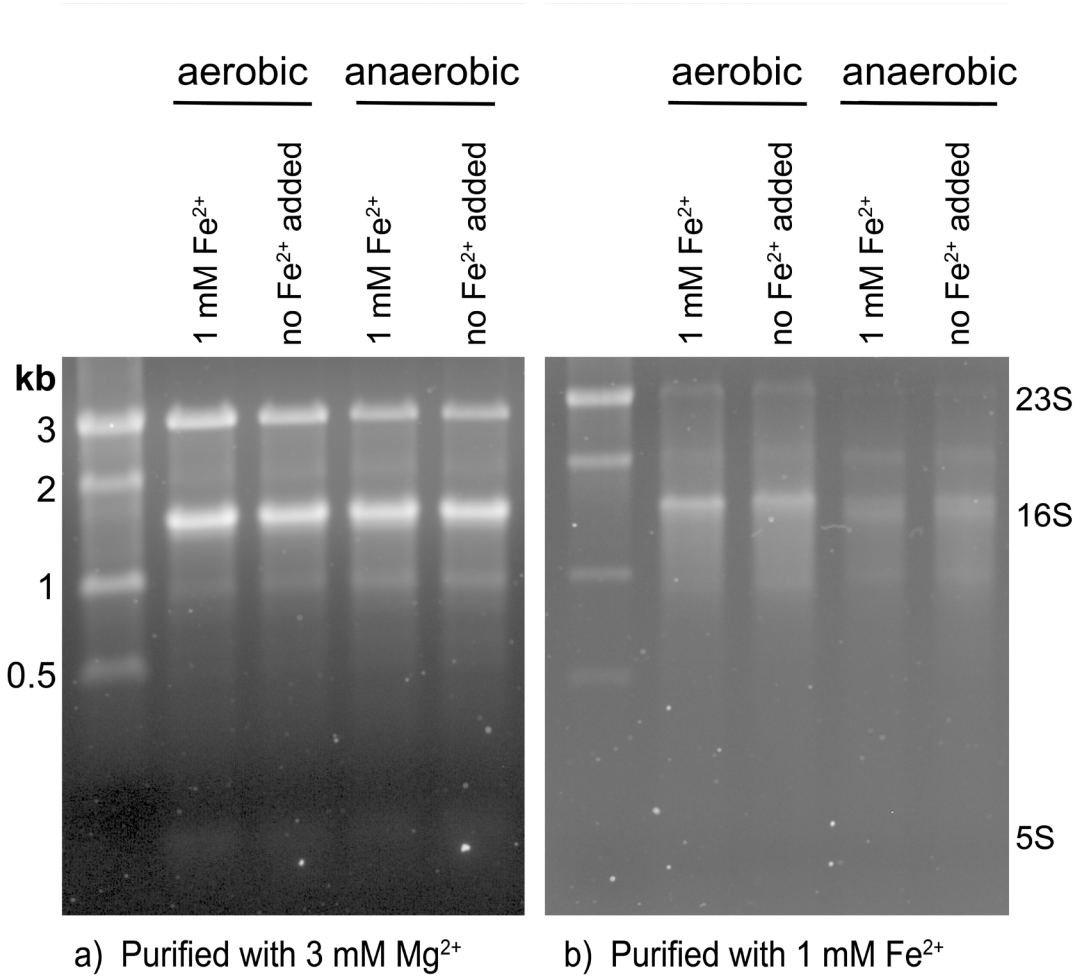

Figure 2.5 – 1% agarose gels showing rRNA from ribosomes purified in (a) 3 mM Mg^{2+} and (b) 1 mM Fe^{2+}. The banding pattern suggests that rRNA is relatively more intact in ribosomes purified with 3 mM Mg^{2+} than in ribosomes purified with 1 mM Fe^{2+}. Figure in Ref. (98).

2.5.6 rProtein characterization

In addition to oxidative mechanism, our results pointed to a non-oxidative cleavage mechanism of RNA with Fe^{2+}. So, we next asked whether ribosomes might adopt different proteins to cope with high Fe^{2+} in both oxic and anoxic conditions. Ribosomes under all four growth conditions contained a full repertoire of rProteins, and were associated with additional proteins, as determined by mass spectrometry. These non-ribosomal proteins ranged in function from translation to central metabolism. Proteins from anaerobic pathways were generally more abundant in ribosomes from anaerobic cells while proteins from aerobic pathways were more abundant in ribosomes from aerobic cells (Table A.1; Table A.2). Proteins for synthesis of enterobactin, an Fe^{3+}-binding siderophore, were more abundant in ribosomes from aerobic cells and from those grown without the addition of Fe, while the bacterial non-heme ferritin subunit was more abundant in ribosomes from anaerobic cells regardless of the Fe^{2+} content in the media (Table A.2). Several proteins were differentially expressed in ribosomes grown in pre-GOE conditions relative to other growth conditions (Figure A.7). Notably, ribosomes grown anaerobically with high Fe^{2+} had five times the abundance of the protein YceD than ribosomes grown anaerobically without added Fe^{2+}. Anaerobic high Fe^{2+} ribosomes had one third the abundance of the rProtein S12 methylthiotransferase protein RimO and rRNA LSU methyltransferase K/L protein RlmL than ribosomes from aerobically grown cells with 1 mM Fe^{2+}.

2.6 Discussion

2.6.1 Iron promotes rapid in-line cleavage of rRNA

Mg^{2+} is known to cleave the RNA phosphodiester backbone via an in-line mechanism (64,114). We have shown here that Fe^{2+}, like Mg^{2+}, can cleave RNA by a non-oxidative in-line mechanism. We used cleavage of 23S and 16S rRNA to determine the observed rate constants of both Mg^{2+}- and Fe^{2+}- mediated cleavage. The k_{obs}, uncorrected for metal concentration, for in-line cleavage by Fe^{2+} is around 10 times greater than for Mg^{2+}. Previous studies of metal concentration effects on k_{obs} suggest that in-line cleavage is first-order with respect to metal concentration (127,128), allowing the calculation of a per molar metal reaction rate constant by $k = k_{obs}/[M^{2+}]$. Assuming this first-order relationship in our experiments, k with Fe^{2+} is ~300 times greater for the 23S and ~200 times greater for the 16S than with Mg^{2+}. In Table 2.4 we compare our results to literature k values of Mg^{2+} and Zn^{2+} in-line cleavage taken under a range of conditions (127,128,141-145), normalizing for the number of cleavable phosphates in the RNA substrate. Changes in metal identity, RNA length, RNA folding, pH, and temperature, result in differences in normalized rate constants. The values extend over four orders of magnitude. Rate enhancement by switching Mg^{2+} to another metal while other conditions are held constant is greater for Fe^{2+} than for Zn^{2+}, highlighting the rapidity of cleavage by Fe^{2+}.

Support for a non-oxidative in-line mechanism of cleavage of RNA by anoxic Fe^{2+} is provided by observations that the rate of the reaction is not attenuated by anoxia and that the sites of cleavage appear to be conserved for Mg^{2+} and anoxic Fe^{2+}. The absence of hydroxyl radical intermediates in the anoxic cleavage reaction is confirmed by the lack of inhibition by a hydroxyl radical quencher known to inhibit Fenton chemistry (122). Cleavage products of the RNA dinucleotide ApA include only those that are

expected from an in-line mechanism and align with products formed with Mg^{2+}. Among these is 2',3'-cyclic phosphate, the hallmark of in-line attack of the bridging phosphate by the 2'OH.

In-line cleavage is the dominant mechanism of Fe^{2+} cleavage when contributions from Fenton-mediated processes are minimized and is the only mechanism of Mg^{2+} cleavage. By contrast, in oxic environments, transient Fe^{2+} oxidation generates hydroxyl radicals (121) that cleave nucleic acids (120,122-125). Our results have significant implications for iron toxicity and human disease. The potency of Fe^{2+} in inducing rRNA cleavage may lead to decreased longevity of Fe^{2+}-containing ribosomes. In fact, rRNA cleavage linked to Fe^{2+} oxidation, as in the human ribosome in Alzheimer's disease (146), or in yeast rRNA (147), could be in some measure attributable to Fe^{2+} in-line cleavage.

Fe^{2+} appears to be a potent all-around cofactor for nucleic acids. The combined results indicate that:

a) rRNA folds at lower concentration of Fe^{2+} than Mg^{2+} (94),
b) at least a subset of ribozymes and DNAzymes are more active in Fe^{2+} than in Mg^{2+} (92,148),
c) the translation system is functional when Fe^{2+} is the dominant divalent cation (94),
d) at low concentrations of M^{2+}, T7 RNA polymerase is more active with Fe^{2+} than with Mg^{2+} (95),

e) a broad variety of nucleic acid processing enzymes are active with Fe^{2+} instead of Mg^{2+} (95),

f) rates of in-line cleavage are significantly greater for Fe^{2+} than for Mg^{2+} (here), and

g) Fe^{2+} but not Mg^{2+} confers oxidoreductase functionality to some RNAs (49,109).

2.6.2 Why so fast?

Our previous DFT computations (95) help explain why Fe^{2+} is such a potent cofactor for RNA. Conformations and geometries of coordination complexes with water and/or phosphate are nearly identical for Fe^{2+} or Mg^{2+}. However, differences between Mg^{2+} and Fe^{2+} are seen in the electronic structures of coordination complexes.

Firstly, because of low lying d orbitals, Fe^{2+} has greater electron withdrawing power than Mg^{2+} from first shell phosphate ligands. In coordination complexes with phosphate groups, the phosphorus atom is a better electrophile when $M^{2+} = Fe^{2+}$ than when $M^{2+} = Mg^{2+}$. This difference between Mg^{2+} and Fe^{2+} is apparent in both ribozyme reactions and in-line cleavage reactions.

Secondly, $Fe^{2+}(H_2O)_6$ is a stronger acid than $Mg^{2+}(H_2O)_6$; depletion of electrons is greater from water molecules that coordinate Fe^{2+} than from those that coordinate Mg^{2+}. The lower pK_a of $Fe^{2+}(H_2O)_6$ may promote protonation of the 5'OH leaving group during cleavage. Metal hydrates with low pK_as have been reported to induce RNA cleavage better than less acidic metal hydrates (64).

In in-line cleavage, RNA coordinates M^{2+} or the M^{2+} hydrate (64,114). Indeed, studies of the in-line cleavage fragment patterns have previously been used to probe structural information on RNA molecules, such as metal-binding sites (116,117). We demonstrated with ApA that RNA secondary structure is not required for in-line cleavage. The same activities that drive in-line cleavage (e.g. 2'OH activation and coordination of the leaving group) are thought to occur in metal-catalyzed ribozyme cleavage (50). Multiple ribozymes (92) and DNAzymes (148) have been observed to function with Fe^{2+} as a cofactor. Our results with Fe^{2+} in-line cleavage, and in-line cleavage in general, require no enzymatic activity.

The remarkably high cleavage activity of Fe^{2+} with RNA demonstrated here bears relevance to prebiotic chemistry and early biochemistry. Because these reactions are catalytic, they increase both forward and reverse reaction rates. RNA degradation through Fe^{2+} cleavage should be weighed against potential RNA polymerization and the benefits of increased catalytic activity. The same dualism exists with Mg^{2+}, but our work suggests higher stakes with Fe^{2+}. At the extremes, without M^{2+}, RNA cannot form complex folds and has few avenues for catalytic or functional activity while with excessive M^{2+} RNA is degraded. There theoretically exists some point of balance wherein M^{2+} is beneficially utilized with some frequency of disabling cleavage. Given the increased potency of cleavage with Fe^{2+} relative to M^{2+}, this balancing point may be at a lower concentration of Fe^{2+} than Mg^{2+}. However, enhanced cofactor characteristics of Fe^{2+} may allow RNA to access more functions using less metal. On early Earth, heightened RNA cleavage in the presence of Fe^{2+} if balanced by a similar rate of RNA resupply would allow functional space to be explored in short time. RNAs would be selected that could cooperate with or

tolerate a potent metal. Fe^{2+} may have been a force for accelerated RNA evolution on early Earth.

2.6.3 Fe^{2+} associates with rRNA in vivo

Exchange of non-native metals for native metals is well-known during purification of proteins (139). We observe analogous phenomena with rRNA. Fe^{2+} can exchange with Mg^{2+} (and vice versa) during purification of ribosomes. Ribosomes purified in either Fe^{2+} or Mg^{2+} associate with 500-1000 M^{2+} ions that match the type of ion in the purification buffers. Our data support the tight association and lack of exchange of around 9 M^{2+} per ribosome. This subset of M^{2+} do not exchange during purification. The number of non-exchangeable M^{2+} closely matches the number of M^{2+} identified previously as a special class of deeply buried and highly coordinated M^{2+} in dinuclear microclusters (M^{2+}-μc's) (108). Mg^{2+} ions in M^{2+}-μc's are directly chelated by multiple phosphate oxygens of the rRNA backbone and are substantially dehydrated. M^{2+}-μc's within the LSU provide a framework for the ribosome's peptidyl transferase center, the site of protein synthesis in the ribosome, suggesting an essential and ancient role for M^{2+}-μc's in the ribosome. There are four dinuclear M^{2+}-μc's in the LSU and one in the SSU, accounting for 10 M^{2+} (108). Displacement of these M^{2+} would require large-scale changes in ribosomal conformation. In sum, there are ten M^{2+} per ribosome that are expected to be refractory to exchange. We hypothesize that this subset M^{2+} are contained in M^{2+} -μc's, which can be occupied by either Mg^{2+} or Fe^{2+} (109), depending on growth conditions.

We also hypothesize that ribosomes harvested from aerobic cells have low Fe^{2+}/Mg^{2+} ratios because of low intracellular Fe^{2+} availability and lability. This hypothesis is supported by our observation that the number of slow exchanging Fe^{2+} per ribosome from aerobic cells is near the baseline of our measurements. It appears that ribosomes harvested from pre-GOE conditions have high Fe^{2+}/Mg^{2+} ratios because of high intracellular Fe^{2+} availability and lability, as indicated by the close match in the number of slowly exchanging Fe^{2+} per ribosome and the number of available M^{2+} sites in ribosomal M^{2+}-μc's. In these experiments we detect only the Fe^{2+} ions that do not exchange during purification.

2.6.4 Summary

Here we have shown for the first time that bacteria grown in pre-GOE conditions contain functional ribosomes with tightly bound Fe atoms. The ~10 ribosomal Fe ions in ribosomes grown anoxically with high Fe^{2+} are likely deeply buried and specifically bound to rRNA. Depending on intracellular Fe lability, ribosomes may have higher Fe content *in vivo* given the high capacity for the ribosome to substitute ~600 loosely bound Mg^{2+} ions for Fe^{2+}. Furthermore, direct association of the rRNA with Fe atoms results in a fast rate of in-line cleavage. 1 mM Fe^{2+} gives a ~10 times higher k_{obs} than does 25 mM Mg^{2+} so that the assumed per molar metal rate constant is hundreds of times greater with Fe^{2+} than with Mg^{2+}. This highlights a potential role of protection from in-line cleavage for rProteins and suggests that Fe^{2+} may drive rapid cycling of RNA between monomers and polymers. Our results support a model in which alternate M^{2+} ions, namely Fe^{2+}, participated in the origin and early evolution of life: first in abiotic proto-biochemical systems, through potentially rapid rounds of formation and breakdown of RNA

structures, and then within early cellular life up until the GOE (93). Our study also expands the role of Fe^{2+} in modern biochemistry by showing that extant life retains the ability to incorporate Fe into ribosomes. We surmise that extant organisms under certain environmental and cellular states may use Fe^{2+} as a ribosomal cofactor. In addition, obligate anaerobic organisms that have spent the entirety of their evolutionary history in permanently anoxic environments may still use abundant Fe^{2+} in their ribosomes *in vivo*.

CHAPTER 3. GOLDILOCKS AND RNA: WHERE MG^{2+} IS JUST RIGHT

The work described in this chapter has been published in the journal *Nucleic Acids Research* (149). Experiments were performed by me and by A.M. Mohamed, with assistance from E.T. Cowan and A. Henning. I designed and performed the modeling, P4-P6 RNA cleavage, and tRNA and P4-P6 RNA folding experiments. A.M. Mohamed performed the tRNA and rU_{20} cleavage experiments and the rU_{20} folding experiment. The manuscript was written primarily by me with contributions from all coauthors.

3.1 Abstract

Magnesium, the most abundant divalent cation in cells, catalyzes RNA cleavage but also promotes RNA folding. Because folding can protect RNA from cleavage, we predicted a "Goldilocks peak", which is a local maximum in RNA lifetime at the Mg^{2+} concentration required for folding. Here we use simulation and experiment to discover an innate yet sophisticated mechanism of control of RNA lifetime. By simulation we characterized the RNA Goldilocks peak and its dependence on cleavage parameters and extent of folding. Supporting experiments with yeast $tRNA^{Phe}$ and *Tetrahymena* ribozyme P4-P6 domains show that structured RNA can inhabit a Goldilocks peak *in vitro*. The Goldilocks peaks are tunable by differences in cleavage rate constants, Mg^{2+} binding cooperativity, and Mg^{2+} affinity. Broad ranges of those folding and cleavage parameters produce Goldilocks peaks of different intensities. Goldilocks behavior allows ultrafine control of RNA chemical lifetime, whereas non-folding RNAs do not display a Goldilocks peak. In sum, the effects of Mg^{2+} on RNA persistence are expected to be pleomorphic, both protecting and degrading RNA. In evolutionary context, Goldilocks

behavior may have shaped RNA in an early Earth environment containing Mg^{2+} and other metals.

3.2 Introduction

Universal biopolymers (DNA, RNA, protein, and polysaccharide) are ephemeral (150,151). Biopolymers hydrolyze spontaneously in aqueous media, degrading to monomers. In dilute aqueous solution, hydrolysis of biopolymers is always thermodynamically favored (152-154). However, low rates of hydrolysis, due to kinetic trapping, allow biopolymers to persist for extended periods of time (150). RNA is especially labile (155), although rates of RNA hydrolysis are modulated by cations, sequence, folding, temperature, and proteins (156-158).

Here we document and characterize Goldilocks behavior of RNAs, with local maxima of chemical lifetimes bounded by conditions of lower lifetimes (Figure 3.1). A Goldilocks landscape is a continuum of conditions, some of which are just right for RNA persistence. We predicted Goldilocks landscapes for RNA because Mg^{2+} directly increases RNA cleavage rates by one mechanism and indirectly decreases cleavage rates by a different mechanism. Mg^{2+}, the most abundant divalent cation in cells (77), degrades RNA by catalyzing in-line attack of the 2'-oxygen on the backbone phosphate (64,98,128,145,156,159,160). Mg^{2+} can also protect against degradation, by facilitating RNA folding (47,48,79-81,161). The mechanism of protection involves converting conformationally flexible RNA to more structured RNA (162), which is less likely to adopt the geometry required for cleavage (114). A Goldilocks landscape can arise when a

given factor acts as a double-edged sword that differentially degrades and protects. Here, we investigated RNA Goldilocks behavior through simulation and experiment.

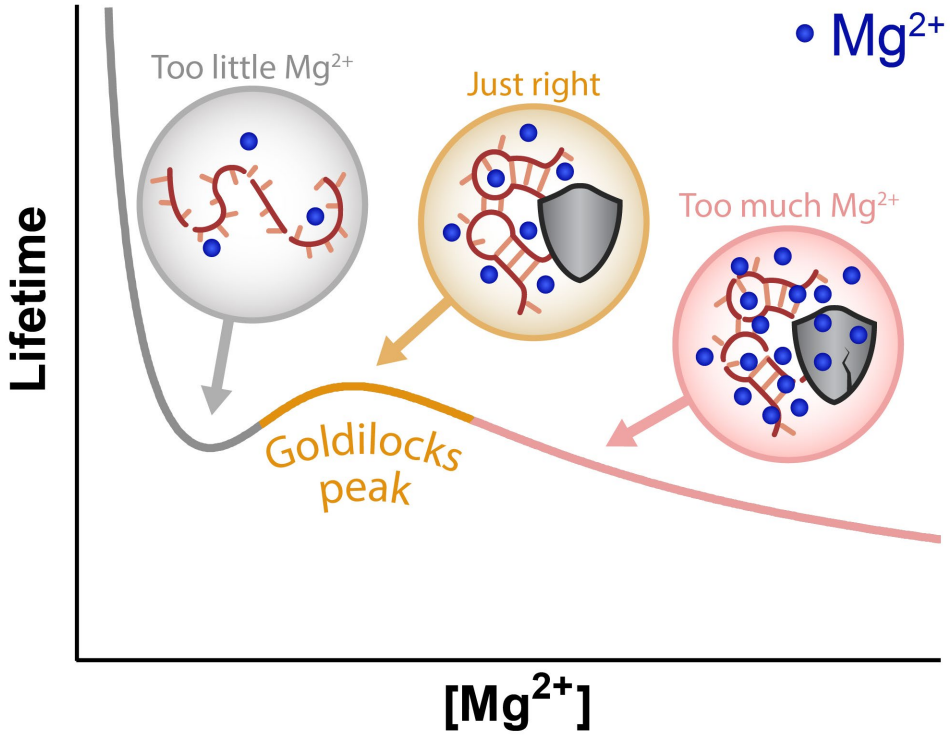

Figure 3.1 – The Goldilocks peak of RNA. Too little Mg^{2+} accelerates RNA cleavage by minimizing folding, a means of cleavage protection. Too much Mg^{2+} accelerates RNA cleavage by over-riding protection. The in-between Goldilocks peak of Mg^{2+} is just right. Figure from Ref. (149).

In simulations, Goldilocks behavior is observed under a broad variety of parameters that influence RNA folding and cleavage. Goldilocks landscapes are influenced by folding mechanism, Mg^{2+}-dependency of folding, and folded and unfolded cleavage rate constants. Goldilocks landscapes are not accessible to RNAs that do not fold or unfold.

In our experiments, Goldilocks behavior is observed for well-established model RNAs, yeast $tRNA^{Phe}$ (163,164) and *Tetrahymena* ribozyme P4–P6 domain (165,166).

An experimental comparison of tRNA and P4-P6 RNA indicates that the Goldilocks phenomena is retained even as the landscape is influenced by sequence and chemical modification. In experiments, Goldilocks peaks were observed where RNA is ~95% folded; a control RNA that does not fold, rU_{20} (polyuridylic acid 20-mer), does not display Goldilocks behavior.

Goldilocks behavior of RNA suggests intrinsic sophistication, allowing ultrafine control of structure and chemical lifetime by a variety of inputs (150,167). RNA chemical lifetimes can be tuned by Mg^{2+}-mediated shifts into and out of Goldilocks peaks and by remodeling Goldilocks landscapes via sequence and chemical modification. Goldilocks behavior of RNA is consistent with its selection in a primordial world of stringent and conflicting evolutionary demands.

3.3 Materials and Methods

3.3.1 Simulation of RNA lifetime

We mathematically modeled the effect of $[Mg^{2+}]$ on fraction of RNA folded and cleavage rate constants which together combine into an observed cleavage rate constant k_{obs}. Lifetime is then the reciprocal of k_{obs}.

For a two-state model, the fraction folded is f_f and the fraction unfolded is f_u. We used the Hill equation to describe extent of folding (168), although any model that reasonably describes RNA folding can be used (Equations 3.1 and 3.2):

$$f_f = \frac{1}{1 + \left(\frac{K_D}{[Mg^{2+}]}\right)^n} \tag{3.1}$$

$$f_f + f_u = 1 \quad \textbf{(3.2)}$$

K_D is equivalent to $[Mg^{2+}]$ at the folding midpoint (48) and n is the Hill coefficient, which reflects the cooperativity of RNA folding.

RNA cleavage is a second-order phenomenon in which the rate of cleavage depends on [RNA] and $[Mg^{2+}]$ (128,156). The observed pseudo first-order rate constant (k_{obs}) is proportional to the second-order rate constant (k) and $[Mg^{2+}]$ (Equation 3.3)(169):

$$k_{obs} = k[Mg^{2+}] \quad (3.3)$$

To model RNA lifetime with a two-state folding model, we used two cleavage rate constants: k_f for folded RNA and k_u for unfolded RNA. Folding offers protection from cleavage, and therefore $k_f < k_u$. For an RNA that can occupy two states, k_{obs} is a convolution of cleavage contributions based on fractional occupancies and rate constants for each state (Equation 3.4, which is an extension of Equation 3.3 with differential cleavage based on folding):

$$k_{obs} = f_f k_f[Mg^{2+}] + f_u k_u[Mg^{2+}] \quad (3.4)$$

RNA lifetime is the reciprocal of the observed cleavage rate constant (k_{obs}) (Equation 3.5) (170):

$$\boldsymbol{lifetime} = (\boldsymbol{k_{obs}})^{-1} = \left(\frac{\boldsymbol{k_f}[\boldsymbol{Mg^{2+}}]}{\boldsymbol{1} + \left(\frac{\boldsymbol{K_D}}{[\boldsymbol{Mg^{2+}}]}\right)^{\boldsymbol{n}}} + \left[\boldsymbol{1} - \frac{\boldsymbol{1}}{\boldsymbol{1} + \left(\frac{\boldsymbol{K_D}}{[\boldsymbol{Mg^{2+}}]}\right)^{\boldsymbol{n}}} \right] \boldsymbol{k_u}[\boldsymbol{Mg^{2+}}] \right)^{-1} \quad (3.5)$$

Initial folding parameters, K_D = 0.022 mM Mg^{2+} and n = 4.1, for native yeast $tRNA^{Phe}$, were obtained from previous work (79). Initial values of relative rate constants were set to $k_u = 1$ and $k_f = 0.2\ t_{rel}^{-1}[Mg^{2+}]_{rel}^{-1}$, consistent with changes in RNA cleavage rates upon conversion of single strands to duplex (171,172). The software GraphPad Prism 8 was used for simulations.

To model the contribution of folding intermediates to Goldilocks behavior, we modified the two-state model using the approach of Shelton et al. (79) (Appendix Equations B.1, B.2, & B.3). The transition from unfolded to intermediate is described by the terms K_{D1} and n_1, and the transition from intermediate to fully folded is described by K_{D2} and n_2. We initialized the three-state equation with K_{D1} at 1 $[Mg^{2+}]_{rel}$ and k_u/k_f at 5. We set both n_1 and n_2 to 4.1 and K_{D2} for the second transition to 2 $[Mg^{2+}]_{rel}$. k_i was varied.

Our simulations and analysis of experimental data related to RNA Goldilocks phenomena assume that RNA folding is fast relative to cleavage. We assume both that Mg^{2+} binding to RNA is not rate-limiting and that cleavage operates over a fixed folding ensemble. These assumptions are based on experiment and theory. For folding, $k = 10^4$ to 10^{-4} s^{-1} (173-180). For cleavage $k = 10^{-4}$ to 10^{-7} s^{-1} (98,128,156,172). To either cleave or fold RNA, Mg^{2+} must first associate with the RNA. Diffuse association (or diffuse "binding") of Mg^{2+} with RNA has a rate constant of $k \approx 10^{10}$ s^{-1}, near the rate of diffusion

itself (181), whereas specific binding, involving first shell coordination, has $k \approx 10^5\ s^{-1}$ (182,183). Increasing RNA length might attenuate Goldilocks behavior if rate of folding were decreased sufficiently (184) such that folding and cleavage occur on the same timescale.

3.3.2 RNA Preparation

Yeast $tRNA^{Phe}$ was purchased from Sigma-Aldrich (R4018). rU_{20} was a custom oligo purchased from Integrated DNA Technologies. T7-transcribed, stabilized P4-P6 RNA was produced as in Athavale et al. (92). Background Mg^{2+} was removed from the RNAs by dialysis in 180 mM NaCl and 50 mM HEPES buffer pH 7.1 using a 10 kDa MWCO filter.

3.3.3 Circular Dichroism

Extent of folding was quantified by CD spectroscopy. A solution of 10 μM tRNA, 8 μM P4-P6 RNA, or 10 μM rU_{20} in 180 mM NaCl and 50 mM HEPES buffer pH 7.1 was added to a cuvette with a 0.1 cm path length. Spectra were accumulated on a Jasco J-815 spectropolarimeter with scan rate of 200 nm/min, bandwidth of 3 nm, and data pitch of 0.2 nm from 220 to 350 nm at 65°C. The RNAs were titrated with small volumes of concentrated known $MgCl_2$ solutions. CD spectra were blank-subtracted and smoothed with a moving average. For yeast $tRNA^{Phe}$ and P4-P6 RNA, fraction RNA folded was plotted using the theta value at the wavelength that maximized the difference between spectra (260 nm for tRNA and 260.6 nm for P4-P6 RNA). Theta values were baseline-corrected for the effects of dilution, evaporation, and cleavage over the course of CD data acquisition. Yeast $tRNA^{Phe}$ showed little cleavage during CD data acquisition. Some P4-

P6 RNA cleavage was observed, consistent with the longer CD acquisition time and greater RNA length (Figure B.1).

3.3.4 In-line cleavage of RNA

We approximated native ionic strength at 180 mM NaCl, which required elevated temperature (65°C) to observe Mg^{2+}-dependent folding (185). Solutions of 10 μM yeast $tRNA^{Phe}$, 3.8 μM P4-P6 RNA, or 10 μM rU_{20} in 180 mM NaCl, 50 mM HEPES buffer pH 7.1, and variable $MgCl_2$ were incubated at 65°C for 48 hours. Reaction mixtures were separated by electrophoresis on 7% or 6% urea PAGE gels run at 120V for 1 hour and stained with SYBR Green II. Stained gels were digitized with an Azure 6000 or Typhoon FLA 9500 Imaging System. Band intensities were quantified using AzureSpot Analysis software to determine the amount of total intact RNA present.

3.3.5 Sequencing and fragment analysis of P4-P6 RNA cleavage products

RNA species were analyzed by capillary electrophoresis (SeqStudio, Applied Biosystems) by following the manufacturer's protocol and data was analyzed and aligned in MATLAB. In detail, a final concentration of 10 ng/μL uncleaved "fresh" P4-P6 RNA with 0.4 μM of FAM-labeled reverse transcription primer that binds to the 3' end (5'-AGCTTGAACTGCATCCATATCAACA-3', Integrated DNA Technologies), 5 mM DTT, 1X first strand buffer (Invitrogen), 0.5 mM each dNTP, and 2 mM of either ddATP, ddCTP, ddGTP, or ddTTP was reverse transcribed by SuperScript III (Invitrogen) to create fragments for sequencing. The P4-P6 RNA cleavage reactions containing 5 mM, 10 mM, and 15 mM Mg^{2+} were reverse transcribed in parallel with omission of the ddNTPs for identification of cleavage sites. 1 μL of each reverse transcription was

combined with 1 µL GenefloTM 625 size standard ROX ladder (CHIMERx) and 20 µL HiDi (Applied Biosystems). Samples were resolved on a SeqStudio instrument using the FragAnalysis run module.

3.4 Results

3.4.1 Simulations reveal Goldilocks behavior

We investigated RNA Goldilocks behavior for RNAs that fold in response to Mg^{2+}. The simplest model (Figure 3.2) allows two states (folded and unfolded) and two cleavage rate constants; k_u is the cleavage rate constant of an unfolded RNA and k_f is the cleavage rate constant of a folded RNA. The observed rate constant shifts from k_u when the RNA is fully unfolded, to a weighted average of k_u and k_f when the RNA is partially folded, to k_f when the RNA is fully folded. This model allows a Goldilocks peak of chemical lifetime if $k_f < k_u$. From the top of a Goldilocks peak, RNA lifetime decreases if $[Mg^{2+}]$ is either increased or decreased. The folding transition in this model is governed by $[Mg^{2+}]$, K_D (for $[Mg^{2+}]$) and n (the Hill coefficient).

This simple two-state model predicts a Goldilocks landscape of chemical lifetime over a broad range of folding and cleavage parameters (Figure 3.2C-F). K_D modulates the position of the Goldilocks peak on the $[Mg^{2+}]$ axis; RNAs that fold at lower $[Mg^{2+}]$ show a Goldilocks peak at lower $[Mg^{2+}]$. The Hill coefficient n modulates the sharpness of the Goldilocks peak without a substantial change in its position; a larger n gives a sharper peak. k_u modifies the slope of the Goldilocks peak on the low $[Mg^{2+}]$ side, and k_f modifies the slope on the high $[Mg^{2+}]$ side. The ratio of k_u to k_f modulates the intensity of the peak. Goldilocks peaks are absent for RNAs that (i) do not fold, (ii) are always

folded, (iii) do not change cleavage rate constant upon folding, or (iv) transition very gradually between differential cleavage realms with varying [Mg^{2+}] (Figure B.2).

Here we define Goldilocks peak intensity as the ratio of the lifetime at the local maximum to the lifetime at the preceding minimum. In simulation, positions of maxima and minima were determined by determining the simulated lifetime derivative across [Mg^{2+}] and solving for [Mg^{2+}] where slopes are zero. Returning each of those [Mg^{2+}] values back into the original lifetime equation solves for the maximum and minimum used for Goldilocks peak intensity. In experiment, the low and high lifetime datapoints were used directly for the ratio.

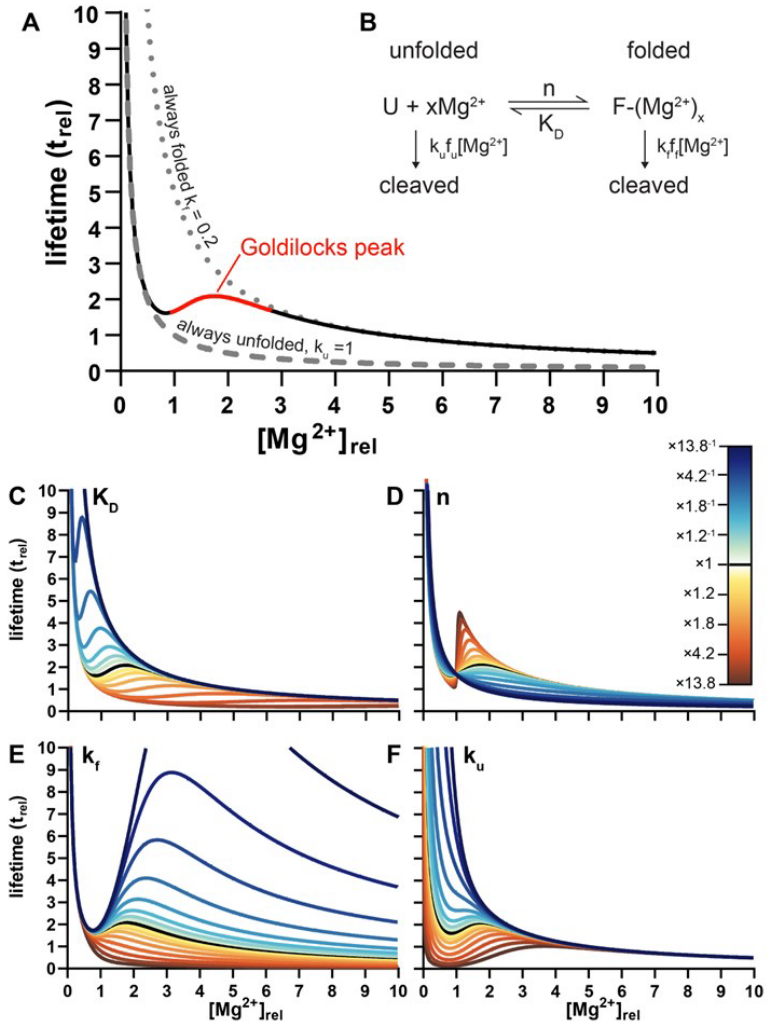

Figure 3.2 – Goldilocks behavior of RNA is predicted by simulations. (A) Simulations reveal the influence of $[Mg^{2+}]$ on the chemical lifetime of an RNA that is cleaved more slowly in the folded state than in the unfolded state (black/red line). The Goldilocks peak is highlighted in red. The lifetime of an always unfolded RNA is shown by a dashed line ($k_u = 1\ t_{rel}^{-1}[Mg^{2+}]_{rel}^{-1}$). The lifetime of an always folded RNA is shown by a dotted line ($k_f = 0.2\ t_{rel}^{-1}[Mg^{2+}]_{rel}^{-1}$). An RNA that shifts between unfolded and folded states shifts between unfolded and folded lifetimes, to establish a Goldilocks peak. Goldilocks behavior requires conversion from unfolded to folded and a slower cleavage constant of folded vs. unfolded RNA ($k_f < k_u$). (B) The two-state reaction mechanism. U is unfolded RNA and F is folded RNA. (C-F) Effects while other parameters are held constant of (C) K_D (D) n (E) k_f, and (F) k_u. Each parameter was varied by multiplication or division by $1+(0.1\times2^i)$ (i = 1, 2, 3, …8). For this representation, $[Mg^{2+}]$ was converted to $[Mg^{2+}]_{rel}$ where $1\ [Mg^{2+}]_{rel} = K_D = 0.022$ mM Mg^{2+}. Lifetime (t) was converted to t_{rel} where $t_{rel} = 1$ when $[Mg^{2+}]_{rel} = 1$ and the cleavage constant(s) are always $1\ t_{rel}^{-1}[Mg^{2+}]_{rel}^{-1}$. Figure from Ref. (149).

3.4.2 Goldilocks behavior in complex models

More realistic RNA folding mechanisms involve intermediate states (79). In a model with intermediates, each intermediate I is associated with specific cleavage rate constant k_i (Figure 3.3A). The simulations reveal that the number, intensities, and proximities of Goldilocks peaks depend on the relative magnitudes of the rate constants and on locations of the folding transitions in $[Mg^{2+}]$-space. For a three-state model with two transitions that are fully resolved in $[Mg^{2+}]$-space, RNA can display two distinct Goldilocks peaks (Figure 3.3B). When the transitions overlap in $[Mg^{2+}]$-space, decreasing k_i tends to increase the intensity of the Goldilocks peak at the $[Mg^{2+}]$ where the intermediate population is maximum. Increasing k_i depresses lifetime at low $[Mg^{2+}]$ (peak position 1, Figure 3.3B) and shifts the Goldilocks peak to higher $[Mg^{2+}]$ (peak position 2, Figure 3.3B). An RNA with a folding intermediate that is cleaved more slowly than the fully folded state ($k_i < k_f$) or cleaved more rapidly than the unfolded state ($k_i > k_u$) it can display especially intense Goldilocks peaks. If an intermediate state has intermediate protection, the net Goldilocks peak is less intense than in the absence of an intermediate.

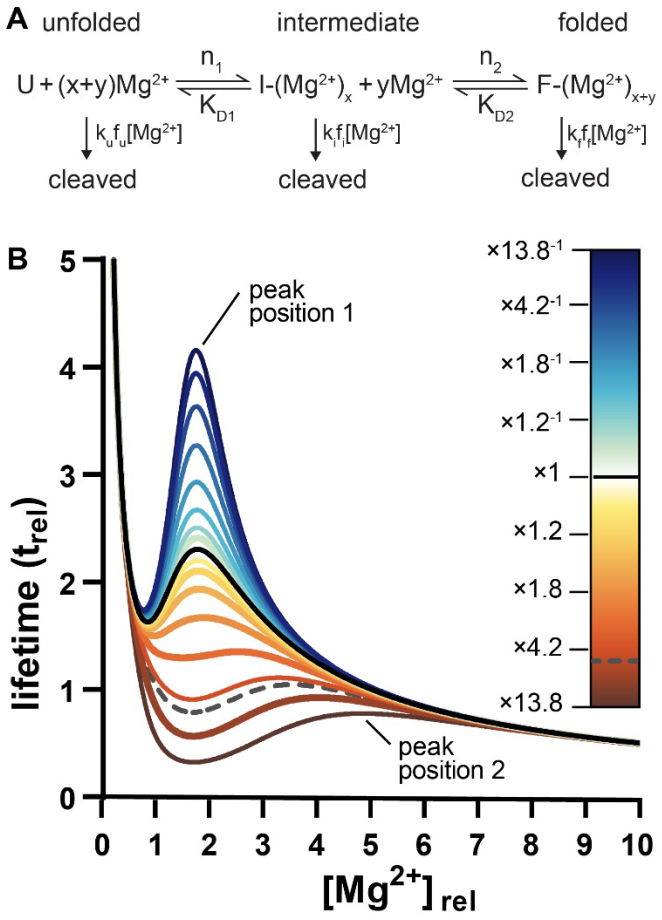

Figure 3.3 – Complex folding models form Goldilocks peaks. (A) In a three-state mechanism, unfolded RNA converts by a first transition to an intermediate and by a second transition to fully folded. Unfolded RNA is cleaved with a rate constant k_u, the intermediate is cleaved with a rate constant k_i, and fully folded RNA is cleaved with a rate constant of k_f. (B) In the simulation, k_i was varied relative to k_u while other parameters were fixed. The black line represents lifetimes when $k_i = k_f$. The dashed line represents the lifetimes when $k_i = k_u$. A $k_i < k_f$ scenario favors an early Goldilocks peak and a $k_i > k_u$ scenario favors a late Goldilocks peak. Figure from Ref. (149).

3.4.3 Goldilocks intensity

We show that RNA can inhabit a Goldilocks peak of RNA protection flanked by conditions of lability. The level of protection, given by Goldilocks peak intensity, depends on RNA properties. We defined Goldilocks peak intensity as the ratio of the

peak maximum to minimum, i.e. the ratio of the protected lifetime to the labile lifetime. Using Goldilocks peak intensity, one can compare and rank various RNAs. We observed, in two-state simulations, that Goldilocks peak intensity increases with increased cooperativity of folding (n) or with increased extent of protection afforded by folding (decrease of k_f relative to k_u) (Figure 3.4A). We surveyed values of n and k_u/k_f to create a Goldilocks intensity map (Figure 3.4B). A $k_u/k_f = 3$ with an n=4 produces a modest Goldilocks peak. Increasing either n or k_u/k_f increases Goldilocks peak intensity. Lowering parameters n or k_u/k_f disallows a Goldilocks peak unless there is a compensatory increase in the other parameter. We considered area under the curve as a method for quantifying the Goldilocks phenomena. By this method, greater area under the curve would correspond to more extensive protection. Intensity and area together describe the shape of a Goldilocks peak. While intensity indicates the protection an RNA achieves when reaching its peak, area can be concentrated locally or widely dissipated (Figure B.3). We conclude that a local description (intensity) is a more useful comparator.

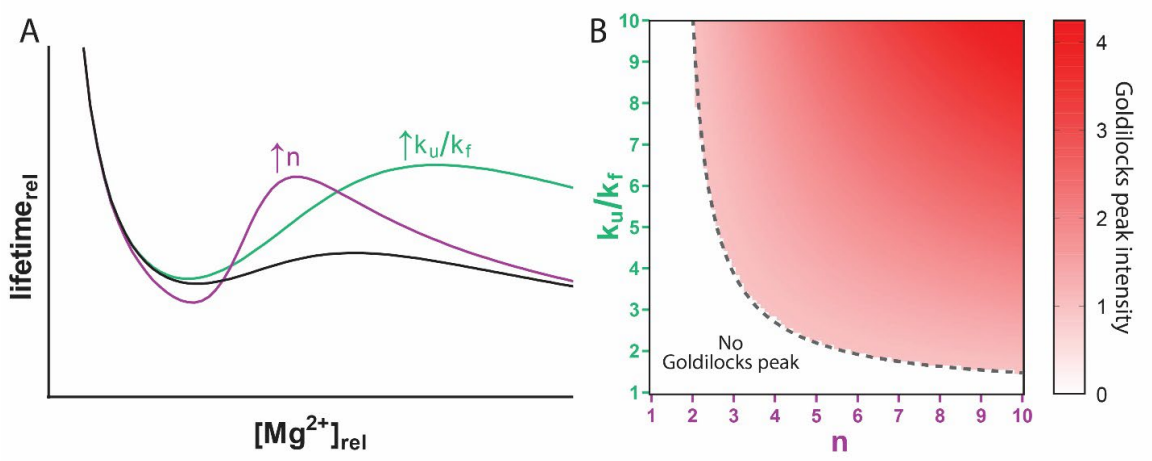

Figure 3.4 – Goldilocks peak intensity increases with n and k_u/k_f ratio. (A) A simulated Goldilocks peak (black) is enhanced by increasing the RNA's cooperativity (n) or increasing the ratio of the unfolded to the folded cleavage rate constant (i.e. increasing protection of the folded state). (B) Surveying a range of rate constant ratios (k_u/k_f) across a range of n values shows that regions toward high k_u/k_f, n, or both have Goldilocks peaks and regions where both parameters are low do not. Figure from Ref. (149).

3.4.4 Experimental observation of a Goldilocks landscape of tRNA

To experimentally investigate Goldilocks behavior, we assayed both fraction folded and lifetime of yeast $tRNA^{Phe}$ across a range of [Mg^{2+}]. Circular Dichroism showed a clear cooperative folding transition with a [Mg^{2+}] midpoint between 1 and 2 mM (Figure 3.5; Figure B.4). Random coil yeast $tRNA^{Phe}$ folds to the native L-shaped structure upon addition of Mg^{2+} (173,186-191). Chemical lifetime of yeast $tRNA^{Phe}$ showed a distinct Goldilocks peak near 3 mM Mg^{2+}, where the tRNA was ~95% folded (Figure 3.5; Figure B.5). The tRNA lifetime was longer at 3 mM Mg^{2+} than at either 2.0 mM or at 3.5 mM Mg^{2+}. In contrast, rU_{20}, which does not fold, did not exhibit Goldilocks behavior (Figure B.6).

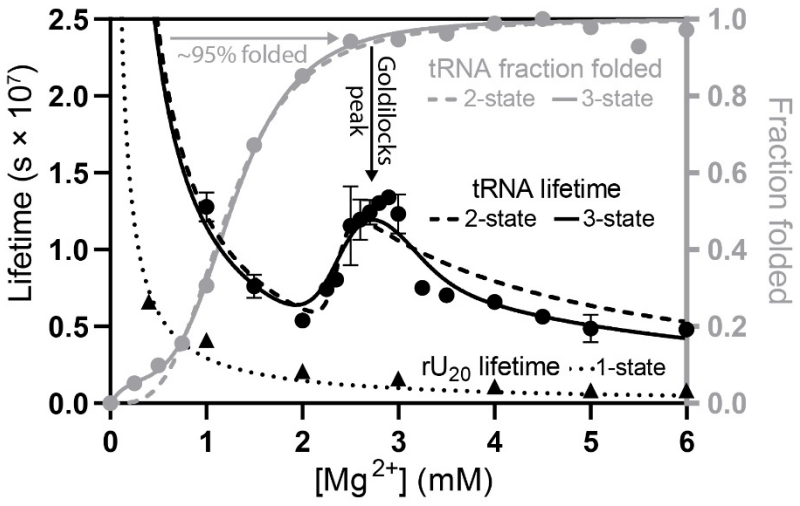

Figure 3.5 – Yeast tRNA^{Phe} shows Goldilocks behavior. Lifetimes of yeast tRNA^{Phe} (black circles) and rU$_{20}$ (black triangles) were determined over a range of [Mg^{2+}]. The yeast tRNA^{Phe} fraction folded (gray circles) was determined by CD. Experimental lifetimes were fit to two-state (black dashed) and three-state (black solid) models. Fraction folded was fit with two-state (gray dashed) and three-state (grey solid) Hill equation models. The three-state model better approximates the lifetime data, with a more intense Goldilocks peak than the two-state model. The tRNA Goldilocks peak is coincident with folding. rU$_{20}$ lifetimes decrease monotonically with no Goldilocks peak (dotted black). rU$_{20}$ did not show a folding transition (Figure B.6). Lifetimes were determined by quantification of intact RNA resolved by PAGE after 48 hours and normalized per phosphodiester bond. All experiments were conducted in 180 mM NaCl, 50 mM HEPES pH 7.1 at 65°C, with variable [Mg^{2+}]. Yeast tRNA^{Phe} lifetime error bars represent the standard deviation of five replicates. Folding and rU$_{20}$ lifetime experiments used one replicate. Figure from Ref. (149).

We compared the experimental lifetime data with predictions of our models (Figure 3.5). The observed yeast tRNA^{Phe} Goldilocks landscape is reasonably fit by a two-state model. The fit and observed Goldilocks peaks are centered at the same [Mg^{2+}]. The cleavage rate constant of the unfolded tRNA is predicted to be 2.7 times greater than that of the folded tRNA. However, the observed Goldilocks peak is sharper and more intense than predicted by the two-state model. A three-state model provides a better fit to the data, especially in the center of the Goldilocks peak. In the three-state model the

cleavage rate constant for the unfolded RNA is predicted to be 3.2 times that of the intermediate and 2.2 times that of the fully folded tRNA ($k_u > k_f > k_i$). The statistical significance of the improved fit of the three-state versus the two-state lifetime and folding models is indicated by residual errors (Figure B.7). Our results are consistent with previous observations of >2 states for folding of yeast $tRNA^{Phe}$ (79,173,186,192). The fundamental conclusion here, which is the prediction and validation of Goldilocks behavior by RNA, is not dependent on the folding model.

Yeast $tRNA^{Phe}$, with an intense Goldilocks peak, appears to fold via a protected intermediate. Prior work has shown that yeast $tRNA^{Phe}$ is most compact in intermediate ionic strength (193-195) suggesting that the folding intermediate is more compact that the native state (however, see reference (196)).

3.4.5 Experimental observation of a Goldilocks landscape of Tetrahymena ribozyme P4-P6 domain

P4-P6 RNA is a well-established model (165,166) that folds with increasing Mg^{2+} (197,198). The Mg^{2+}-dependence of P4-P6 RNA folding by CD (Figure B.8) and chemical lifetime (Figure B.9) were determined (Figure 3.6) by the same methods and under the same conditions as for yeast $tRNA^{Phe}$. P4-P6 RNA has a clear Goldilocks peak that is coincident with RNA folding.

The Goldilocks behavior of P4-P6 RNA is approximated by both the two-state or three-state models. Both models recreate the position in Mg^{2+}-space and intensity of the single Goldilocks peak. The peak is produced by the intermediate to folded transition in the three-state model wherein k_i is 8 times k_f. When constrained to two states, k_u is 22

times k_f. A low [Mg^{2+}] folding transition prior to the transition that forms the Goldilocks peak is approximated by the three-state model. The low [Mg^{2+}] trend is captured only by the three-state model. The fit suggests that P4-P6 RNA folds by least three states, even though only two contribute to the Goldilocks peak. This conclusion is supported by residual plots for both lifetime and folding (Figure B.10) and previous observations that P4-P6 RNA has more than two folding states (197,198).

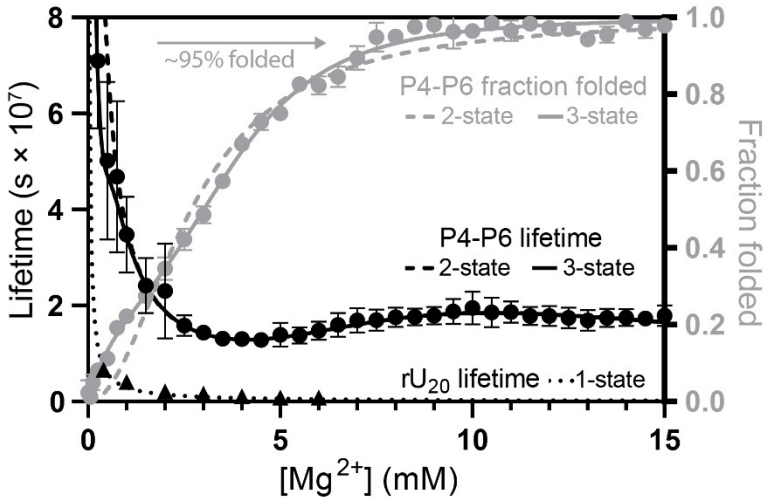

Figure 3.6 – P4-P6 RNA shows Goldilocks behavior. P4-P6 RNA lifetime (black circles) shows a Goldilocks peak when the RNA is near-fully folded. The two-state (dashed line) and three-state (solid line) fits equally capture lifetime within the Goldilocks peak but the three-state fit better approximates lifetime at low [Mg^{2+}]. Lifetime is normalized per phosphodiester bond. For a non-folding RNA comparison, rU_{20} lifetime (black triangles) is included and fit with a single state model (dotted line). P4-P6 RNA folding measured by CD (gray circles) is better approximated by a three-state fit (solid gray line) than a two-state fit (dashed gray line). Both folding and lifetime experiments were conducted in 180 mM NaCl, 50 mM HEPES pH 7.1 at 65°C with variable $MgCl_2$. Error bars represent the standard deviations. P4-P6 RNA lifetime had four replicates, P4-P6 RNA folding had two replicates, and rU_{20} lifetime had one replicate. Figure from Ref. (149).

3.4.6 Comparison of yeast $tRNA^{Phe}$ and P4-P6 RNA

Both RNAs display Goldilocks peaks in experiment and in simulation. Both RNAs are best fit to models with more than two states. For the tRNA the Goldilocks peak is sharp, with a half-height peak width of around 1 mM Mg^{2+}. This level of cooperativity is associated with a pronounced Goldilocks peak. tRNA is noted for its high level of structure (199,200). Conversely, P4-P6 RNA has low cooperativity, which is associated with a broad Goldilocks peak, with a peak width at half-height of around 5 mM Mg^{2+}. Goldilocks peak intensity for tRNA is greater (2.4) than for P4-P6 RNA (1.5). The fit parameters of each RNA are compared in Table 3.1.

Table 3.1 – Fitted parameters for yeast $tRNA^{Phe}$ and P4-P6 RNA

RNA	Exp.[a]	States	k_u ($s^{-1}M^{-1}$)[b]	k_i ($s^{-1}M^{-1}$)[b]	k_f ($s^{-1}M^{-1}$)[b]	K_{D1} (mM)	K_{D2} (mM)	n_1	n_2
tRNA	lifetime	3	8.7×10^{-5}	2.7×10^{-5}	3.9×10^{-5}	2.2	3.3	15[c]	15[c]
	lifetime	2	8.2×10^{-5}	--	3.1×10^{-5}	2.3	--	33.5	--
	folding	3	--	--	--	0.2	1.3	1.1	3.8
	folding	2	--	--	--	--	1.2	--	3.4
P4-P6	lifetime	3	6.1×10^{-4}	2.8×10^{-5}	3.5×10^{-6}	0.5	4.9	3.9	3.4
	lifetime	2	8.7×10^{-5}	--	3.9×10^{-6}	--	4.8	--	3.4
	folding	3	--	--	--	2.3	3.8	0.9[d]	2.9
	folding	2	--	--	--	--	2.7	--	2.0

[a]Experiment type, either lifetime analysis by fraction intact in PAGE or folding analysis by CD.
[b]Cleavage rates are per phosphodiester bond
[c]Values were poorly constrained, the value shown is one that minimizes magnitude while following the data
[d]n values less than one have literature precedent (201)

3.4.7 Site specificity of cleavage

To characterize Goldilocks phenomena at the level of single nucleotides, we quantified cleavage fragments of P4-P6 RNA using a sequencer. We examined the site-specific extent of cleavage under conditions of the Goldilocks peak (10 mM Mg^{2+}), on the partially folded side of the peak (5 mM), and on the fully folded side of the peak (15

mM) (Figure B.11). The average extent of cleavage is less under the conditions of the Goldilocks peak (0.18) than in regions flanking the peak (0.21 pre-peak and 0.20 post-peak**)**. Subtracting the 10 mM Mg^{2+} Goldilocks peak condition as a baseline shows nucleotides that experience more cleavage off the peak than on the peak, with larger Δcleavage values indicating greater cleavage (Figure 3.7A). This information was superimposed on P4-P6 RNA's secondary structure (Figure 3.7B). The number of detectable cleavage sites and variety of cleavage intensities are greatest for the partially folded RNA (at 5 mM Mg^{2+}). These sites overwhelm the few nucleotides that are highly cleaved in the folded state (strong negative Δcleavage). In the partially folded realm, double-stranded RNA shows more uniform extent of cleavage than unpaired RNA (202). Variability decreases when the RNA fully folds, where the conformations of essentially all nucleotides become fixed. Here, Δcleavage for 5 mM to 10 mM Mg^{2+} is most variable, especially in bulge and loop-forming regions. When increasing from 10 mM to 15 mM Mg^{2+} a few cleavage hot spots emerge in unpaired regions, where the RNA is most susceptible to cleavage (114).

In P4-P6 RNA, the Mg^{2+}-binding core does not appear to be folded at 5 mM Mg^{2+}, as indicated by extent of cleavage (Figure 3.7A-B). The metal core folds and is protected at 10 mM Mg^{2+}. This region is a representation of the double-edged sword of Mg^{2+}; by associating with Mg^{2+} the RNA is protected from Mg^{2+}. As expected (203), by its low reactivity relative to other loop or bulge regions, the GAAA tetraloop appears to be fully folded by 5 mM Mg^{2+}.

The sequencing data indicate that even though the low resolution P4-P6 RNA PAGE banding patterns remain reasonably constant, relative extent of cleavage at various

sites does in fact change. Although the yeast $tRNA^{Phe}$ banding pattern appeared uniform across [Mg^{2+}] in gels, we assume significant differences in locations of cleavage upon folding. Site-specific analysis of yeast $tRNA^{Phe}$ was not possible with our method because of the RNA base modifications.

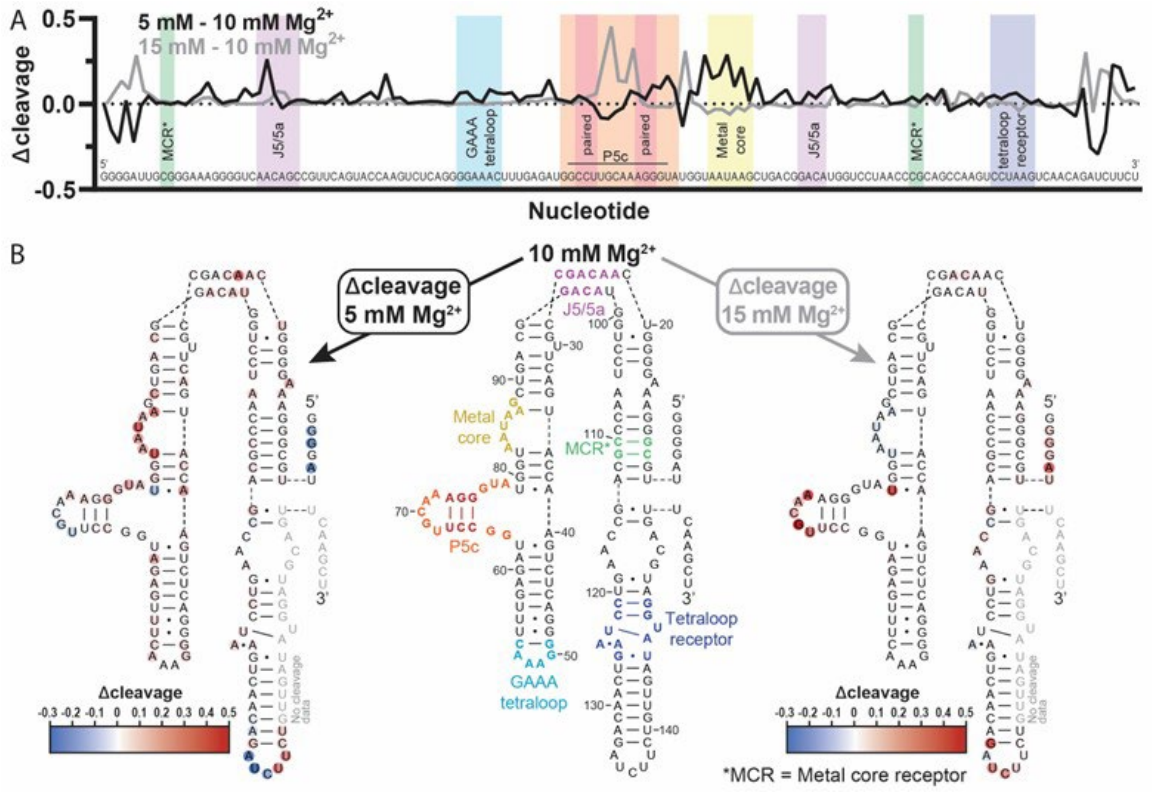

Figure 3.7 – Differences in site specificity of cleavage with changing [Mg^{2+}]. (A) Δcleavage reports differences in cleavage between P4-P6 RNA at the Goldilocks peak (10 mM Mg^{2+}) and at 5 or 15 mM Mg^{2+}. Δcleavage indicates highest lifetime at the Goldilocks peak. (B) Superimposition of cleavage data onto the secondary structure of P4-P6 RNA shows that hot spots for cleavage (red) or protection (blue) relative to P4-P6 RNA at 10 mM Mg^{2+} occur at loops and bulges in the RNA. Important structural features are provided as in Bisaria 2016 (204). Each Δcleavage value is the mean of two replicates. Figure from Ref. (149).

3.5 Discussion

By simulation and experiment we validated a Goldilocks model of RNA. Local

maxima in lifetime are flanked by conditions of greater lability. RNAs can resist Mg^{2+}-mediated cleavage when Mg^{2+} folds the RNA. Increasing [Mg^{2+}] beyond the folding threshold increases Mg^{2+}-mediated cleavage. We use Goldilocks model framework to explain how lifetime landscapes are modulated by specific characteristics of diverse RNAs. We predict that Goldilocks landscapes are modulated by monovalent cation concentrations, type of divalent cation, RNA sequence and modification, protein and ligand association, and temperature. RNA that cannot fold or unfold cannot access Goldilocks protection. Self-cleaving ribozymes are exempt from Goldilocks behavior because their folding increases rates of cleavage.

3.5.1 Goldilocks landscapes

RNA response to [Mg^{2+}] is modulated by RNA sequence and chemical modification. The number, intensity, profile, and position in [Mg^{2+}]-space of Goldilocks peaks depends on RNA sequence and chemical modification. The position of a Goldilocks peak in [Mg^{2+}]-space is determined primarily by the affinity of the folded RNA for Mg^{2+}. A smaller K_D shifts the Goldilocks peak to lower [Mg^{2+}].

Goldilocks behaviors of RNA should extend beyond Mg^{2+} to species such as Fe^{2+}, which also promote both RNA folding and cleavage (92,94). Even farther, the general principles of Goldilocks behavior can be applied to any agent that has differential opposing effects on lifetime. For example, protein is cleaved by hydrolysis (205). Protein folding decreases rates of hydrolysis (150) and is often promoted by high water activity (206). This model predicts water-defined Goldilocks phenomena for proteins.

3.5.2 Goldilocks behavior in vivo

RNA Our simulations anticipate some RNAs *in vivo* may inhabit Goldilocks peaks. Free Mg^{2+} *in vivo* is near 1 mM (207,208). An RNA hairpin ribozyme used as a model is mostly folded at 1 mM Mg^{2+} in molecularly crowded conditions mimicking the cytosol (209). If the minimal [Mg^{2+}] required for folding *in vivo* coincides with the *in vivo* [Mg^{2+}], RNA may occupy a Goldilocks peak in cells. More specific *in vivo* conclusions remain unresolved thus far because of differences in *in vitro* and *in vivo* conditions and limitations in manipulating *in vivo* [Mg^{2+}] (210). Goldilocks landscapes remain to be evaluated *in vivo* and in the context of protein and ligand binding. For mRNAs, with lifetimes *in vivo* of minutes (211-215), spontaneous cleavage might be insignificant. However, long-lived RNAs (tRNAs, ~9 hours to days (216-219); and rRNAs, ~5 hours to days (220-224)) might be subject to spontaneous cleavage, governed by the Goldilocks phenomena. Goldilocks behavior could explain in part why cells invest in careful maintenance of Mg^{2+} homeostasis (225). It seems likely that a narrow range of [Mg^{2+}] prolongs specific RNA lifetimes *in vivo*.

3.5.3 Goldilocks and Origins of Life

RNA can transit between dangerous spaces and safe spaces. Finely controlled metastability, with access to Goldilocks peaks of protection, is most likely an imprint of evolutionary processes (226) during the emergence of RNA on the ancient Earth. Sophisticated internal control of lifetime is an indication of selection - of backbone structure, base modifications, and sequence, all of which modulate Goldilocks landscapes.

CHAPTER 4. CONCLUSION AND OUTLOOK

4.1 Import on the origin of life

4.1.1 Fe^{2+} could have driven rapid RNA evolution

We find that Fe^{2+} was an important and more potent cleavage catalyst than Mg^{2+} for RNA on early Earth. Initially, fast RNA cleavage with Fe^{2+} relative to Mg^{2+} seems a detriment to the emergence of RNA in an early environment with more abundant Fe^{2+}. However, such a stance assumes the current Mg^{2+}-based rate of other biological processes including RNA synthesis. Overall rates of biochemistry may have been altered in an Fe^{2+} world. If RNA polymerization rates matched RNA cleavage rates in the presence of Fe^{2+}, then a population of RNA could be maintained. In fact, some RNA polymerases show higher RNA production using Fe^{2+} in place of Mg^{2+} under certain test conditions (95,227,228). Supporting rationale is that catalysts, in this case Fe^{2+} or Mg^{2+}, lower activation energy for reactions to more readily proceed forward and in reverse (229). Enhanced cleavage with Fe^{2+} relative to Mg^{2+} should be paralleled in the reverse reaction, enhanced polymerization, allowing RNA to persist.

Rapid rates of RNA turnover through Fe^{2+}-driven cleavage and polymerization would have impacted the rate of evolution on early Earth. In an Fe^{2+} environment, new RNAs can enter and exit the population quickly, allowing sequence space to be explored in little time (Figure 4.1). The result is that evolution proceeds quickly, and more diversity can exist in Fe^{2+}-evolved than Mg^{2+}-evolved RNA. More sequence diversity and

fast evolution with Fe^{2+} may have helped RNA persist across changing environmental conditions over billions of years.

Figure 4.1 – RNA's explorable sequence space is greater under Fe^{2+} than Mg^{2+}. Each bar represents an RNA sequence (black), which is replaced by the end of its lifetime with the next RNA going forward in time. In this representation, a mutation (red) emerges once per replication, or lifetime. The example RNA lifetime is half as long with Fe^{2+} as Mg^{2+}. Given the same amount of time, an RNA population will have explored more sequence space under Fe^{2+} evolution than under Mg^{2+} evolution because mutations accumulate with more generations.

4.1.2 Goldilocks peaks are signs of selection

Origin of life theory posits that there has been continuous selection driving chemical and gradually Darwinian evolution of a persistent system across Earth's history (4). Therefore, one explanation for why life has its current set of biomolecules is because those are the molecules that survived and survive selection and not because they are optimal or special in any other way. It should then be possible to find fingerprints of selection on biomolecules such as RNA that are emblematic of their selection history and can help us reconstruct the past. Goldilocks peaks appear to be one such fingerprint.

As a sign of selection, we would expect a biopolymer to have a trait or combined traits that only support its survival within a flexible window of boundaries. The importance of the window of boundaries is that the biomolecule neither becomes unchangeable nor fleeting, and flexibility in the window allows adaptability of the trait as environmental conditions change. RNA Goldilocks peaks fit this criterion in the single trait of a limited but variable lifetime optimum across metal conditions. Other competitors to RNA during its selection without such a property may have been winnowed out. Therefore, the modern existence of RNA is likely due to ancient selection on a chemical level.

4.1.3 Goldilocks peaks may help reconstruct the M^{2+} environment at the cradle of life

We demonstrated that folded RNAs of different structures and classes have distinct Goldilocks peaks. Two RNAs only give a preview of the Goldilocks peak landscape across RNAs and M^{2+}, let alone different conditions of temperature, ligand binding, etc. Thus far, low mM Mg^{2+} appears important for RNA lifetime under our conditions, but testing more RNAs will show whether this range is conserved, and perhaps can be extended back to early Earth. If so, low mM Mg^{2+} might have been important for the emergence of RNA. Similarly, testing other M^{2+} will allow prediction of which M^{2+} might have enriched RNA evolution through Goldilocks peaks. M^{2+} with the dualism of both folding and cleaving RNA may produce Goldilocks peaks. Therefore, our work suggests that Fe^{2+} will produce RNA Goldilocks peaks. Possibly, a mixture of M^{2+} supported RNA evolution.

Goldilocks peak insight on ancient M^{2+} conditions is a rare and significant window onto the bio-geochemical environment of the cradle of life. Contextual geological records are limited by the age of preserved rocks themselves, which are thought to extend back 3.8 billion (230,231) to possibly 4 billion years (232). However, there was surface water to support life on Earth estimated about 4.4 billion years ago (233,234), leaving a significant gap in the historical record. Additionally, in the oldest rocks, there is great contention to claims that they were altered by life (2,235). Biomolecules only are preserved in rocks up to hundreds of millions of years (236), and rocks are regularly metamorphosed and their original compositions are modified or overwritten. However, Goldilocks peaks that persisted across time may preserve an environmental record as old as RNA itself.

Knowledge of the ancient metal environment is helpful in two areas of astrobiology. In prebiotic chemistry, it can inform what metal conditions are appropriate to use in experiments simulating the early biotic or prebiotic environment, which might lead to more provocative and meaningful outcomes. In the search for life, defined metal conditions might help target the search for habitable environments elsewhere, for example, on Mars.

4.2 Import on modern biology

4.2.1 In-line cleavage might dominate Fe^{2+}-driven RNA cleavage in anoxic cells

Our work shows that Fe^{2+} is readily used in critical biomolecules like the ribosome but is a double-edged sword because it also rapidly cleaves RNA by in-line cleavage in anoxia. In oxic conditions, though, Fe^{2+} in-line cleavage of RNA is

overshadowed by Fe^{2+} and O_2-driven Fenton chemistry. In our experiments, 1 mM Fe^{2+} completely cut all rRNA before 15 minutes by Fenton reactions and by ~4 hours by in-line cleavage, although under different conditions. Cleavage of RNA by Fenton chemistry in just 30 seconds is detectable by gel electrophoresis (237). Therefore, Fe^{2+} is not evolutionarily favorable in high doses in oxic post-GOE systems but might balance the double-edged sword in life unexposed to oxygen or in the pre-GOE world. In fact, there is a high usage of iron by organisms in oceanic oxygen minimum zones measured by genes and transcripts for iron-binding proteins (238). Fe^{2+} use in RNA balanced with RNA in-line cleavage may have carried on from life's anoxic origins into organisms that retain their anoxic lineage in Earth's oceans today. Other anoxic life possibly balancing Fe^{2+} in-line cleavage is in the gut, which contains bacteria evolved as strict anaerobes (239).

4.2.2 Fe^{2+} in-line cleavage may contribute to iron toxicity

Our work suggests a new pathway for iron toxicity through Fe^{2+}-driven in-line cleavage. Free Fe^{2+} can reach up to 20 μM in diseased states (240). This load of iron causes oxidative reactions through Fenton chemistry as the main mechanism of cell damage (241). In the example of Alzheimer's Disease, rRNA will take up additional Fe^{2+} then is oxidatively damaged by that Fe^{2+}, inhibiting its ability to translate (146). This suggests that rRNA is also exposed to low levels of Fe^{2+}-mediated in-line cleavage at the same locations and affecting its translation whenever excess Fe^{2+} is present, not just in oxic conditions. The low level of in-line cleavage is likely still important. If the rate of Fe^{2+}-driven in-line cleavage is similar *in vivo* to our experiments, then a 1,000 nucleotide-long RNA exposed to 20 μM Fe^{2+} would have a lifetime of just seven hours.

A normal lifetime for human rRNA is one or more days (221,223). tRNAs also have long lifetimes and could be cut prematurely by in-line cleavage with excess Fe^{2+}. Fe^{2+}-driven in-line cleavage of RNA is an added reason why cells might carefully maintain their iron stores.

4.2.3 Goldilocks peaks in vivo

Our experiments support the conclusion that Goldilocks peaks modulate the survival of RNA in non-cellular conditions. However, it remains untested whether RNAs are subject to Goldilocks peaks in cells. The primary challenge to *in vivo* experiments is manipulating the cellular [M^{2+}]. Cells will likely die quickly when lowering [M^{2+}] to the point of RNA unfolding, which is required to define a Goldilocks peak. It will also be difficult to separate the lifetime effects of M^{2+}-driven cleavage and folding from other influences that changing M^{2+} has across the cell, particularly for Mg^{2+} as life's most used M^{2+}. If these challenges can be overcome, then *in vivo* Goldilocks peak studies can address questions including:

1. Do Goldilocks peaks exist *in vivo*?
2. Where does physiological [M^{2+}] fall relative to *in vivo* RNA Goldilocks peaks?
3. How does lifetime driven by Goldilocks peaks compare to other drivers of programmed RNA turnover (e.g. RNases)?
4. How do native interactions with proteins and other cell components affect Goldilocks peaks?
5. Does forcing RNAs out of their Goldilocks peaks contribute to M^{2+} toxicity?

6. Might cells have adopted their [M^{2+}] to keep their RNAs within their innate Goldilocks peaks?
7. How do Goldilocks peaks compare between organisms with different [M^{2+}] requirements?

Simulating the *in vivo* environment may more readily answer some but not all these remaining questions. Experiments could be performed in cell lysate or in the presence of molecular crowders, allowing control of [M^{2+}] while maintaining cell-like conditions. Overall, there is great potential for discovery of Goldilocks influences on cells.

4.3 Future outlook

4.3.1 Does Fe^{2+} support non-enzymatic RNA polymerization?

Our results suggest that the reverse reaction of non-enzymatic in-line cleavage, i.e. non-enzymatic RNA polymerization, should also be accelerated with Fe^{2+}. Polymerization can be favored by beginning with all unpolymerized RNA monomers so the reaction can only go in the polymerization direction. In one study, non-enzymatic RNA polymerization has been shown with Fe^{2+} and is more effective than with Mg^{2+} (242). However, this reaction used a 5' activated nucleotide as the starting monomer, which polymerizes through a different route than reversed in-line cleavage. To test the reverse of the in-line cleavage reaction, the starting monomer would instead have a 2',3'-cyclic phosphate. Simple incubation of the cyclic phosphate monomers in a buffer containing Fe^{2+} with or without a template strand may reveal a new mechanism of RNA polymerization with Fe^{2+}. Wet-dry cycling could be incorporated to incrementally grow

longer, farther-from-equilibrium RNA (243). The polymerization reaction could also be attempted in the presence of amino acids or peptides, shown to enhance other RNA polymerization experiments (244,245). Fe^{2+} RNA polymerization reactions will answer whether Fe^{2+} possibly supported rapid RNA turnover and evolution on early Earth.

4.3.2 What are the bounds of Goldilocks peaks across M^{2+}, RNAs, and time?

There still are many questions surrounding Goldilocks peaks that can be answered readily *in vitro*. Three main questions are whether (i) prebiotically important M^{2+} like Fe^{2+} and Mn^{2+} or M^{2+} mixtures produce Goldilocks peaks, (ii) RNAs of different classes have characteristic Goldilocks peaks that factor into their different lifetimes, and (iii) ancient RNAs have a Goldilocks peak range that is a footprint of the M^{2+} environment of RNA origins. Ideally to address these questions, many RNAs could be tested at once to greatly expand the surveyable space. There is no current limitation directly on how many different RNAs can be cleaved at once, as RNAs of entire organisms could undergo cleavage simultaneously in a single tube. However, analyzing the fraction of each type of RNA that becomes cleaved would be impossible to resolve on a gel in a mixture of RNAs plus their cleavage products without some intervention. There are at least two methods to help distinguish between RNAs in a messy, cleaved mixture so that the boundaries of RNA Goldilocks peaks across M^{2+}, sequence, and time can be explored.

One method to increase experimental throughput is to modify the RNAs so only intact, uncleaved RNAs are detectable, then to measure their presence across $[M^{2+}]$. This method requires relatively few preparatory steps to assess the cleavage products, is affordable, and could be done in little time. The process would involve adding

fluorescent and biotin tags to opposite ends of the RNAs then to proceed with cleavage by M^{2+}. If an RNA is cleaved, it produces two smaller RNAs, one attached to biotin, and the other attached to the fluorophore. Streptavidin can then separate for analysis any RNAs, cleaved or uncleaved, still attached to biotin. RNAs that were uncleaved will still have their fluorophore attached and be fluorescently detectable, while cleaved RNAs will be missing the fluorophore and escape detection. The amounts of remaining intact RNAs could be fluorescently detected by gel or capillary electrophoresis. Thereby, many RNAs can be examined in parallel, and their Goldilocks peaks found across M^{2+} identity and concentration.

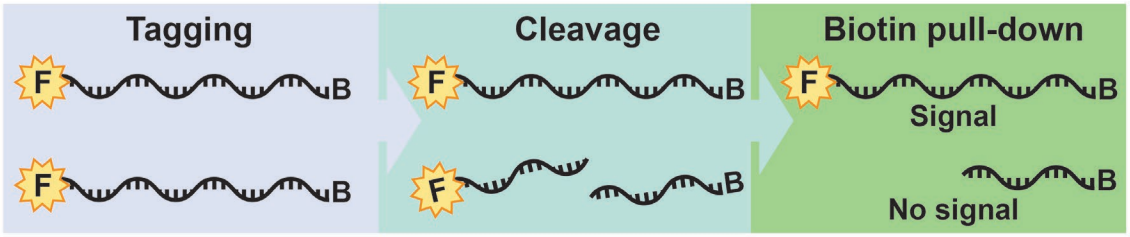

Figure 4.2 – A mixture of RNAs can be cleaved for simultaneous Goldilocks peak analysis using tags. F is for the fluorophore tag and B is for the biotin tag.

A second method for increased throughput of RNA cleavage analysis is by using RNA-seq. RNA-seq is a high-throughput method that measures both the quantity and sequence of different RNAs in a mixture. With RNA-seq, it would be possible to not only determine the lifetimes of RNAs across $[M^{2+}]$, but also sequence the cleavage fragments to map where cleavage occurs. There are many examples of using RNA-seq to detect RNAs and RNA cleavage products from entire transcriptomes (246-250). RNA-seq has the advantage of being data-rich, but it is also expensive, slow, and has an intensive data analysis process. RNA-seq would be a beneficial supplement to the biotin and

fluorophore tagging method through which appropriate experimental conditions can be found. Through this and related experiments, many more answers will be revealed about RNA and metals and their intersection near the origin of life.

APPENDIX A. SUPPLEMENTAL INFORMATION FOR CHAPTER 2

Table A.1 – Proteins differentially expressed in ribosomes purified from aerobic vs anaerobic cells. Information on metal cofactors was taken from the UniProt entries for each protein

Condition	Protein more abundant in	Protein name	UniProt ID	Fold more abundant	p-value	Metal cofactor
1 mM added Fe^{2+}	Anaerobic vs. Aerobic	L-threonine dehydratase catabolic TdcB	P0AGF6	211.8	0.02	N.A.
		Hydrogenase maturation factor HypB	P0AAN3	12.1	0.03	N.A.
		Glycerol dehydrogenase	P0A9S5	11.4	0.01	Zn^{2+}
		Phosphoribosylaminoimidazole-succinocarboxamide synthase	P0A7D7	6.0	0.02	N.A.
		Aldehyde-alcohol dehydrogenase	P0A9Q7	6.0	0.03	Fe^{2+}
		Uncharacterized protein YjjI	P37342	5.8	0.02	N.A.
		Probable acrylyl-CoA reductase AcuI	P26646	5.5	0.01	N.A.
		Bacterial non-heme ferritin[a]	P0A998	5.1	0.03	N.A.
		Aspartate ammonia-lyase	P0AC38	4.1	0.01	N.A.
		Fumarate reductase flavoprotein subunit	P00363	3.7	0.05	N.A.
		UvrABC system protein B	P0A8F8	3.6	0.01	N.A.
		Formate acetyltransferase 1	P09373	3.2	0.01	N.A.
		UPF0227 protein YcfP	P0A8E1	3.1	0.02	N.A.
		Phosphoenolpyruvate-protein phosphotransferase	P08839	2.6	0.03	Mg^{2+}
		Ubiquinone/menaquinone biosynthesis C-methyltransferase UbiE	P0A887	2.4	0.02	N.A.
		Glycogen phosphorylase	P0AC86	2.2	0.01	N.A.
		Maltodextrin phosphorylase	P00490	2.1	0.04	N.A.
		Thymidine phosphorylase	P07650	2.1	0.01	N.A.
		Protein-export protein SecB	P0AG86	2.0	0.01	N.A.
		Integration host factor subunit beta	P0A6Y1	2.0	0.04	N.A.
		Cold shock-like protein CspE	P0A972	2.0	0.03	N.A.
		Fatty acid metabolism regulator protein	P0A8V6	1.9	0.02	N.A.
	Aerobic vs. Anaerobic	Lipoyl synthase	P60716	2.2	0.04	[4Fe-4S]
		Translation initiation factor IF-3[b]	P0A707	2.2	0.00	N.A.
		Ribosomal protein S12 methylthiotransferase RimO[b]	P0AEI4	2.3	0.02	[4Fe-4S]
		Dihydrolipoyllysine-residue acetyltransferase component of pyruvate dehydrogenase complex	P06959	2.4	0.01	N.A.
		Ribonucleotide monophosphatase NagD	P0AF24	2.4	0.01	Mg^{2+}
		Ribosomal RNA large subunit methyltransferase K/L[b]	P75864	2.4	0.04	N.A.
		2-oxoglutarate dehydrogenase E1 component	P0AFG3	4.7	0.01	N.A.
		Alkyl hydroperoxide reductase C	P0AE08	5.4	0.05	N.A.

		Pyruvate/proton symporter BtsT	P39396	9.1	0.02	N.A.
		Bifunctional protein PutA	P09546	10.7	0.02	N.A.
No added Fe^{2+}	Anaerobic vs. Aerobic	L-threonine dehydratase catabolic TdcB	P0AGF6	137.5	0.00	N.A.
		Uncharacterized protein YfdQ	P76513	38.0	0.02	N.A.
		Hydrogenase-2 large chain	P0ACE0	31.5	0.01	Ni^{2+}
		Fumarate reductase iron-sulfur subunit	P0AC47	17.5	0.01	[2Fe-2S], [3Fe-4S], [4Fe-4S]
		Glycerol dehydrogenase	P0A9S5	16.9	0.01	Zn^{2+}
		Bacterial non-heme ferritin[a]	P0A998	14.9	0.00	N.A.
		Hydrogenase maturation factor HypB	P0AAN3	11.6	0.02	N.A.
		PFL-like enzyme TdcE	P42632	8.6	0.01	N.A.
		Aldehyde-alcohol dehydrogenase	P0A9Q7	7.2	0.01	Fe^{2+}
		Anaerobic ribonucleoside-triphosphate reductase	P28903	5.8	0.04	N.A.
		Aspartate ammonia-lyase	P0AC38	4.5	0.01	N.A.
		Uncharacterized protein YjjI	P37342	4.3	0.03	N.A.
		SCP2 domain-containing protein YhbT	P64599	4.1	0.01	N.A.
		2,3-bisphosphoglycerate-independent phosphoglycerate mutase	P37689	3.9	0.00	Mn^{2+}
		2-octaprenylphenol hydroxylase	P25535	3.7	0.05	N.A.
		Fructose-1,6-bisphosphatase 1 class 2	P0A9C9	3.3	0.03	Mn^{2+}
		Stationary-phase-induced ribosome-associated protein[b]	P68191	3.3	0.00	N.A.
		Evolved beta-galactosidase subunit alpha	P06864	3.2	0.04	N.A.
		Ribonuclease T	P30014	2.8	0.03	Mg^{2+}
		UPF0227 protein YcfP	P0A8E1	2.5	0.03	N.A.
		UPF0313 protein YgiQ	Q46861	2.4	0.01	[4Fe-4S]
		Methionine--tRNA ligase	P00959	2.4	0.02	Zn^{2+}
		Polyphosphate kinase	P0A7B1	2.4	0.03	Mg^{2+}
		RecBCD enzyme subunit RecC	P07648	2.3	0.02	N.A.
		ADP-heptose--LPS heptosyltransferase 2	P37692	2.2	0.03	N.A.
	Aerobic vs. Anaerobic	RNA-binding protein YhbY	P0AGK4	2.2	0.01	N.A.
		Chaperone protein HscA	P0A6Z1	2.3	0.00	N.A.
		Cytochrome bd-I ubiquinol oxidase subunit 2	P0ABK2	2.3	0.03	heme
		5'-methylthioadenosine/S-adenosylhomocysteine nucleosidase	P0AF12	2.3	0.02	N.A.
		Ribosomal silencing factor RsfS[b]	P0AAT6	2.4	0.00	N.A.
		DNA topoisomerase 4 subunit B	P20083	2.7	0.01	Mg^{2+}
		Lipoyl synthase	P60716	3.0	0.01	[4Fe-4S]
		Transcriptional regulatory protein GlrR	P0AFU4	3.2	0.00	N.A.
		Modulator of FtsH protease HflC	P0ABC3	3.5	0.01	N.A.
		Ribosomal RNA small subunit methyltransferase A[b]	P06992	3.7	0.01	N.A.
		Pyruvate/proton symporter BtsT	P39396	5.8	0.04	N.A.
		Enterobactin synthase component B[a]	P0ADI4	8.0	0.01	Mg^{2+}
		Respiratory nitrate reductase 1 alpha chain	P09152	37.3	0.01	[4Fe-4S] Mo-bis-MGD

[a]Protein is involved in bacterial iron homeostasis; [b]Protein is involved in translation

Table A.2 – Proteins differentially expressed in ribosomes purified from cells grown with or without 1 mM added Fe^{2+}. Information on metal cofactors was taken from the UniProt entries for each protein.

Condition	Protein more abundant in	Protein name	UniProt ID	Fold more abundant	p-value	Metal cofactor
Anaerobic	1 mM added Fe vs. without added Fe	Transcriptional regulatory protein OmpR	P0AA16	2.0	0.01	N.A.
		UvrABC system protein B	P0A8F8	2.1	0.03	N.A.
		5'-methylthioadenosine/S-adenosylhomocysteine nucleosidase	P0AF12	2.3	0.04	N.A.
		Large ribosomal RNA subunit accumulation protein YceD[b]	P0AB28	2.3	0.01	N.A.
		ATP-dependent dethiobiotin synthetase BioD 2	P0A6E9	2.7	0.04	Mg^{2+}
		Phosphoribosylaminoimidazole-succinocarboxamide synthase	P0A7D7	2.7	0.01	N.A.
		Phosphoserine phosphatase	P0AGB0	4.1	0.02	Mg^{2+}
	Without added Fe vs. 1 mM added Fe	4-alpha-glucanotransferase	P15977	2.2	0.03	N.A.
Aerobic	1 mM added Fe vs. without added Fe	Probable 4-deoxy-4-formamido-L-arabinose-phosphoundecaprenol deformylase ArnD	P76472	2.0	0.01	N.A.
		GDP-mannose pyrophosphatase NudK	P37128	2.0	0.03	Mg^{2+}
		Uncharacterized protein YfdQ	P76513	2.1	0.02	N.A.
		Uncharacterized protein YciO	P0AFR4	2.1	0.00	N.A.
		ABC transporter ATP-binding protein ModF	P31060	3.1	0.04	N.A.
	Without added Fe vs. 1 mM added Fe	Enterobactin synthase component B[a]	P0ADI4	8.9	0.03	Mg^{2+}
		Fe(3+) dicitrate-binding periplasmic protein[a]	P15028	7.7	0.02	N.A.

[a]Protein is involved in bacterial iron homeostasis; [b]Protein is involved in translation

Table A.3 – Reaction kinetics of in-line cleavage

	Conditions	k_{obs} (10^{-5} sec^{-1})	No. cleavable phosphates	$[M^{2+}]$ (M)	k/phosphate (10^{-5} sec^{-1}, no. $phosphates^{-1}$, $[M^{2+}]^{-1}$)
This study					
Mg^{2+}, 23S rRNA	pH 7.6, 37°C	5	2905	0.025	0.07
Mg^{2+}, 16S rRNA	pH 7.6, 37°C	3	1541	0.025	0.08
Fe^{2+}, 23S rRNA	pH 7.6, 37°C	67	2905	0.001	23
Fe^{2+}, 16S rRNA	pH 7.6, 37°C	25	1541	0.001	16
Outside studies					
[a]Mg^{2+}, UpU	pH 5.6, 90°C	0.01	1	0.005	2.1
[b]Mg^{2+}, *S(ApG)	pH 9.5, 37°C	0.18	1	0.005	37
[c]Mg^{2+}, polyU	pH 5.6, 90°C	0.32	300	0.005	0.21
[d]Zn^{2+}, ApA	pH 5.1, 90°C	0.64	1	0.01	64
[e]Zn^{2+}, ApA	pH 7.0, 62.1°C	0.06	1	0.001	56

[a]Zn^{2+}, UpU	pH 5.6, 90°C	0.43	1	0.005	85
[f]Zn^{2+}, UpU	pH 7, 80°C	0.04	1	0.001	41
[c]Zn^{2+}, polyU	pH 5.6, 90°C	0.43	300	0.005	0.28
[g]Zn^{2+}, $Up(Tp)_7Tp$	pH 5.5, 37°C	0.50	1	0.01	50

[a]Kuusela & Lönnberg, 1993 (128); [b]Li & Breaker, 1999 (127); [c]Kuusela & Lönnberg, 1994 (143); [d]Kuusela & Lönnberg, 1996; [e]Ikenaga & Inoue, 1974 (144); [f]Breslow & Huang, 1991 (145); [g]Kuusela et al., 1995 (141).
*22 nucleotide DNA-RNA hybrid

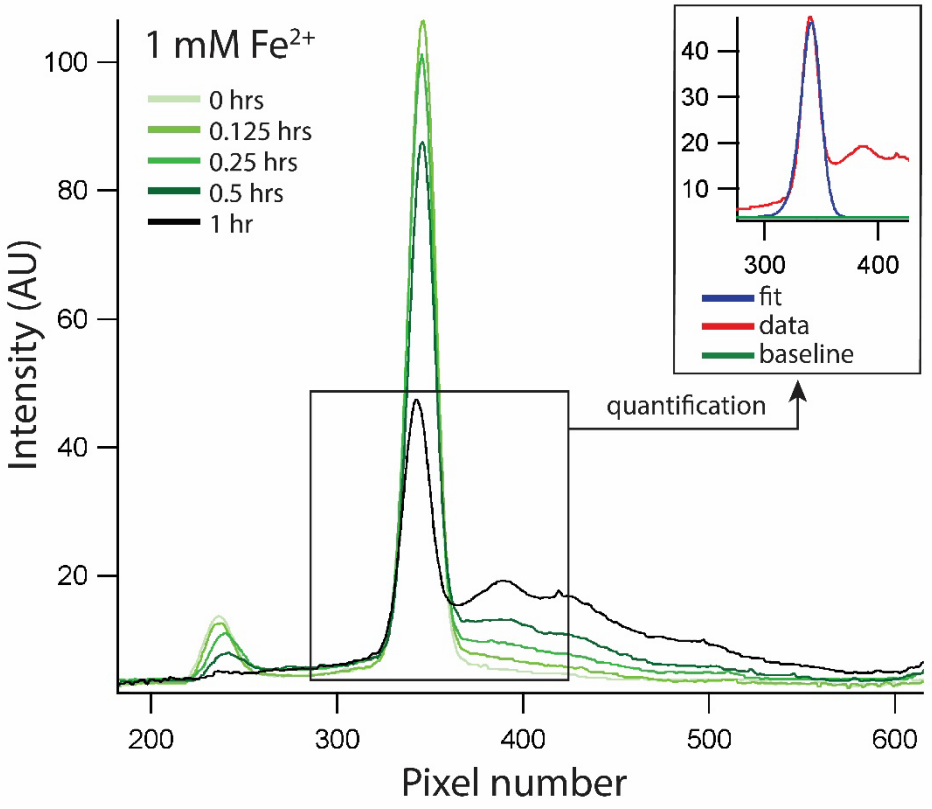

Figure A.1 – Example quantification of a gel scan for rRNA reactions with 1 mM Fe^{2+}. Shown here is a typical example of lane profiles and peak quantification for rRNA in-line cleavage reactions from a gel scan. Peak fitting was done in Igor Pro 7. The areas of quantified peaks were compiled and plotted in Figure 2.1. Figure in Ref. (98).

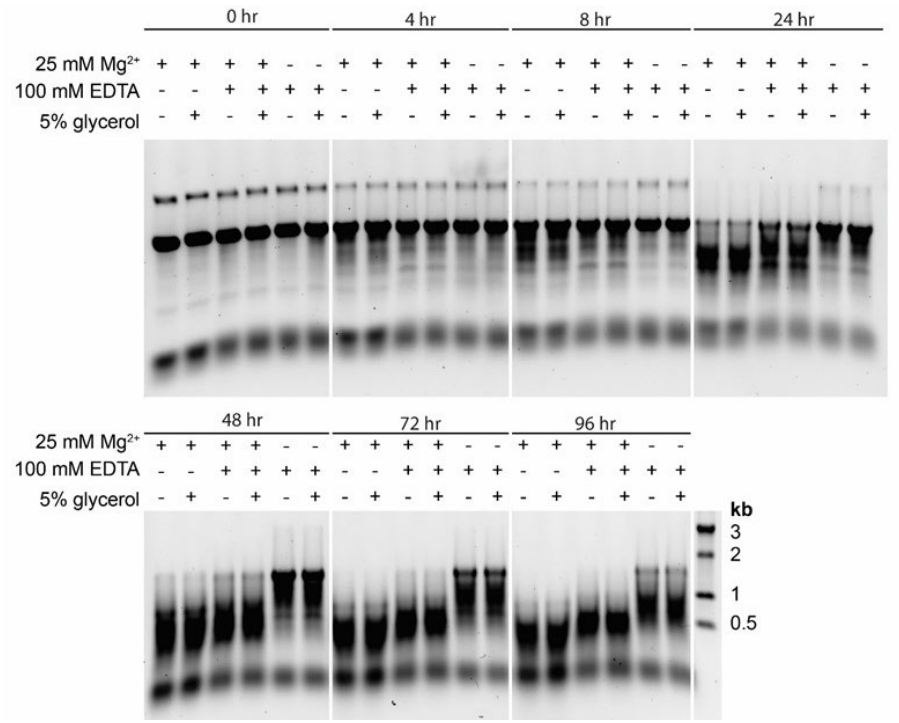

Figure A.2 – 1% agarose gel showing 5% v/v glycerol does not inhibit Mg^{2+} in-line cleavage of naked rRNA at 37ºC in air over the course of 96 hours. Chelation by 100 mM EDTA inhibits in-line cleavage, but there is no difference with and without 5% glycerol. Figure in Ref. (98).

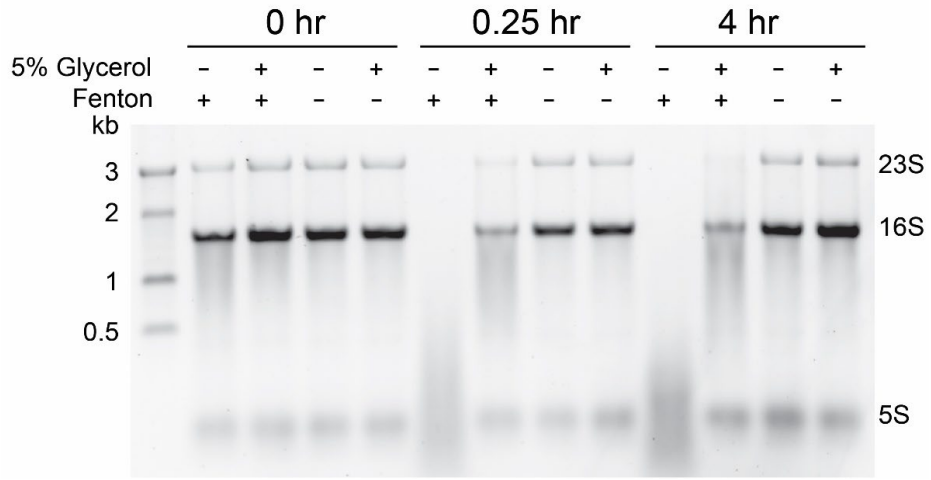

Figure A.3 – 1% agarose gel showing 5% v/v glycerol inhibition of Fenton chemistry against naked rRNA at 37ºC in air over the course of 4 hours. "+ Fenton" reactions contained 1 mM Fe^{2+}, 0.3% H_2O_2, 10 mM ascorbic acid, and 10 mM EDTA. "- Fenton" reactions contained 10 mM EDTA. Figure in Ref. (98).

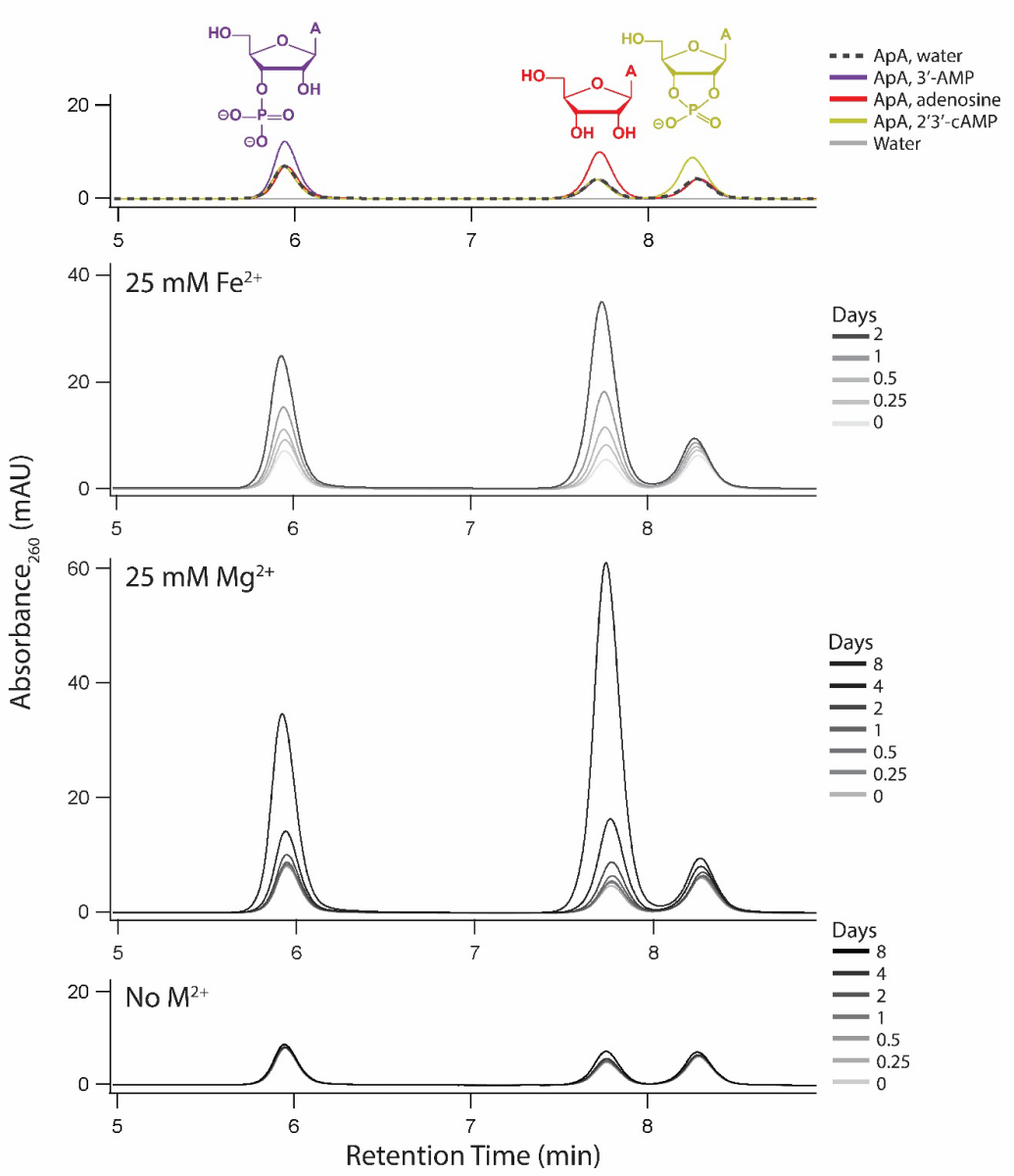

Figure A.4 – C18 column HPLC chromatograms of ApA reactions showing accumulation of the same products with Fe^{2+} and Mg^{2+}. 3'-AMP, adenosine, and 2',3'-cAMP standards (2.5 µM) were spiked into ApA solutions (0.5 mM ApA, 20 mM HEPES pH 7.6, 30 mM NaCl, 5% v/v glycerol) giving characteristic retention times for 3'-AMP, adenosine, and 2',3'-cAMP. ApA solutions (0.5 mM ApA, 20 mM HEPES pH 7.6, 30 mM NaCl, 5% v/v glycerol) anoxically incubated at 37°C with either 25 mM Fe^{2+} out to 2 days or 25 mM Mg^{2+} out to 8 days accumulate 3'-AMP, adenosine, and 2',3'-cAMP. 2',3'-cAMP peaks build to a lesser extent due to cyclic phosphate hydrolysis to form 3'-AMP or 2'-AMP. There is little cleavage product formation in the no metal (M^{2+}) control. Figure in Ref. (98).

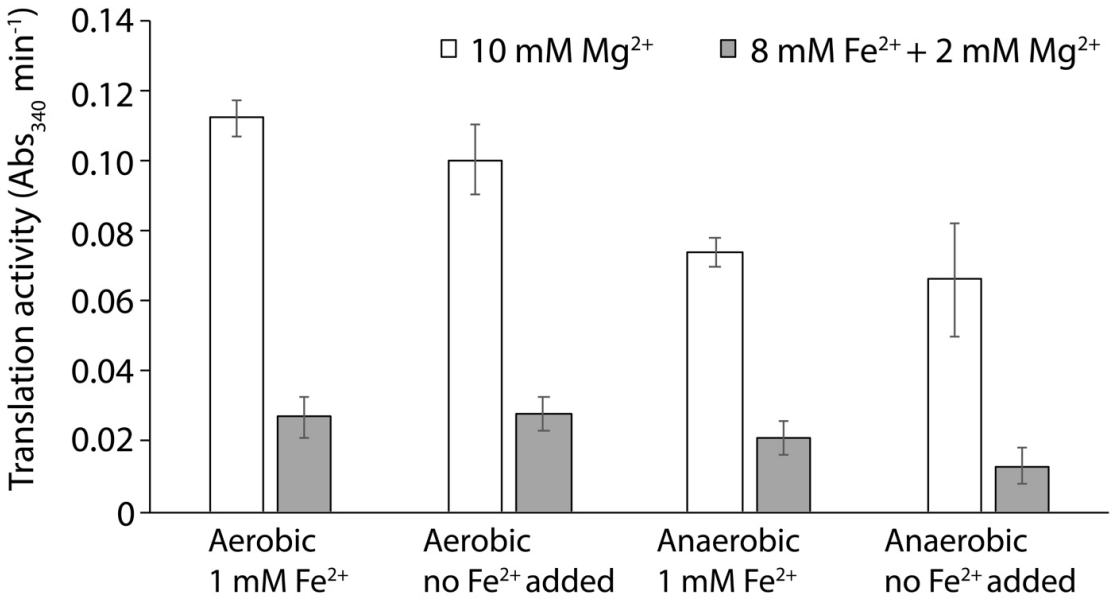

Figure A.5 – *In vitro* translation activity of purified ribosomes. Production of the protein dihydrofolate reductase (DHFR) from its mRNA was used to monitor translational activity. Protein synthesis was assayed by measuring the rate of NADPH oxidation at Abs_{340} by DHFR. Average values are reported ± standard error of the mean (n=4). All ribosomes were normalized to 9 mg mL^{-1} before adding to translation reactions. Figure in Ref. (98).

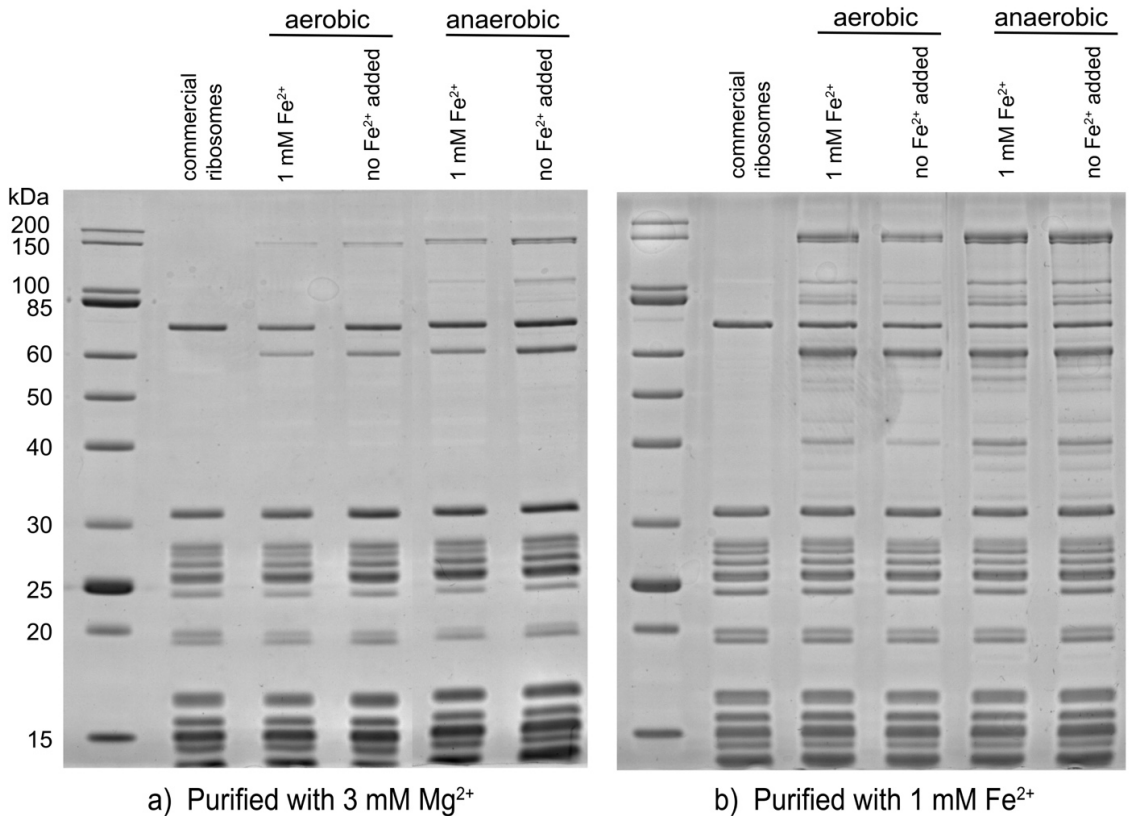

Figure A.6 – 12% SDS polyacrylamide gels for proteins from ribosomes purified in (a) 3 mM Mg^{2+} or (b) 1 mM Fe^{2+} compared to commercial ribosomes supplied by New England Biolabs. Figure in Ref. (98).

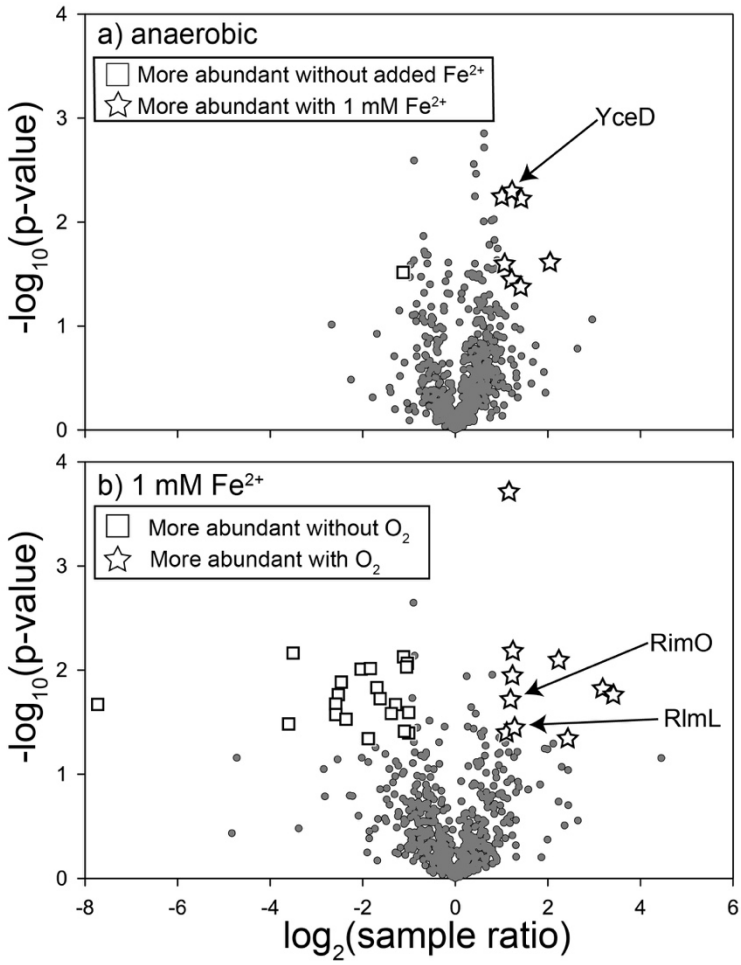

Figure A.7 – Differential protein abundance between ribosomes purified from cells grown under four growth conditions. Graphs display relative protein abundance in ribosome samples between two growth conditions. Black circles represent proteins not significantly more abundant in either sample. Gray rectangle and white stars represent proteins significantly more abundant in one of the samples. Proteins with a 2-fold or greater abundance in one sample versus another and a p-value less than or equal to 0.05 (n=3), were classified as significantly more abundant. Figure in Ref. (98).

APPENDIX B. SUPPLEMENTAL INFORMATION FOR CHAPTER 3

The lifetime of RNA with three states is given by Equation B.1:

$$lifetime = (k_{obs})^{-1} = \left(\frac{k_f[Mg^{2+}]}{1 + \left(\frac{K_D}{[Mg^{2+}]}\right)^n} + \left[1 - \frac{1}{1 + \left(\frac{K_D}{[Mg^{2+}]}\right)^n} \right] k_u[Mg^{2+}] \right)^{-1} \quad \textbf{(B.1)}$$

The overall lifetime can also be written simply as the proportional contributions of the lifetimes of RNA in each state (Equation B.2), where the fraction of RNA in each state adds to one (Equation B.3).

$$lifetime = f_u lifetime_u + f_i lifetime_i + f_f lifetime_f \quad \textbf{(B.2)}$$

$$lifetime = f_u lifetime_u + f_i lifetime_i + f_f lifetime_f \quad \textbf{(B.3)}$$

Table B.1 – Cytosolic free Mg^{2+} (non-complexed and unbound) concentrations in bacteria and eukarya. References (251,252) are compiled from previous studies.

Species and cell type	Free Mg^{2+} (mM)	Reference
Escherichia coli (bacterium)	0.8±0.2	(253)
Salmonella enterica (bacterium)	0.9-1.5	(254)
Saccharomyces cerevisiae (yeast)	0.9-2.0	(255)
Penicillium chrysogenum (fungi)	0.4-0.8	(255)
Endomyces magnusii (fungi)	0.4-1.6	(255)
Xenopus laevis (giant squid)	0.3	(256)
Skeletal muscle (human, mouse, frog, rat)	0.6-1.3	(251,257)
Cardiac myocytes (chicken, rat, guinea pig)	0.5-1.1	(251,252)
Smooth muscle cells (rabbit, rat, guinea pig)	0.3-1.0	(251)
Neuronal cells (human)	0.7-1.0	(251)
Exocrine cells (rat, lymphocytes)	0.2-0.4	(251)

Adrenal cells (rat)	0.5-0.9	(258)
Red blood cells (human)	0.3-1.9	(251,257)
Hepatocytes	0.3-0.7	(251)

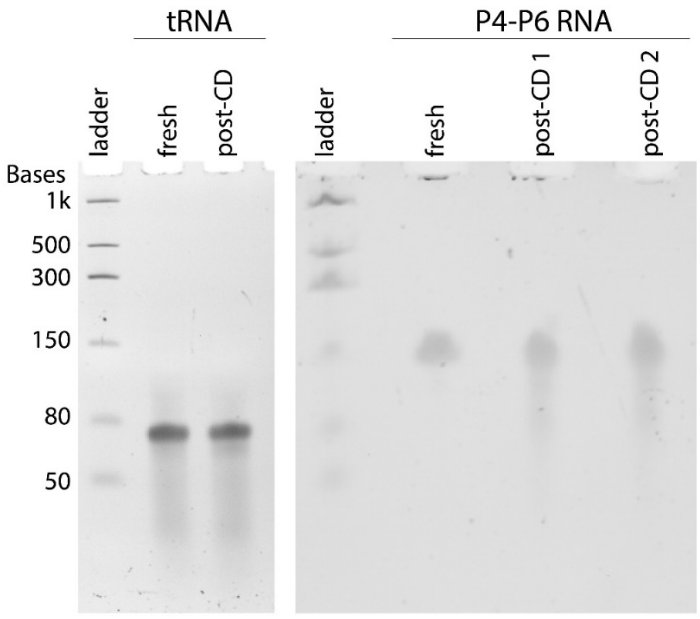

Figure B.1 – RNA cleavage is possible during long CD experiments. Yeast $tRNA^{Phe}$ showed little degredation during CD data acquisition. P4-P6 RNA showed some cleavage. P4-P6 RNA cleavage is greater than yeast $tRNA^{Phe}$ cleavage because CD data acquisition times were longer than for yeast $tRNA^{Phe}$, and because P4-P6 RNA is longer than yeast $tRNA^{Phe}$. Figure from Ref. (149).

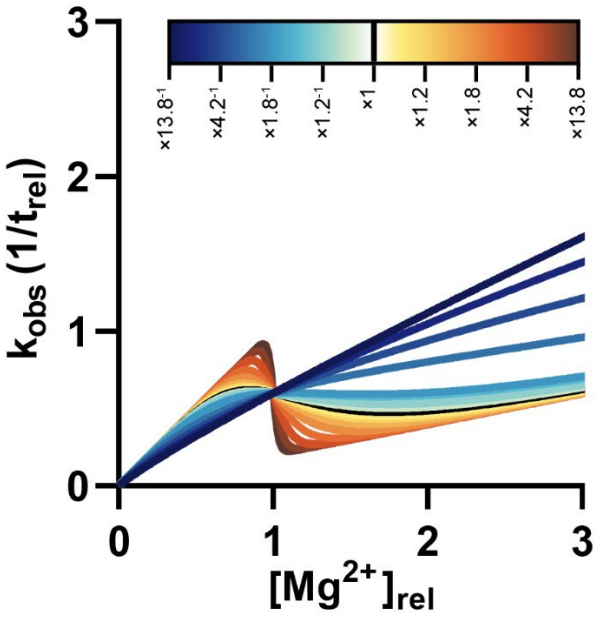

Figure B.2 – The Goldilocks peak requires cooperative binding of Mg^{2+} to RNA. k_{obs} is the reciprocal of lifetime. When lifetime rises k_{obs} decreases and vice versa. The k_{obs} vs. $[Mg^{2+}]$ graph has the advantage of straight trends and easy visualization. For very low n there is not an inflection of k_{obs} with increasing $[Mg^{2+}]$ (darker blue lines). So, lifetime does not increase, and no Goldilocks peak occurs. The same parameters and scale were used as in Figure 3.2D, where the initial n is equal to 4.1 (black line) and the various colors have n values that are the initial n multiplied by the indicated factor. Figure from Ref. (149).

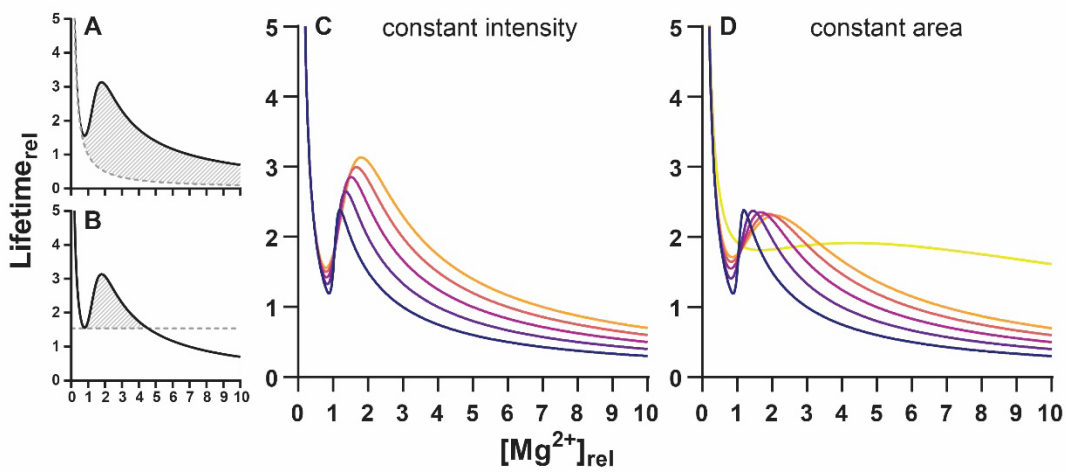

Figure B.3 – Methods for quantitation of Goldilocks behavior. (A) Goldilocks behavior is not quantified by the total difference in areas under the curves, because the two curves never converge. The bottom curve assumes no folding. (B) Goldilocks behavior is quantified by intensity, the ratio of lifetime at the local maximum to the lifetime at the preceding minimum. Alternatively, Goldilocks behavior is quantified by local area between the lifetime curve and a horizontal line at the local minimum. (C) Increasing local area calculated as shown in panel B with fixed intensity (= 2) and K_D (= 1 $[Mg^{2+}]_{rel}$) causes changes in RNA lifetime over an extended range of $[Mg^{2+}]$. (D) Peaks with fixed area calculated as in panel B and K_D (= 1 $[Mg^{2+}]_{rel}$) but different intensities illustrate the spectrum of differences in RNA lifetime. A high intensity peak (e.g. the darkest line) allows fine control of RNA lifetime with small changes in $[Mg^{2+}]$, while a lower intensity peak of the same area changes RNA lifetime over a larger $[Mg^{2+}]$ range. The Goldilocks landscape is essentially flat if the intensity is very low (yellow line). Figure from Ref. (149).

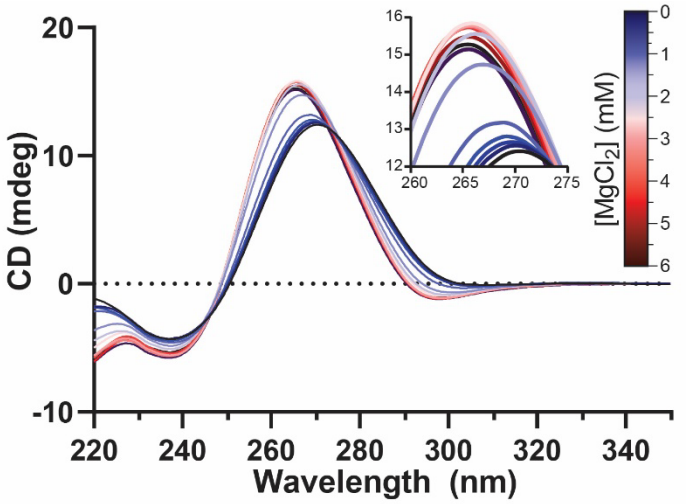

Figure B.4 – tRNA folds with increasing [Mg^{2+}]. Yeast $tRNA^{Phe}$ shows a change in CD spectra upon addition of $MgCl_2$ indicating a Mg^{2+}-induced structural transition. To extract the fraction of full-length RNA from the spectra, the theta values at 260 nm were corrected for dilution upon $MgCl_2$ addition then plotted against the [Mg^{2+}]. The experiment was run in 180 mM NaCl, 50 mM HEPES pH 7.1 at 65°C with variable $MgCl_2$. Figure from Ref. (149).

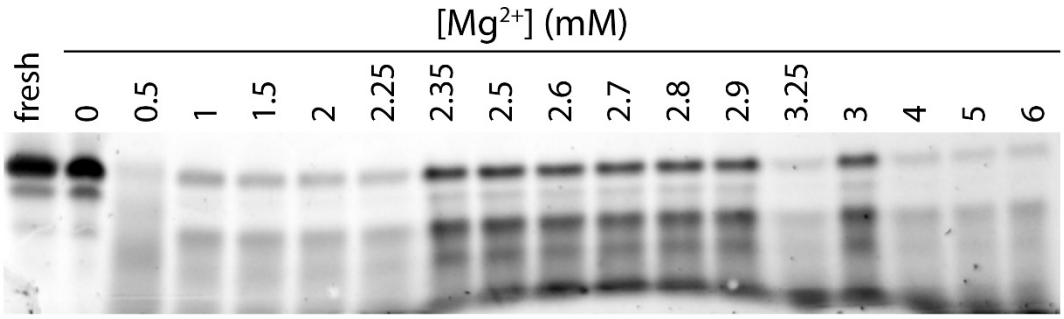

Figure B.5 – the fraction of intact tRNA has a multiphasic response to increasing [Mg^{2+}]. A representative gel of yeast $tRNA^{Phe}$ after no reaction (fresh) or 48 hours of cleavage shows that the fraction of intact RNA first decreases, then increases, then decreases again when exposed to increasing [Mg^{2+}]. Quantification in our gels of the top band, i.e. the full-length band, produced our fraction intact and lifetime data. The re-emergence of the full-length band does not depend on position in the gel, shown by loading some samples out of order. Figure from Ref. (149).

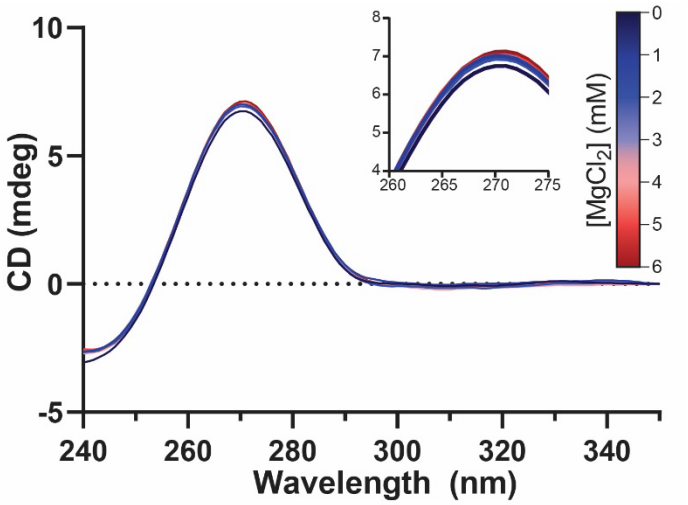

Figure B.6 – rU_{20} does not fold. rU_{20} does not show a change in CD spectra upon addition of $MgCl_2$ as expected for a non-folding RNA. The experiment was run in 180 mM NaCl, 50 mM HEPES pH 7.1 at 65°C with variable $MgCl_2$. Figure from Ref. (149).

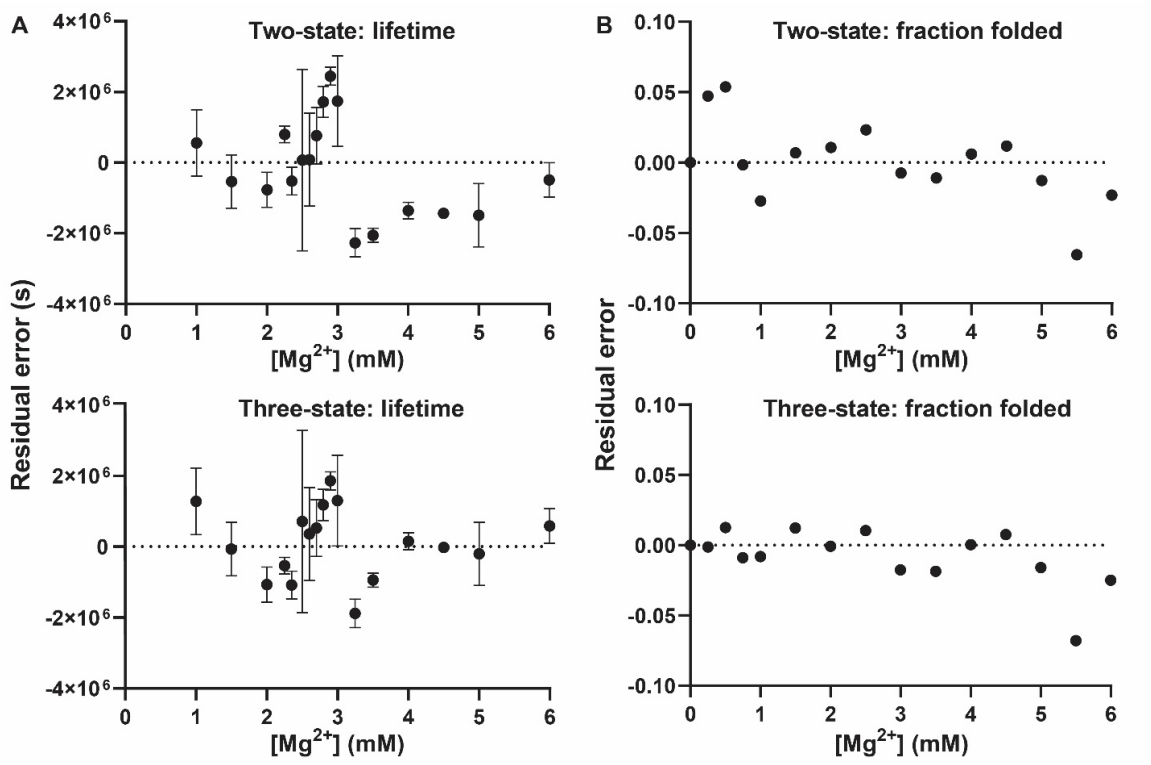

Figure B.7 – The tRNA lifetime and folding residual errors are minimized by the three-state model. (A) For the two-state model the lifetime errors are large and non-random; all the mean errors are positive between 2.8 and 3.0 mM Mg^{2+} and are negative for all values of [Mg^{2+}] greater than 3.0. For the three-state model the errors appear to be more randomly distributed around zero. (B) Errors in folding are minimized by the three-state model below 2.5 mM Mg^{2+}, showing better approximation of an early transition state. Figure from Ref. (149).

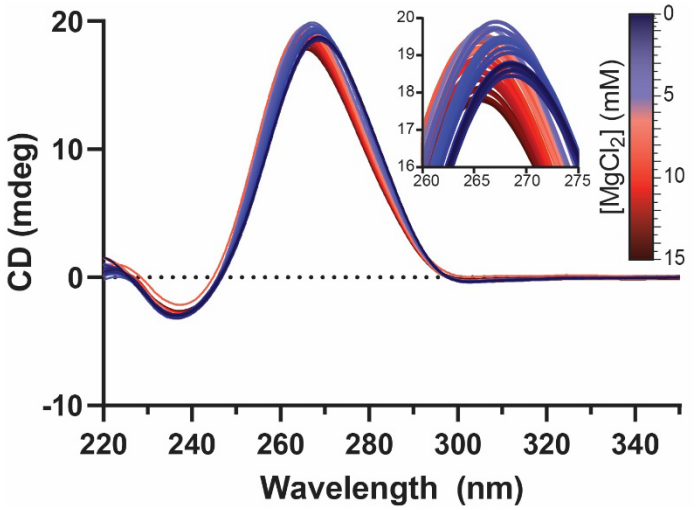

Figure B.8 – P4-P6 RNA folds with increasing [Mg^{2+}]. P4-P6 RNA shows a change in CD spectra upon addition of $MgCl_2$ indicating a Mg^{2+}-induced structural transition. The initial rise in peak height is the Mg^{2+} folding response, which is followed by a peak decrease, the effect of dilution when adding Mg^{2+} that becomes apparent when the RNA has completed folding. To extract the fraction of full-length RNA from the spectra, the theta values at 260.6 nm were corrected for dilution then plotted against the [Mg^{2+}]. The experiment was run in 180 mM NaCl, 50 mM HEPES pH 7.1 at 65°C with variable $MgCl_2$. Figure from Ref. (149).

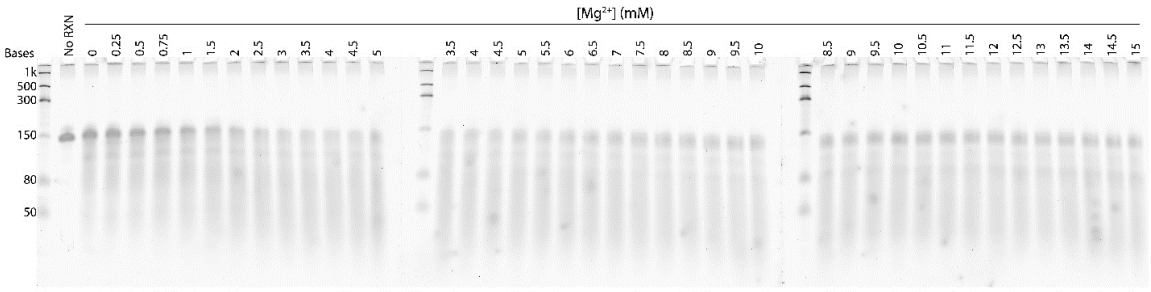

Figure B.9 – the fraction of intact P4-P6 RNA has a multiphasic response to increasing [Mg^{2+}]. A representative gel of P4-P6 RNA after 48 hours of cleavage shows that the fraction of intact RNA first decreases, then increases, then decreases again when exposed to increasing [Mg^{2+}]. A surplus of prepared RNA allowed a single mixture to be added to up two gels. In this way each gel was made to share four samples with its neighboring gel allowing for normalization between gels and for the running of the large number of samples. Additionally, running and then imaging was performed simultaneously for the three gels. Figure from Ref. (149).

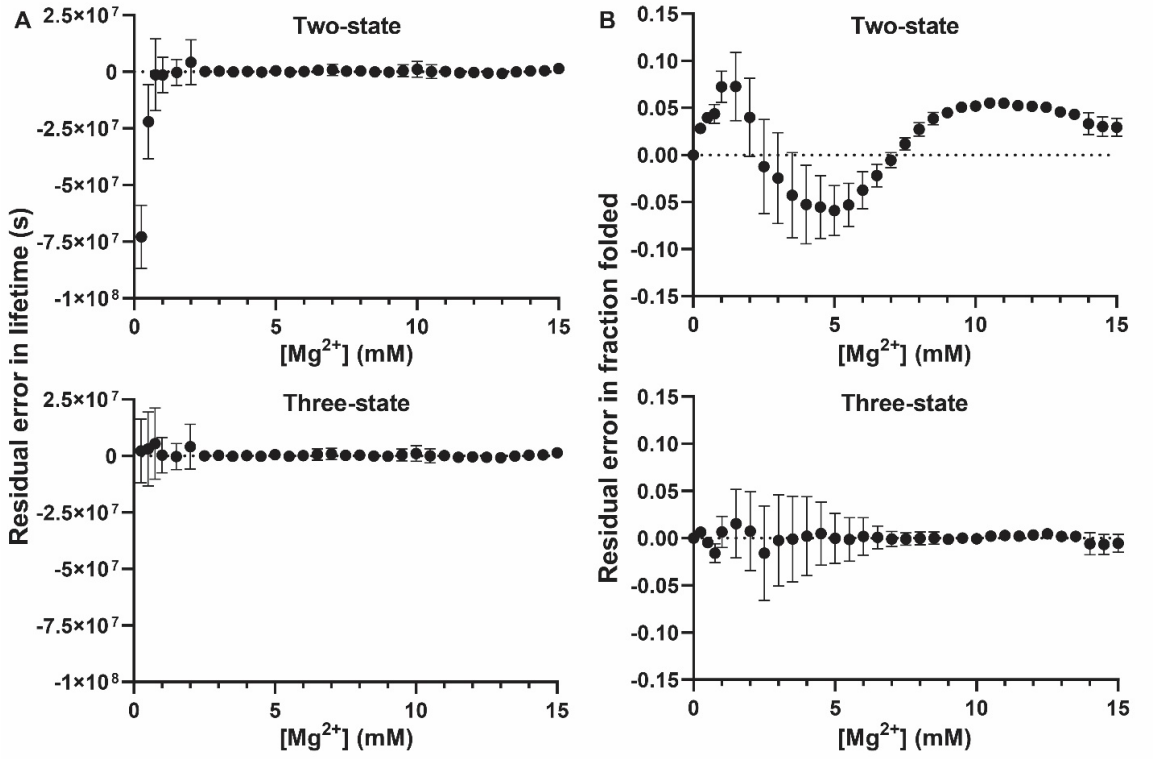

Figure B.10 – P4-P6 RNA has an apparent transition to an intermediate folding state at low [Mg^{2+}]. (A) Lifetime residuals between two- and three-state models only differ at low [Mg^{2+}] where only the three-state model captures the data of an apparent early folding state. (B) Residual error in the two-state model systematically weaves above and below zero while the three-state difference is smaller and spreads randomly near zero. The three-state fit is a more accurate representation of the folding of P4-P6 RNA again showing an intermediate state between unfolded and folded. Figure from Ref. (149).

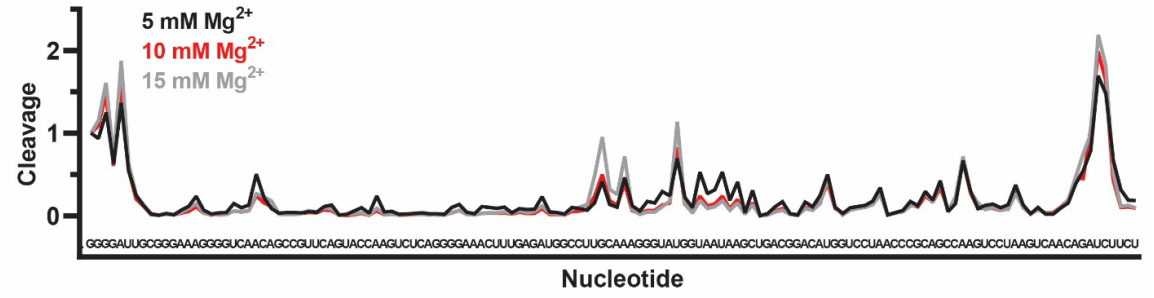

Figure B.11 – P4-P6 RNA cleavage changes at specific sites with changing [Mg^{2+}]. The data from Figure 3.7 is shown with absolute cleavage values (relative to cleavage at the first nucleotide). Each trend is an average of two replicates. Figure from Ref. (149).

REFERENCES

1. Kolb, V.M. (2018) *Handbook of Astrobiology*. CRC Press.

2. Javaux, E.J. (2019) Challenges in Evidencing the Earliest Traces of Life. *Nature*, **572**, 451-460.

3. Benner, S.A. (2010) Defining Life. *Astrobiology*, **10**, 1021-1030.

4. Pross, A. and Pascal, R. (2013) The Origin of Life: What We Know, What We Can Know and What We Will Never Know. *Open biology*, **3**, 120190.

5. Hud, Nicholas V., Cafferty, Brian J., Krishnamurthy, R. and Williams, Loren D. (2013) The Origin of RNA and "My Grandfather's Axe". *Chemistry & Biology*, **20**, 466-474.

6. Koonin, E.V. (2003) Comparative Genomics, Minimal Gene-Sets and the Last Universal Common Ancestor. *Nat Rev Microbiol*, **1**, 127-136.

7. Koonin, E.V., Krupovic, M., Ishino, S. and Ishino, Y. (2020) The Replication Machinery of LUCA: Common Origin of DNA Replication and Transcription. *BMC Biol*, **18**, 61.

8. Ribas de Pouplana, L., Forterre, P., Filée, J. and Myllykallio, H. (2004) Origin and Evolution of DNA and DNA Replication Machineries. *The genetic code and the origin of life*, 145-168.

9. Furukawa, Y., Nakazawa, H., Sekine, T., Kobayashi, T. and Kakegawa, T. (2015) Nucleobase and Amino Acid Formation through Impacts of Meteorites on the Early Ocean. *Earth Planet Sci Lett*, **429**, 216-222.

10. Ferus, M., Pietrucci, F., Saitta, A.M., Knížek, A., Kubelík, P., Ivanek, O., Shestivska, V. and Civiš, S. (2017) Formation of Nucleobases in a Miller–Urey Reducing Atmosphere. *Proc Natl Acad Sci USA*, **114**, 4306-4311.

11. Lanier, K.A., Petrov, A.S. and Williams, L.D. (2017) The Central Symbiosis of Molecular Biology: Molecules in Mutualism. *J Mol Evol*, **85**, 8-13.

12. Schuster, P. and Stadler, P.F. (2008) In Domingo, E., Parrish, C. R. and Holland, J. J. (eds.), *Origin and Evolution of Viruses (Second Edition)*. Academic Press, London, pp. 1-41.

13. Manrubia, S., Cuesta, J.A., Aguirre, J., Ahnert, S.E., Altenberg, L., Cano, A.V., Catalán, P., Diaz-Uriarte, R., Elena, S.F., García-Martín, J.A., Hogeweg, P., Khatri, B.S., Krug, J., Louis, A.A., Martin, N.S., Payne, J.L., Tarnowski, M.J. and Weiß, M. (2021) From Genotypes to Organisms: State-of-the-Art and Perspectives of a Cornerstone in Evolutionary Dynamics. *Physics of Life Reviews*, **38**, 55-106.

14. Strauss, J.H. and Strauss, E.G. (1988) Evolution of RNA Viruses. *Annual Reviews in Microbiology*, **42**, 657-683.

15. Mat, W.-K., Xue, H. and Wong, J.T.-F. (2008) The Genomics of LUCA. *FBL*, **13**, 5605-5613.

16. Weiss, M.C., Sousa, F.L., Mrnjavac, N., Neukirchen, S., Roettger, M., Nelson-Sathi, S. and Martin, W.F. (2016) The Physiology and Habitat of the Last Universal Common Ancestor. *Nat Microbiol*, **1**, 16116.

17. Mushegian, A. (2008) Gene Content of LUCA, the Last Universal Common Ancestor. *Frontiers in Bioscience-Landmark*, **13**, 4657-4666.

18. Ouzounis, C.A., Kunin, V., Darzentas, N. and Goldovsky, L. (2006) A Minimal Estimate for the Gene Content of the Last Universal Common Ancestor—Exobiology from a Terrestrial Perspective. *Res Microbiol*, **157**, 57-68.

19. Isenbarger, T.A., Carr, C.E., Johnson, S.S., Finney, M., Church, G.M., Gilbert, W., Zuber, M.T. and Ruvkun, G. (2008) The Most Conserved Genome Segments for Life Detection on Earth and Other Planets. *Orig Life Evol Biosph*, **38**, 517-533.

20. Woese, C.R., Fox, G.E., Zablen, L., Uchida, T., Bonen, L., Pechman, K., Lewis, B.J. and Stahl, D. (1975) Conservation of Primary Structure in 16S Ribosomal RNA. *Nature*, **254**, 83-86.

21. Petrov, A.S., Bernier, C.R., Hsiao, C., Norris, A.M., Kovacs, N.A., Waterbury, C.C., Stepanov, V.G., Harvey, S.C., Fox, G.E., Wartell, R.M., Hud, N.V. and

Williams, L.D. (2014) Evolution of the Ribosome at Atomic Resolution. *Proc Natl Acad Sci USA*, **111**, 10251-10256.

22. Kruger, K., Grabowski, P.J., Zaug, A.J., Sands, J., Gottschling, D.E. and Cech, T.R. (1982) Self-Splicing RNA: Autoexcision and Autocyclization of the Ribosomal RNA Intervening Sequence of *Tetrahymena*. *Cell*, **31**, 147-157.

23. Guerrier-Takada, C., Gardiner, K., Marsh, T., Pace, N. and Altman, S. (1983) The RNA Moiety of Ribonuclease P Is the Catalytic Subunit of the Enzyme. *Cell*, **35**, 849-857.

24. Silverman, S.K. (2008) Nucleic Acid Enzymes (Ribozymes and Deoxyribozymes): In Vitro Selection and Application. *Wiley Encyclopedia of Chemical Biology: John Wiley & Sons, Inc*.

25. Cech, T.R. (2000) The Ribosome Is a Ribozyme. *Science*, **289**, 878-879.

26. Lark, K.G. (1972) Evidence for the Direct Involvement of RNA in the Initiation of DNA Replication in Escherichia coli 15T−. *Journal of molecular biology*, **64**, 47-60.

27. Stark, B.C., Kole, R., Bowman, E.J. and Altman, S. (1978) Ribonuclease P: An Enzyme with an Essential RNA Component. *Proc Natl Acad Sci USA*, **75**, 3717-3721.

28. Brouns, S.J.J., Jore, M.M., Lundgren, M., Westra, E.R., Slijkhuis, R.J.H., Snijders, A.P.L., Dickman, M.J., Makarova, K.S., Koonin, E.V. and Van Der Oost, J. (2008) Small CRISPR RNAs Guide Antiviral Defense in Prokaryotes. *Science*, **321**, 960-964.

29. Lee, R.C., Feinbaum, R.L. and Ambros, V. (1993) The *C. elegans* Heterochronic Gene Lin-4 Encodes Small RNAs with Antisense Complementarity to Lin-14. *Cell*, **75**, 843-854.

30. Wightman, B., Ha, I. and Ruvkun, G. (1993) Posttranscriptional Regulation of the Heterochronic Gene Lin-14 by Lin-4 Mediates Temporal Pattern Formation in *C. elegans*. *Cell*, **75**, 855-862.

31. Wassarman, K.M. and Storz, G. (2000) 6s RNA Regulates *E. coli* RNA Polymerase Activity. *Cell*, **101**, 613-623.

32. Nahvi, A., Sudarsan, N., Ebert, M.S., Zou, X., Brown, K.L. and Breaker, R.R. (2002) Genetic Control by a Metabolite Binding mRNA. *Chem Biol*, **9**, 1043.

33. Winkler, W., Nahvi, A. and Breaker, R.R. (2002) Thiamine Derivatives Bind Messenger RNAs Directly to Regulate Bacterial Gene Expression. *Nature*, **419**, 952-956.

34. Altuvia, S., Kornitzer, D., Teff, D. and Oppenheim, A.B. (1989) Alternative mRNA Structures of the cIII Gene of Bacteriophage Λ Determine the Rate of Its Translation Initiation. *Journal of Molecular Biology*, **210**, 265-280.

35. de la Fuente, M., Valera, S. and Martínez-Guitarte, J.L. (2012) ncRNAs and Thermoregulation: A View in Prokaryotes and Eukaryotes. *FEBS letters*, **586**, 4061-4069.

36. Irastortza-Olaziregi, M. and Amster-Choder, O. (2021) RNA Localization in Prokaryotes: Where, When, How, and Why. *WIREs RNA*, **12**, e1615.

37. Fay, M.M. and Anderson, P.J. (2018) The Role of RNA in Biological Phase Separations. *Journal of molecular biology*, **430**, 4685-4701.

38. Chu, X.-Y., Xu, Y.-Y., Tong, X.-Y., Wang, G. and Zhang, H.-Y. (2022) The Legend of ATP: From Origin of Life to Precision Medicine. *Metabolites*, **12**, 461.

39. Åqvist, J. and Kamerlin, S.C.L. (2015) Exceptionally Large Entropy Contributions Enable the High Rates of GTP Hydrolysis on the Ribosome. *Scientific Reports*, **5**, 15817.

40. Gancedo, J.M. (2013) Biological Roles of cAMP: Variations on a Theme in the Different Kingdoms of Life. *Biological Reviews*, **88**, 645-668.

41. Martin, W.F. (2020) Older Than Genes: The Acetyl CoA Pathway and Origins. *Frontiers in microbiology*, **11**, 817.

42. Gossmann, T.I., Ziegler, M., Puntervoll, P., de Figueiredo, L.F., Schuster, S. and Heiland, I. (2012) NAD+ Biosynthesis and Salvage – a Phylogenetic Perspective. *The FEBS Journal*, **279**, 3355-3363.

43. Sánchez-Pérez, G.F., Bautista, J.M. and Pajares, M.a.A. (2004) Methionine Adenosyltransferase as a Useful Molecular Systematics Tool Revealed by Phylogenetic and Structural Analyses. *Journal of Molecular Biology*, **335**, 693-706.

44. Drenth, J. and Fraaije, M.W. (2021), *Flavin-Based Catalysis*, pp. 29-65.

45. White, H.B. (1976) Coenzymes as Fossils of an Earlier Metabolic State. *J Mol Evol*, **7**, 101-104.

46. Kazakov, S. and Hecht, S. (2006).

47. Bowman, J.C., Lenz, T.K., Hud, N.V. and Williams, L.D. (2012) Cations in Charge: Magnesium Ions in RNA Folding and Catalysis. *Current Opinion in Structural Biology*, **22**, 262-272.

48. Sosnick, T.R. (2001) Characterization of Tertiary Folding of RNA by Circular Dichroism and Urea. *Curr Protoc Nucleic Acid Chem*, **Chapter 11**, Unit 11 15.

49. Hsiao, C., Chou, I.-C., Okafor, C.D., Bowman, J.C., O'neill, E.B., Athavale, S.S., Petrov, A.S., Hud, N.V., Wartell, R.M., Harvey, S.C. and Williams, L.D. (2013) RNA with Iron (II) as a Cofactor Catalyses Electron Transfer. *Nat Chem*, **5**, 525-528.

50. Ward, W.L., Plakos, K. and DeRose, V.J. (2014) Nucleic Acid Catalysis: Metals, Nucleobases, and Other Cofactors. *Chemical Reviews*, **114**, 4318-4342.

51. Frederiksen, J.K., Fong, R. and Piccirilli, J.A. (2009), *Nucleic Acid-Metal Ion Interactions*. The Royal Society of Chemistry, pp. 260-306.

52. Manning, G.S. (1978) The Molecular Theory of Polyelectrolyte Solutions with Applications to the Electrostatic Properties of Polynucleotides. *Quarterly Reviews of Biophysics*, **11**, 179-246.

53. Draper, D.E. (2008) RNA Folding: Thermodynamic and Molecular Descriptions of the Roles of Ions. *Biophysical Journal*, **95**, 5489-5495.

54. Grilley, D., Soto, A.M. and Draper, D.E. (2006) Mg^{2+}–RNA Interaction Free Energies and Their Relationship to the Folding of RNA Tertiary Structures. *Proc Natl Acad Sci USA*, **103**, 14003.

55. Templeton, C. and Elber, R. (2018) Why Does RNA Collapse? The Importance of Water in a Simulation Study of Helix–Junction–Helix Systems. *J Am Chem Soc*, **140**, 16948-16951.

56. DRAPER, D.E. (2004) A Guide to Ions and RNA Structure. *RNA*, **10**, 335-343.

57. Sarbak, S., Kujawa, M., Jurga-Nowak, H. and Dobek, A. (2015) Sodium Chloride-Induced Conformational Change in tRNA as Measured by Circular Dichroism. *Current Topics in Biophysics*, **38**, 1-5.

58. Kim, H.D., Nienhaus, G.U., Ha, T., Orr, J.W., Williamson, J.R. and Chu, S. (2002) Mg^{2+}-Dependent Conformational Change of RNA Studied by Fluorescence Correlation and FRET on Immobilized Single Molecules. *Proc Natl Acad Sci USA*, **99**, 4284-4289.

59. Lambert, D., Leipply, D., Shiman, R. and Draper, D.E. (2009) The Influence of Monovalent Cation Size on the Stability of RNA Tertiary Structures. *Journal of Molecular Biology*, **390**, 791-804.

60. Glasner, M.E., Bergman, N.H. and Bartel, D.P. (2002) Metal Ion Requirements for Structure and Catalysis of an RNA Ligase Ribozyme. *Biochemistry*, **41**, 8103-8112.

61. Rangan, P. and Woodson, S.A. (2003) Structural Requirement for Mg^{2+} Binding in the Group I Intron Core. *Journal of Molecular Biology*, **329**, 229-238.

62. Petrov, A.S., Bowman, J.C., Harvey, S.C. and Williams, L.D. (2011) Bidentate RNA–Magnesium Clamps: On the Origin of the Special Role of Magnesium in RNA Folding. *RNA*, **17**, 291-297.

63. Bukhman, Y.V. and Draper, D.E. (1997) Affinities and Selectivities of Divalent Cation Binding Sites within an RNA Tertiary Structure. *Journal of Molecular Biology*, **273**, 1020-1031.

64. Forconi, M. and Herschlag, D. (2009) Metal Ion-Based RNA Cleavage as a Structural Probe. *Methods Enzymol*, **468**, 91-106.

65. Brown, R.S., Dewan, J.C. and Klug, A. (1985) Crystallographic and Biochemical Investigation of the Lead(II)-Catalyzed Hydrolysis of Yeast Phenylalanine tRNA. *Biochemistry*, **24**, 4785-4801.

66. Morrow, J.R., Amyes, T.L. and Richard, J.P. (2008) Phosphate Binding Energy and Catalysis by Small and Large Molecules. *Acc Chem Res*, **41**, 539-548.

67. Lönnberg, H. (2011) Cleavage of RNA Phosphodiester Bonds by Small Molecular Entities: A Mechanistic Insight. *Organic & Biomolecular Chemistry*, **9**, 1687-1703.

68. Mikkola, S., Stenman, E., Nurmi, K., Yousefi-Salakdeh, E., Strömberg, R. and Lönnberg, H. (1999) The Mechanism of the Metal Ion Promoted Cleavage of RNA Phosphodiester Bonds Involves a General Acid Catalysis by the Metal Aquo Ion on the Departure of the Leaving Group. *J Chem Soc Perk Trans 2*, 1619-1626.

69. Cassano, A.G., Anderson, V.E. and Harris, M.E. (2004) Understanding the Transition States of Phosphodiester Bond Cleavage: Insights from Heavy Atom Isotope Effects. *Biopolymers*, **73**, 110-129.

70. Murray, J.B., Seyhan, A.A., Walter, N.G., Burke, J.M. and Scott, W.G. (1998) The Hammerhead, Hairpin and Vs Ribozymes Are Catalytically Proficient in Monovalent Cations Alone. *Chemistry & Biology*, **5**, 587-595.

71. Sigel, R.K.O. and Pyle, A.M. (2007) Alternative Roles for Metal Ions in Enzyme Catalysis and the Implications for Ribozyme Chemistry. *Chemical Reviews*, **107**, 97-113.

72. Lippert, B. (2008) Ligand-pK_a Shifts through Metals: Potential Relevance to Ribozyme Chemistry. *Chem Biodivers*, **5**, 1455-1474.

73. Roychowdhury-Saha, M. and Burke, D.H. (2007) Distinct Reaction Pathway Promoted by Non-Divalent-Metal Cations in a Tertiary Stabilized Hammerhead Ribozyme. *RNA*, **13**, 841-848.

74. Perrotta, A.T. and Been, M.D. (2006) HDV Ribozyme Activity in Monovalent Cations. *Biochemistry*, **45**, 11357-11365.

75. Cruz-León, S. and Schwierz, N. (2020) Hofmeister Series for Metal-Cation–RNA Interactions: The Interplay of Binding Affinity and Exchange Kinetics. *Langmuir*, **36**, 5979-5989.

76. Lippert, B. (2000) Multiplicity of Metal Ion Binding Patterns to Nucleobases. *Coordination Chemistry Reviews*, **200-202**, 487-516.

77. Wacker, W.E.C. (1969) The Biochemistry of Magnesium. *Annals of the New York Academy of Sciences*, **162**, 717-726.

78. Hurwitz, C. and Rosano, C.L. (1967) The Intracellular Concentration of Bound and Unbound Magnesium Ions in *Escherichia coli*. *J Biol Chem*, **242**, 3719-3722.

79. Shelton, V.M., Sosnick, T.R. and Pan, T. (2001) Altering the Intermediate in the Equilibrium Folding of Unmodified Yeast-tRNA^{Phe} with Monovalent and Divalent Cations. *Biochemistry*, **40**, 3629-3638.

80. Pan, J., Thirumalai, D. and Woodson, S.A. (1999) Magnesium-Dependent Folding of Self-Splicing RNA: Exploring the Link between Cooperativity, Thermodynamics, and Kinetics. *Proc Natl Acad Sci USA*, **96**, 6149.

81. Friederich, M.W. and Hagerman, P.J. (1997) The Angle between the Anticodon and Aminoacyl Acceptor Stems of Yeast-tRNA^{Phe} Is Strongly Modulated by Magnesium Ions. *Biochemistry*, **36**, 6090-6099.

82. Koculi, E., Hyeon, C., Thirumalai, D. and Woodson, S.A. (2007) Charge Density of Divalent Metal Cations Determines RNA Stability. *J Am Chem Soc*, **129**, 2676-2682.

83. Brown, I.D. (1988) What Factors Determine Cation Coordination Numbers? *Acta Crystallogr Sect B: Struct Sci*, **44**, 545-553.

84. Kepp, K.P. (2018) Thermochemically Consistent Free Energies of Hydration for Di- and Trivalent Metal Ions. *The Journal of Physical Chemistry A*, **122**, 7464-7471.

85. Jackson, V.E., Felmy, A.R. and Dixon, D.A. (2015) Prediction of the pK_a's of Aqueous Metal Ion +2 Complexes. *The Journal of Physical Chemistry A*, **119**, 2926-2939.

86. Holland, H.D. (1973) The Oceans; a Possible Source of Iron in Iron-Formations. *Econ Geol*, **68**, 1169-1172.

87. Holland, H.D. (2006) The Oxygenation of the Atmosphere and Oceans. *Philos Trans R Soc London, Ser B*, **361**, 903-915.

88. Hazen, R.M. and Ferry, J.M. (2010) Mineral Evolution: Mineralogy in the Fourth Dimension. *Elements*, **6**, 9-12.

89. Anbar, A.D. (2008) OCEANS: Elements and Evolution. *Science*, **322**, 1481-1483.

90. Klein, C. (2005) Some Precambrian Banded Iron-Formations (BIFs) from around the World: Their Age, Geologic Setting, Mineralogy, Metamorphism, Geochemistry, and Origins. *Am Mineral*, **90**, 1473-1499.

91. Pogozelski, W.K. and Tullius, T.D. (1998) Oxidative Strand Scission of Nucleic Acids: Routes Initiated by Hydrogen Abstraction from the Sugar Moiety. *Chemical Reviews*, **98**, 1089-1108.

92. Athavale, S.S., Petrov, A.S., Hsiao, C., Watkins, D., Prickett, C.D., Gossett, J.J., Lie, L., Bowman, J.C., O'Neill, E., Bernier, C.R., Hud, N.V., Wartell, R.M., Harvey, S.C. and Williams, L.D. (2012) RNA Folding and Catalysis Mediated by Iron (II). *PLoS One*, **7**, e38024.

93. Okafor, C.D., Bowman, J.C., Hud, N.V., Glass, J.B. and Williams, L.D. (2018), *Prebiotic Chemistry and Chemical Evolution of Nucleic Acids*, pp. 227-243.

94. Bray, M.S., Lenz, T.K., Haynes, J.W., Bowman, J.C., Petrov, A.S., Reddi, A.R., Hud, N.V., Williams, L.D. and Glass, J.B. (2018) Multiple Prebiotic Metals Mediate Translation. *Proc Natl Acad Sci USA*, **115**, 12164-12169.

95. Okafor, C.D., Lanier, K.A., Petrov, A.S., Athavale, S.S., Bowman, J.C., Hud, N.V. and Williams, L.D. (2017) Iron Mediates Catalysis of Nucleic Acid Processing Enzymes: Support for Fe(II) as a Cofactor before the Great Oxidation Event. *Nucleic Acids Res*, **45**, 3634-3642.

96. Dimroth, K., Jaenicke, L. and Heinzel, D. (1950) Die Spaltung Der Pentose-Nucleinsäure Der Hefe Mit Bleihydroxyd. *Justus Liebigs Ann Chem*, **566**, 206-210.

97. Lindahl, T., Adams, A. and Fresco, J.R. (1966) Renaturation of Transfer Ribonucleic Acids through Site Binding of Magnesium. *Proc Natl Acad Sci USA*, **55**, 941-948.

98. Guth-Metzler, R., Bray, M.S., Frenkel-Pinter, M., Suttapitugsakul, S., Montllor-Albalate, C., Bowman, J.C., Wu, R., Reddi, A.R., Okafor, C.D. and Glass, J.B. (2020) Cutting in-Line with Iron: Ribosomal Function and Non-Oxidative RNA Cleavage. *Nucleic Acids Res*, **48**, 8663-8674.

99. Bernier, C.R., Petrov, A.S., Kovacs, N.A., Penev, P.I. and Williams, L.D. (2018) Translation: The Universal Structural Core of Life. *Mol Biol Evol*, **35**, 2065-2076.

100. Melnikov, S., Ben-Shem, A., Garreau de Loubresse, N., Jenner, L., Yusupova, G. and Yusupov, M. (2012) One Core, Two Shells: Bacterial and Eukaryotic Ribosomes. *Nat Struct Mol Biol*, **19**, 560-567.

101. Woese, C.R. (2001) Translation: In Retrospect and Prospect. *RNA*, **7**, 1055-1067.

102. Noller, H.F., Kop, J., Wheaton, V., Brosius, J., Gutell, R.R., Kopylov, A.M., Dohme, F., Herr, W., Stahl, D.A. and Gupta, R. (1981) Secondary Structure Model for 23S Ribosomal RNA. *Nucleic Acids Res*, **9**, 6167-6189.

103. Bokov, K. and Steinberg, S.V. (2009) A Hierarchical Model for Evolution of 23S Ribosomal RNA. *Nature*, **457**, 977-980.

104. Kovacs, N.A., Petrov, A.S., Lanier, K.A. and Williams, L.D. (2017) Frozen in Time: The History of Proteins. *Mol Biol Evol*, **34**, 1252-1260.

105. Agmon, I., Bashan, A. and Yonath, A. (2006) On Ribosome Conservation and Evolution. *Isr J Ecol Evol*, **52**, 359-374.

106. Klein, D.J., Moore, P.B. and Steitz, T.A. (2004) The Contribution of Metal Ions to the Structural Stability of the Large Ribosomal Subunit. *RNA*, **10**, 1366-1379.

107. Anbar, A.D. (2008) Elements and Evolution. *Science*, **322**, 1481-1483.

108. Hsiao, C. and Williams, L.D. (2009) A Recurrent Magnesium-Binding Motif Provides a Framework for the Ribosomal Peptidyl Transferase Center. *Nucleic Acids Res*, **37**, 3134-3142.

109. Lin, S.Y., Wang, Y.C. and Hsiao, C. (2019) Prebiotic Iron Originates the Peptidyl Transfer Origin. *Mol Biol Evol*, **36**, 999-1007.

110. Schuwirth, B.S., Borovinskaya, M.A., Hau, C.W., Zhang, W., Vila-Sanjurjo, A., Holton, J.M. and Cate, J.H.D. (2005) Structures of the Bacterial Ribosome at 3.5 Å Resolution. *Science*, **310**, 827-834.

111. Selmer, M., Dunham, C.M., Murphy, F.V., Weixlbaumer, A., Petry, S., Kelley, A.C., Weir, J.R. and Ramakrishnan, V. (2006) Structure of the 70S Ribosome Complexed with mRNA and tRNA. *Science*, **313**, 1935-1942.

112. Demeshkina, N., Jenner, L., Westhof, E., Yusupov, M. and Yusupova, G. (2012) A New Understanding of the Decoding Principle on the Ribosome. *Nature*, **484**, 256-259.

113. Petrov, A.S., Bernier, C.R., Hsiao, C., Okafor, C.D., Tannenbaum, E., Stern, J., Gaucher, E., Schneider, D., Hud, N.V., Harvey, S.C. and Williams, L.D. (2012) RNA-Magnesium-Protein Interactions in Large Ribosomal Subunit. *J Phys Chem B*, **116**, 8113-8120.

114. Soukup, G.A. and Breaker, R.R. (1999) Relationship between Internucleotide Linkage Geometry and the Stability of RNA. *RNA*, **5**, 1308-1325.

115. Winkler, W.C., Nahvi, A., Roth, A., Collins, J.A. and Breaker, R.R. (2004) Control of Gene Expression by a Natural Metabolite-Responsive Ribozyme. *Nature*, **428**, 281.

116. Dorner, S. and Barta, A. (1999) Probing Ribosome Structure by Europium-Induced RNA Cleavage. *Biol Chem*, **380**, 243-251.

117. Winter, D., Polacek, N., Halama, I., Streicher, B. and Barta, A. (1997) Lead-Catalysed Specific Cleavage of Ribosomal RNAs. *Nucleic Acids Res*, **25**, 1817-1824.

118. Pyle, A.M. (2002) Metal Ions in the Structure and Function of RNA. *J Biol Inorg Chem*, **7**, 679-690.

119. Pan, T. and Uhlenbeck, O.C. (1992) In Vitro Selection of RNAs That Undergo Autolytic Cleavage with Lead (2+). *Biochemistry*, **31**, 3887-3895.

120. Winterbourn, C.C. (1995) Toxicity of Iron and Hydrogen Peroxide: The Fenton Reaction. *Toxicol Lett*, **82**, 969-974.

121. Fischbacher, A., von Sonntag, C. and Schmidt, T.C. (2017) Hydroxyl Radical Yields in the Fenton Process under Various pH, Ligand Concentrations and Hydrogen Peroxide/Fe(II) Ratios. *Chemosphere*, **182**, 738-744.

122. Dixon, W.J., Hayes, J.J., Levin, J.R., Weidner, M.F., Dombroski, B.A. and Tullius, T.D. (1991) Hydroxyl Radical Footprinting. *Methods Enzymol*, **208**, 380-413.

123. Tullius, T.D. (1996) In Suslick, K. (ed.), *Comprehensive Supramolecular Chemistry*. Elsevier, Tarrytown, NY, Vol. 5, pp. 317-343.

124. Celander, D.W. and Cech, T.R. (1991) Visualizing the Higher Order Folding of a Catalytic RNA Molecule. *Science*, **251**, 401-407.

125. Li, Z., Wu, J. and Deleo, C.J. (2006) RNA Damage and Surveillance under Oxidative Stress. *IUBMB Life*, **58**, 581-588.

126. Shcherbik, N. and Pestov, D.G. (2019) The Impact of Oxidative Stress on Ribosomes: From Injury to Regulation. *Cells*, **8**, 1379.

127. Li, Y. and Breaker, R.R. (1999) Kinetics of RNA Degradation by Specific Base Catalysis of Transesterification Involving the 2'-Hydroxyl Group. *J Am Chem Soc*, **121**, 5364-5372.

128. Kuusela, S. and Lönnberg, H. (1993) Metal Ions That Promote the Hydrolysis of Nucleoside Phosphoesters Do Not Enhance Intramolecular Phosphate Migration. *J Phys Org*, **6**, 347-356.

129. Hsiao, C., Lenz, T.K., Peters, J.K., Fang, P.-Y., Schneider, D.M., Anderson, E.J., Preeprem, T., Bowman, J.C., O'Neill, E.B. and Lie, L. (2013) Molecular Paleontology: A Biochemical Model of the Ancestral Ribosome. *Nucleic Acids Res*, **41**, 3373-3385.

130. Riemer, J., Hoepken, H.H., Czerwinska, H., Robinson, S.R. and Dringen, R. (2004) Colorimetric Ferrozine-Based Assay for the Quantitation of Iron in Cultured Cells. *Anal Biochem*, **331**, 370-375.

131. Maguire, B.A., Wondrack, L.M., Contillo, L.G. and Xu, Z. (2008) A Novel Chromatography System to Isolate Active Ribosomes from Pathogenic Bacteria. *RNA*, **14**, 188-195.

132. Shimizu, Y., Inoue, A., Tomari, Y., Suzuki, T., Yokogawa, T., Nishikawa, K. and Ueda, T. (2001) Cell-Free Translation Reconstituted with Purified Components. *Nature Biotechnol*, **19**, 751-755.

133. Rappsilber, J., Mann, M. and Ishihama, Y. (2007) Protocol for Micro-Purification, Enrichment, Pre-Fractionation and Storage of Peptides for Proteomics Using StageTips. *Nat Protoc*, **2**, 1896-1906.

134. Cox, J. and Mann, M. (2008) MaxQuant Enables High Peptide Identification Rates, Individualized P.P.B.-Range Mass Accuracies and Proteome-Wide Protein Quantification. *Nat Biotechnol*, **26**, 1367-1372.

135. Cox, J., Neuhauser, N., Michalski, A., Scheltema, R.A., Olsen, J.V. and Mann, M. (2011) Andromeda: A Peptide Search Engine Integrated into the MaxQuant Environment. *J Proteome Res*, **10**, 1794-1805.

136. Kurylo, C.M., Alexander, N., Dass, R.A., Parks, M.M., Altman, R.A., Vincent, C.T., Mason, C.E. and Blanchard, S.C. (2016) Genome Sequence and Analysis of *Escherichia coli* MRE600, a Colicinogenic, Nonmotile Strain That Lacks RNase I and the Type I Methyltransferase, EcoKI. *Genome Biol Evol*, **8**, 742-752.

137. Tyanova, S., Temu, T., Sinitcyn, P., Carlson, A., Hein, M.Y., Geiger, T., Mann, M. and Cox, J. (2016) The Perseus Computational Platform for Comprehensive Analysis of (Prote)Omics Data. *Nat Methods*, **13**, 731-740.

138. Tullius, T.D., Dombroski, B.A., Churchill, M.E. and Kam, L. (1987) Hydroxyl Radical Footprinting: A High-Resolution Method for Mapping Protein-DNA Contacts. *Methods Enzymol*, **155**, 537-558.

139. Handing, K.B., Niedzialkowska, E., Shabalin, I.G., Kuhn, M.L., Zheng, H. and Minor, W. (2018) Characterizing Metal-Binding Sites in Proteins with X-ray Crystallography. *Nat Protoc*, **13**, 1062.

140. Rivera, M.C., Maguire, B. and Lake, J.A. (2015) Isolation of Ribosomes and Polysomes. *Cold Spring Harb Protoc*, **2015**, pdb.prot081331.

141. Kuusela, S., Azhayev, A., Guzaev, A. and Lönnberg, H. (1995) The Effect of the 3′-Terminal Monophosphate Group on the Metal-Ion-Promoted Hydrolysis of the Phosphodiester Bonds of Short Oligonucleotides. *J Chem Soc Perk Trans 2*, 1197-1202.

142. Kuusela, S. and Lönnberg, H. (1996) Zn^{2+}-Promoted Hydrolysis of 3′,5′-Dinucleoside Monophosphates and Polyribonucleotides. The Effect of Nearest Neighbours on the Cleavage of Phosphodiester Bonds. *Nucleosides Nucleotides Nucl Acids*, **15**, 1669-1678.

143. Kuusela, S. and Lönnberg, H. (1994) Metal-Ion-Promoted Hydrolysis of Polyuridylic Acid. *J Chem Soc Perk Trans 2*, 2301-2306.

144. Ikenaga, H. and Inoue, Y. (1974) Metal (II) Ion Catalyzed Transphosphorylation of Four Homodinucleotides and Five Pairs of Dinucleotide Sequence Isomers. *Biochemistry*, **13**, 577-582.

145. Breslow, R. and Huang, D.-L. (1991) Effects of Metal Ions, Including Mg^{2+} and Lanthanides, on the Cleavage of Ribonucleotides and RNA Model Compounds. *Proc Natl Acad Sci USA*, **88**, 4080-4083.

146. Honda, K., Smith, M.A., Zhu, X., Baus, D., Merrick, W.C., Tartakoff, A.M., Hattier, T., Harris, P.L., Siedlak, S.L., Fujioka, H., Liu, Q., Moreira, P.I., Miller, F.P., Nunomura, A., Shimohama, S. and Perry, G. (2005) Ribosomal RNA in

Alzheimer Disease Is Oxidized by Bound Redox-Active Iron. *J Biol Chem*, **280**, 20978-20986.

147. Zinskie, J.A., Ghosh, A., Trainor, B.M., Shedlovskiy, D., Pestov, D.G. and Shcherbik, N. (2018) Iron-Dependent Cleavage of Ribosomal RNA During Oxidative Stress in the Yeast *Saccharomyces cerevisiae*. *J Biol Chem*, **293**, 14237-14248.

148. Moon, W.J. and Liu, J. (2020) Replacing Mg^{2+} by Fe^{2+} for RNA-Cleaving DNAzymes. *ChemBioChem*, **21**, 401-407.

149. Guth-Metzler, R., Mohamed, A.M., Cowan, E.T., Henning, A., Ito, C., Frenkel-Pinter, M., Wartell, R.M., Glass, J.B. and Williams, L.D. (2023) Goldilocks and RNA: Where Mg^{2+} Concentration Is Just Right. *Nucleic Acids Res*, gkad124.

150. Runnels, C.M., Lanier, K.A., Williams, J.K., Bowman, J.C., Petrov, A.S., Hud, N.V. and Williams, L.D. (2018) Folding, Assembly, and Persistence: The Essential Nature and Origins of Biopolymers. *J Mol Evol*, **86**, 598-610.

151. Lindahl, T. (1993) Instability and Decay of the Primary Structure of DNA. *Nature*, **362**, 709-715.

152. Peller, L. (1976) On the Free-Energy Changes in the Synthesis and Degradation of Nucleic Acids. *Biochemistry*, **15**, 141-146.

153. Martin, R.B. (1998) Free Energies and Equilibria of Peptide Bond Hydrolysis and Formation. *Biopolymers: Original Research on Biomolecules*, **45**, 351-353.

154. Leloir, L.F., Cardini, C.E. and Cabib, E. (1960) Utilization of Free Energy for the Biosynthesis of Saccharides.

155. Lindahl, T. (1967) Irreversible Heat Inactivation of Transfer Ribonucleic Acids. *J Biol Chem*, **242**, 1970-1973.

156. Li, Y. and Breaker, R.R. (1999) Kinetics of RNA Degradation by Specific Base Catalysis of Transesterification Involving the 2'-Hydroxyl Group. *J Am Chem Soc*, **121**, 5364-5372.

157. Ciesiołka, J., Michałowski, D., Wrzesinski, J., Krajewski, J. and Krzyżosiak, W.J. (1998) Patterns of Cleavages Induced by Lead Ions in Defined RNA Secondary Structure Motifs. *Journal of Molecular Biology*, **275**, 211-220.

158. Lindell, M., Bränvall, M., Wagner, E.G.H. and Kirsebom, L.A. (2005) Lead(II) Cleavage Analysis of RNase P RNA in Vivo. *RNA*, **11**, 1348-1354.

159. Regulski, E.E. and Breaker, R.R. (2008) In Wilusz, J. (ed.), *Post-Transcriptional Gene Regulation*. Humana Press, Totowa, NJ, pp. 53-67.

160. Behlen, L.S., Sampson, J.R., DiRenzo, A.B. and Uhlenbeck, O.C. (1990) Lead-Catalyzed Cleavage of Yeast-tRNA^{Phe} Mutants. *Biochemistry*, **29**, 2515-2523.

161. DeRose, V.J. and Yglesias, M.V. (2021), *Reference Module in Chemistry, Molecular Sciences and Chemical Engineering*. Elsevier.

162. Wadley, L.M., Keating, K.S., Duarte, C.M. and Pyle, A.M. (2007) Evaluating and Learning from RNA Pseudotorsional Space: Quantitative Validation of a Reduced Representation for RNA Structure. *Journal of molecular biology*, **372**, 942-957.

163. Barciszewska, M.Z., Perrigue, P.M. and Barciszewski, J. (2016) tRNA – the Golden Standard in Molecular Biology. *Molecular BioSystems*, **12**, 12-17.

164. Kim, S.H., Suddath, F.L., Quigley, G.J., McPherson, A., Sussman, J.L., Wang, A.H., Seeman, N.C. and Rich, A. (1974) Three-Dimensional Tertiary Structure of Yeast Phenylalanine Transfer RNA. *Science*, **185**, 435-440.

165. Cate, J.H., Hanna, R.L. and Doudna, J.A. (1997) A Magnesium Ion Core at the Heart of a Ribozyme Domain. *Nature structural biology*, **4**, 553-558.

166. Silverman, S.K., Deras, M.L., Woodson, S.A., Scaringe, S.A. and Cech, T.R. (2000) Multiple Folding Pathways for the P4−P6 RNA Domain. *Biochemistry*, **39**, 12465-12475.

167. DeRose, V.J. (2007) Sensing Cellular Magnesium with RNA. *Nat Chem Biol*, **3**, 693-694.

168. Draper, D.E., Grilley, D. and Soto, A.M. (2005) Ions and RNA Folding. *Annual Review of Biophysics and Biomolecular Structure*, **34**, 221-243.

169. Corbett, J.F. (1972) Pseudo First-Order Kinetics. *J Chem Educ*, **49**, 663.

170. El Seoud, O.A., Baader, W.J. and Bastos, E.L. (2016) Practical Chemical Kinetics in Solution. *Encyclopedia of Physical Organic Chemistry*, 1-68.

171. Wayment-Steele, H.K., Kim, D.S., Choe, C.A., Nicol, J.J., Wellington-Oguri, R., Watkins, A.M., Sperberg, R.A.P., Huang, P.-S., Participants, E. and Das, R. (2020). Cold Spring Harbor Laboratory.

172. Rohatgi, R., Bartel, D.P. and Szostak, J.W. (1996) Nonenzymatic, Template-Directed Ligation of Oligoribonucleotides Is Highly Regioselective for the Formation of 3‘−5‘ Phosphodiester Bonds. *J Am Chem Soc*, **118**, 3340-3344.

173. Cole, P.E., Yang, S.K. and Crothers, D.M. (1972) Conformational Changes of Transfer Ribonucleic Acid. Equilibrium Phase Diagrams. *Biochemistry*, **11**, 4358-4368.

174. Sclavi, B., Sullivan, M., Chance, M.R., Brenowitz, M. and Woodson, S.A. (1998) RNA Folding at Millisecond Intervals by Synchrotron Hydroxyl Radical Footprinting. *Science*, **279**, 1940-1943.

175. Li, P.T.X., Collin, D., Smith, S.B., Bustamante, C. and Tinoco, I. (2006) Probing the Mechanical Folding Kinetics of TAR RNA by Hopping, Force-Jump, and Force-Ramp Methods. *Biophysical Journal*, **90**, 250-260.

176. Hodak, J.H., Fiore, J.L., Nesbitt, D.J., Downey, C.D. and Pardi, A. (2005) Docking Kinetics and Equilibrium of a GAAA Tetraloop-Receptor Motif Probed by Single-Molecule FRET. *Proc Natl Acad Sci USA*, **102**, 10505.

177. Zarrinkar, P.P., Wang, J. and Williamson, J.R. (1996) Slow Folding Kinetics of RNase P RNA. *RNA (New York, NY)*, **2**, 564-573.

178. Heilman-Miller, S.L., Pan, J., Thirumalai, D. and Woodson, S.A. (2001) Role of Counterion Condensation in Folding of the *Tetrahymena* Ribozyme II. *Journal of Molecular Biology*, **309**, 57-68.

179. Labuda, D. and Poerschke, D. (1982) Magnesium Ion Inner Sphere Complex in the Anticodon Loop of $tRNA^{Phe}$. *Biochemistry*, **21**, 49-53.

180. Bujalowski, W., Graeser, E., McLaughlin, L.W. and Porschke, D. (1986) Anticodon Loop of $tRNA^{Phe}$: Structure, Dynamics, and Magnesium Binding. *Biochemistry*, **25**, 6365-6371.

181. Pörschke, D. (1976) Thermodynamic and Kinetic Parameters of Ion Condensation to Polynucleotides: Outer Sphere Complex Formed by Mg++ Ions. *Biophysical Chemistry*, **4**, 383-394.

182. Cowan, J.A. (1991) Coordination Chemistry of Magnesium Ions and 5S rRNA (*Escherichia coli*): Binding Parameters, Ligand Symmetry, and Implications for Activity. *J Am Chem Soc*, **113**, 675-676.

183. Eigen, M. (1963) Fast Elementary Steps in Chemical Reaction Mechanisms. **6**, 97-116.

184. Hyeon, C. and Thirumalai, D. (2012) Chain Length Determines the Folding Rates of RNA. *Biophysical journal*, **102**, L11-L13.

185. Blum, A.D., Uhlenbeck, O.C. and Tinoco, I. (1972) Circular Dichroism Study of Nine Species of Transfer Ribonucleic Acid. *Biochemistry*, **11**, 3248-3256.

186. Serebrov, V., Clarke, R.J., Gross, H.J. and Kisselev, L. (2001) Mg^{2+}-Induced tRNA Folding. *Biochemistry*, **40**, 6688-6698.

187. Friedrich, K., Woolley, P. and SteinhÄUser, K.G. (1988) Electrostatic Potential of Macromolecules Measured by pK_a Shift of a Fluorophore. *European Journal of Biochemistry*, **173**, 233-239.

188. Thomas, J.C., Schurr, J.M., Reid, B.R., Ribeiro, N.S. and Hare, D. (1984) Effect of Magnesium(2+) on the Solution Conformation of Two Different Transfer Ribonucleic Acids. *Biochemistry*, **23**, 5414-5420.

189. Robison, B. and Zimmerman, T.P. (1971) A Conformational Study of Yeast Phenylalanine Transfer Ribonucleic Acid. *J Biol Chem*, **246**, 110-117.

190. Maglott, E.J., Deo, S.S., Przykorska, A. and Glick, G.D. (1998) Conformational Transitions of an Unmodified tRNA: Implications for RNA Folding. *Biochemistry*, **37**, 16349-16359.

191. Privalov, P.L. and Filimonov, V.V. (1978) Thermodynamic Analysis of Transfer RNA Unfolding. *Journal of Molecular Biology*, **122**, 447-464.

192. Shelton, V.M., Sosnick, T.R. and Pan, T. (1999) Applicability of Urea in the Thermodynamic Analysis of Secondary and Tertiary RNA Folding. *Biochemistry*, **38**, 16831-16839.

193. Olson, T., Fournier, M.J., Langley, K.H. and Ford, N.C. (1976) Detection of a Major Conformational Change in Transfer Ribonucleic Acid by Laser Light Scattering. *Journal of Molecular Biology*, **102**, 193-203.

194. Rhee, K.W., Potts, R.O., Wang, C.-C., Fournier, M.J. and Ford, N.C., Jr. (1981) Effects of Magnesium and Ionic Strength on the Diffusion and Charge Properties of Several Single tRNA Species. *Nucleic Acids Res*, **9**, 2411-2420.

195. Fritzinger, D.C. and Fournier, M.J. (1982) Chemical Modification Analysis of Ion-Dependent Changes in the Solution Structure of Yeast Phenylalanine tRNA. *Biochemistry*, **21**, 2118-2127.

196. Fang, X., Littrell, K., Yang, X.-j., Henderson, S.J., Siefert, S., Thiyagarajan, P., Pan, T. and Sosnick, T.R. (2000) Mg^{2+}-Dependent Compaction and Folding of Yeast-$tRNA^{Phe}$ and the Catalytic Domain of the *B. subtilis* RNase P RNA Determined by Small-Angle X-ray Scattering. *Biochemistry*, **39**, 11107-11113.

197. Silverman, S.K. and Cech, T.R. (1999) RNA Tertiary Folding Monitored by Fluorescence of Covalently Attached Pyrene. *Biochemistry*, **38**, 14224-14237.

198. Silverman, S.K. and Cech, T.R. (2001) An Early Transition State for Folding of the P4-P6 RNA Domain. *RNA*, **7**, 161-166.

199. Yamagami, R., Sieg, J.P., Assmann, S.M. and Bevilacqua, P.C. (2022) Genome-Wide Analysis of the in Vivo tRNA Structurome Reveals RNA Structural and Modification Dynamics under Heat Stress. *Proc Natl Acad Sci USA*, **119**, e2201237119.

200. Li, J., Xu, C., Shimada, N., Miyoshi, Y., Watanabe, K., Cong, W. and Ohtsuki, T. (2017) Detection of Small, Highly Structured RNAs Using Molecular Beacons. *Analytical Methods*, **9**, 2971-2976.

201. Leipply, D. and Draper, D.E. (2010) Dependence of RNA Tertiary Structural Stability on Mg^{2+} Concentration: Interpretation of the Hill Equation and Coefficient. *Biochemistry*, **49**, 1843-1853.

202. Brion, P. and Westhof, E. (1997) Hierarchy and Dynamics of RNA Folding. *Annual review of biophysics and biomolecular structure*, **26**, 113-137.

203. Shcherbakova, I. and Brenowitz, M. (2005) Perturbation of the Hierarchical Folding of a Large RNA by the Destabilization of Its Scaffold's Tertiary Structure. *Journal of Molecular Biology*, **354**, 483-496.

204. Bisaria, N., Greenfeld, M., Limouse, C., Pavlichin, D.S., Mabuchi, H. and Herschlag, D. (2016) Kinetic and Thermodynamic Framework for P4-P6 RNA Reveals Tertiary Motif Modularity and Modulation of the Folding Preferred Pathway. *Proc Natl Acad Sci USA*, **113**, E4956-E4965.

205. Radzicka, A. and Wolfenden, R. (1996) Rates of Uncatalyzed Peptide Bond Hydrolysis in Neutral Solution and the Transition State Affinities of Proteases. *J Am Chem Soc*, **118**, 6105-6109.

206. Eisenberg, D., Kauzmann, W. and Kauzmann, W. (2005) *The Structure and Properties of Water*. Oxford University Press on Demand.

207. Okorokov, L.A., Lichko, L.P. and Kulaev, I.S. (1980) Vacuoles: Main Compartments of Potassium, Magnesium, and Phosphate Ions in *Saccharomyces carlsbergenis* Cells. *J Bacteriol*, **144**, 661-665.

208. Beeler, T., Bruce, K. and Dunn, T. (1997) Regulation of Cellular Mg^{2+} by *Saccharomyces cerevisiae*. *Biochim Biophys Acta*, **1323**, 310-318.

209. Daher, M., Widom, J.R., Tay, W. and Walter, N.G. (2018) Soft Interactions with Model Crowders and Non-Canonical Interactions with Cellular Proteins Stabilize RNA Folding. *Journal of Molecular Biology*, **430**, 509-523.

210. Leamy, K.A., Assmann, S.M., Mathews, D.H. and Bevilacqua, P.C. (2016) Bridging the Gap between in Vitro and in Vivo RNA Folding. *Quarterly reviews of biophysics*, **49**, e10-e10.

211. Hambraeus, G., von Wachenfeldt, C. and Hederstedt, L. (2003) Genome-Wide Survey of mRNA Half-Lives in *Bacillus subtilis* Identifies Extremely Stable Mrnas. *Mol Genet Genomics*, **269**, 706-714.

212. Rabani, M., Raychowdhury, R., Jovanovic, M., Rooney, M., Stumpo, Deborah J., Pauli, A., Hacohen, N., Schier, Alexander F., Blackshear, Perry J., Friedman, N., Amit, I. and Regev, A. (2014) High-Resolution Sequencing and Modeling Identifies Distinct Dynamic RNA Regulatory Strategies. *Cell*, **159**, 1698-1710.

213. Geisberg, J.V., Moqtaderi, Z., Fan, X., Ozsolak, F. and Struhl, K. (2014) Global Analysis of mRNA Isoform Half-Lives Reveals Stabilizing and Destabilizing Elements in Yeast. *Cell*, **156**, 812-824.

214. Chen, H., Shiroguchi, K., Ge, H. and Xie, X.S. (2015) Genome-Wide Study of mRNA Degradation and Transcript Elongation in *Escherichia coli*. *Mol Syst Biol*, **11**, 781.

215. Chan, L.Y., Mugler, C.F., Heinrich, S., Vallotton, P. and Weis, K. (2018) Non-Invasive Measurement of mRNA Decay Reveals Translation Initiation as the Major Determinant of mRNA Stability. *eLife*, **7**, e32536.

216. Choe, B.K. and Taylor, M.W. (1972) Kinetics of Synthesis and Characterization of Transfer RNA Precursors in Mammalian Cells. *Biochimica et Biophysica Acta (BBA) - Nucleic Acids and Protein Synthesis*, **272**, 275-287.

217. Abelson, H.T., Johnson, L.F., Penman, S. and Green, H. (1974) Changes in RNA in Relation to Growth of the Fibroblast: II. The Lifetime of mRNA, rRNA, and tRNA in Resting and Growing Cells. *Cell*, **1**, 161-165.

218. Karnahl, U. and Wasternack, C. (1992) Half-Life of Cytoplasmic rRNA and tRNA, of Plastid rRNA and of Uridine Nucleotides in Heterotrophically and Photoorganotrophically Grown Cells of *Euglena gracilis* and Its Apoplastic Mutant W3BUL. *The International journal of biochemistry*, **24**, 493-497.

219. Gudipati, Rajani K., Xu, Z., Lebreton, A., Séraphin, B., Steinmetz, Lars M., Jacquier, A. and Libri, D. (2012) Extensive Degradation of RNA Precursors by the Exosome in Wild-Type Cells. *Mol Cell*, **48**, 409-421.

220. Hirsch, C.A. and Hiatt, H.H. (1966) Turnover of Liver Ribosomes in Fed and in Fasted Rats. *J Biol Chem*, **241**, 5936-5940.

221. Gillery, P., Georges, N., Wegrowski, J., Randoux, A. and Borel, J.-P. (1995) Protein Synthesis in Collagen Lattice-Cultured Fibroblasts Is Controlled at the Ribosomal Level. *FEBS Letters*, **357**, 287-289.

222. Halle, J.P., Müller, S., Simm, A. and Adam, G. (1997) Copy Number, Epigenetic State and Expression of the rRNA Genes in Young and Senescent Rat Embryo Fibroblasts. *Eur J Cell Biol*, **74**, 281-288.

223. Yi, X., Tesmer, V.M., Savre-Train, I., Shay, J.W. and Wright, W.E. (1999) Both Transcriptional and Posttranscriptional Mechanisms Regulate Human Telomerase Template RNA Levels. *Mol Cell Biol*, **19**, 3989-3997.

224. Nercessian, D. and Conde, R.D. (2006) Control of Ribosome Turnover During Growth of the Haloalkaliphilic Archaeon *Natronococcus occultus*. *Res Microbiol*, **157**, 625-628.

225. Romani, A.M. (2011) Cellular Magnesium Homeostasis. *Archives of biochemistry and biophysics*, **512**, 1-23.

226. Frenkel-Pinter, M., Haynes, J.W., Mohyeldin, A.M., C, M., Sargon, A.B., Petrov, A.S., Krishnamurthy, R., Hud, N.V., Williams, L.D. and Leman, L.J. (2020) Mutually Stabilizing Interactions between Proto-Peptides and RNA. *Nature Communications*, **11**, 3137.

227. Arnold, J.J., Ghosh, S.K.B. and Cameron, C.E. (1999) Poliovirus RNA-Dependent RNA Polymerase (3dpol): Divalent Cation Modulation of Primer, Template, and Nucleotide Selection. *J Biol Chem*, **274**, 37060-37069.

228. Toriyama, S. (1987) Ribonucleic Acid Polymerase Activity in Filamentous Nucleoproteins of Rice Grassy Stunt Virus. *J Gen Virol*, **68**, 925-929.

229. Kim, Y., Dumett Torres, D. and Jain, P.K. (2016) Activation Energies of Plasmonic Catalysts. *Nano Lett*, **16**, 3399-3407.

230. Roth, A.S.G., Bourdon, B., Mojzsis, S.J., Touboul, M., Sprung, P., Guitreau, M. and Blichert-Toft, J. (2013) Inherited 142Nd Anomalies in Eoarchean Protoliths. *Earth Planet Sci Lett*, **361**, 50-57.

231. Kamber Balz, S., Moorbath, S. and Whitehouse Martin, J. (2001) The Oldest Rocks on Earth: Time Constraints and Geological Controversies. *Geological Society, London, Special Publications*, **190**, 177-203.

232. Reimink, J.R., Chacko, T., Stern, R.A. and Heaman, L.M. (2016) The Birth of a Cratonic Nucleus: Lithogeochemical Evolution of the 4.02–2.94ga Acasta Gneiss Complex. *Precambrian Res*, **281**, 453-472.

233. Mojzsis, S.J., Harrison, T.M. and Pidgeon, R.T. (2001) Oxygen-Isotope Evidence from Ancient Zircons for Liquid Water at the Earth's Surface 4,300 Myr Ago. *Nature*, **409**, 178-181.

234. Wilde, S.A., Valley, J.W., Peck, W.H. and Graham, C.M. (2001) Evidence from Detrital Zircons for the Existence of Continental Crust and Oceans on the Earth 4.4 Gyr Ago. *Nature*, **409**, 175-178.

235. Allwood, A.C., Rosing, M.T., Flannery, D.T., Hurowitz, J.A. and Heirwegh, C.M. (2018) Reassessing Evidence of Life in 3,700-Million-Year-Old Rocks of Greenland. *Nature*, **563**, 241-244.

236. Briggs, D.E.G. and Summons, R.E. (2014) Ancient Biomolecules: Their Origins, Fossilization, and Role in Revealing the History of Life. *Bioessays*, **36**, 482-490.

237. Hampel, K.J. and Burke, J.M. (2001) Time-Resolved Hydroxyl-Radical Footprinting of RNA Using Fe(II)-EDTA. *Methods*, **23**, 233-239.

238. Glass, J.B., Kretz, C.B., Ganesh, S., Ranjan, P., Seston, S.L., Buck, K.N., Landing, W.M., Morton, P.L., Moffett, J.W., Giovannoni, S.J., Vergin, K.L. and Stewart, F.J. (2015) Meta-Omic Signatures of Microbial Metal and Nitrogen Cycling in Marine Oxygen Minimum Zones. *Frontiers in microbiology*, **6**.

239. Shin, W., Wu, A., Massidda, M.W., Foster, C., Thomas, N., Lee, D.-W., Koh, H., Ju, Y., Kim, J. and Kim, H.J. (2019) A Robust Longitudinal Co-Culture of Obligate Anaerobic Gut Microbiome with Human Intestinal Epithelium in an Anoxic-Oxic Interface-on-a-Chip. *Frontiers in Bioengineering and Biotechnology*, **7**.

240. Anderson, G.J. (2007) Mechanisms of Iron Loading and Toxicity. *American Journal of Hematology*, **82**, 1128-1131.

241. Eaton, J.W. and Qian, M. (2002) Molecular Bases of Cellular Iron Toxicity. *Free Radical Biol Med*, **32**, 833-840.

242. Jin, L., Engelhart, A.E., Zhang, W., Adamala, K. and Szostak, J.W. (2018) Catalysis of Template-Directed Nonenzymatic RNA Copying by Iron(II). *J Am Chem Soc*, **140**, 15016-15021.

243. Higgs, P.G. (2016) The Effect of Limited Diffusion and Wet–Dry Cycling on Reversible Polymerization Reactions: Implications for Prebiotic Synthesis of Nucleic Acids. *Life*, 10.3390/life6020024.

244. Wieczorek, R., Dörr, M., Chotera, A., Luisi, P.L. and Monnard, P.A. (2013) Formation of RNA Phosphodiester Bond by Histidine-Containing Dipeptides. *ChemBioChem*, **14**, 217-223.

245. Namani, T., Snyder, S., Eagan, J.M., Bevilacqua, P.C., Wesdemiotis, C. and Sahai, N. (2021) Amino Acid Specific Nonenzymatic Montmorillonite-Promoted RNA Polymerization. *ChemSystemsChem*, **3**, e2000060.

246. Won, J.-I., Shin, J., Park, S.Y., Yoon, J. and Jeong, D.-H. (2020) Global Analysis of the Human RNA Degradome Reveals Widespread Decapped and Endonucleolytic Cleaved Transcripts. *Int J Mol Sci*, 10.3390/ijms21186452.

247. Blumberg, A., Zhao, Y., Huang, Y.-F., Dukler, N., Rice, E.J., Chivu, A.G., Krumholz, K., Danko, C.G. and Siepel, A. (2021) Characterizing RNA Stability Genome-Wide through Combined Analysis of PRO-seq and RNA-Seq Data. *BMC Biol*, **19**, 1-17.

248. Abdul-Rahman, F. and Gresham, D. (2018) In Lamandé, S. R. (ed.), *mRNA Decay: Methods and Protocols*. Springer New York, New York, NY, pp. 15-24.

249. Lu, W., Zhou, Q. and Chen, Y. (2022) Impact of RNA Degradation on Next-Generation Sequencing Transcriptome Data. *Genomics*, **114**, 110429.

250. Tani, H., Mizutani, R., Salam, K.A., Tano, K., Ijiri, K., Wakamatsu, A., Isogai, T., Suzuki, Y. and Akimitsu, N. (2012) Genome-Wide Determination of RNA Stability Reveals Hundreds of Short-Lived Noncoding Transcripts in Mammals. *Genome Res*, **22**, 947-956.

251. Grubbs, R.D. (2002) Intracellular Magnesium and Magnesium Buffering. *BioMetals*, **15**, 251-259.

252. Murphy, E., Freudenrich, C.C. and Lieberman, M. (1991) Cellular Magnesium and Na/Mg Exchange in Heart Cells. *Annu Rev Physiol*, **53**, 273-287.

253. Tyrrell, J., McGinnis, J.L., Weeks, K.M. and Pielak, G.J. (2013) The Cellular Environment Stabilizes Adenine Riboswitch RNA Structure. *Biochemistry*, **52**, 8777-8785.

254. Froschauer, E.M., Kolisek, M., Dieterich, F., Schweigel, M. and Schweyen, R.J. (2004) Fluorescence Measurements of Free [Mg^{2+}] by Use of Mag-Fura 2 in *Salmonella enterica*. *FEMS Microbiol Lett*, **237**, 49-55.

255. Okorokov, L., Lichko, L., Kholodenko, V., Kadomtseva, V., Petrikevich, S., Zaichkin, E. and Karimova, A. (1975) Free and Bound Magnesium in Fungi and Yeasts. *Folia Microbiol*, **20**, 460-466.

256. Horowitz, S.B. and Tluczek, L. (1989) Gonadotropin Stimulates Oocyte Translation by Increasing Magnesium Activity through Intracellular Potassium-Magnesium Exchange. *Proc Natl Acad Sci USA*, **86**, 9652-9656.

257. Ryschon, T.W., Rosenstein, D.L., Rubinow, D.R., Niemela, J.E., Elin, R.J. and Balaban, R.S. (1996) Relationship between Skeletal Muscle Intracellular Ionized Magnesium and Measurements of Blood Magnesium. *Journal of Laboratory and Clinical Medicine*, **127**, 207-213.

258. Shindo, Y., Yamanaka, R., Suzuki, K., Hotta, K. and Oka, K. (2015) Intracellular Magnesium Level Determines Cell Viability in the MPP+ Model of Parkinson's Disease. *Biochim Biophys Acta*, **1853**, 3182-3191.